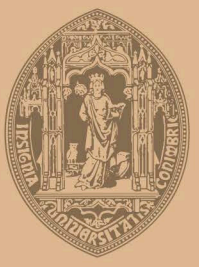

UNIVERSIDADE D
COIMBRA

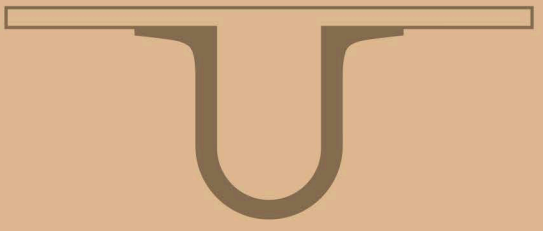

Rita Viegas Botelho Correia Rego

OPTIMIZATION STUDY OF THE PERFORMANCE OF A $LaBr_3$ MONOLITHIC SCINTILLATOR IN A COMPTON CAMERA SYSTEM

Thesis submitted to the Faculty of Sciences and Technology of the University of Coimbra
for the degree of Master in Biomedical Engineering,
supervised by Priv. Doz. Dr. Peter Thirolf and Prof. Dr. Paulo Crespo

September 2018

UNIVERSIDADE D COIMBRA
FACULDADE DE CIÊNCIAS E TECNOLOGIA

Rita Viegas Botelho Correia Rego

Optimization study of the performance of a $LaBr_3$ monolithic scintillator in a Compton camera system

Thesis submitted to the
University of Coimbra for the degree of
Master in Biomedical Engineering

Supervisors:
Priv. Doz. Dr. Peter Thirolf (LMU Munich)
Prof. Dr. Paulo Crespo (LIP and UC)

Coimbra, 2018

This work was developed in collaboration with:

Department of Physics, Faculty of Sciences and Technology, University of Coimbra

Chair of Experimental Physics, Medical Physics, Faculty for Physics of the Ludwig-Maximilians-Universität München

Para a minha mãe,
e para a nossa estrelinha

Acknowledgments

The conclusion of this thesis marks not only the ending of my 5 year journey in Biomedical Engineering but also the beginning of a new chapter in my life. I would like therefore to thank all the individuals that have supported and help me towards making this moment a reality. First and foremost my deep gratitude goes to Prof. Peter Thirolf for the opportunity of working in the Compton camera group and for all the guidance and continuous support in the months I spent at LMU Munich. Thank you for sharing your unwavering enthusiasm and love for physics, and for encouraging me to always be critical and aspire for more. My appreciation undoubtedly extends to Prof. Paulo Crespo for introducing me to medical imaging and for believing in me and finding me the opportunity to work at LMU Munich. I would also like to express my deepest appreciation to Prof. Katia Parodi for opening me the doors of the chair of Medical Physics and allowing me to work with her amazing group.

I would also like to thank the people who I have encounter during my stay in Munich and made this city my home for the last months, *how lucky am I to have something that makes saying goodbye so hard*. To Franz (and his bavarian mood), Carmen, Juliana, Maria, Giovanni and to everyone from the chair of Medical Physics of LMU for welcoming me with open arms in your family. Thank you to Tim for all the guidance, patience, support, moments of fun and for teaching me the Bavarian "ways". Grazie mille per tutto Silvia, for giving me a little bit of my Mediterranean home so far away, for all the support, for pink fridays, for not letting me fall into desperation mood (alone), for keeping me company in Garching at night (almost our second home now) and for helping me reach the light at the end of the tunnel. Without you this thesis would not be possible.

Em português, não posso deixar de agradecer à minha família por todo o apoio incondicional que me têm dado durante esta viagem. Um especial obrigada e um abraço de saudade à minha avó Liseta, que infelizmente já não está cá para presenciar o final desta etapa, que sempre me encorajou a seguir os meus sonhos e a encarar as

adversidades com um sorriso. Mas especialmente um obrigada à minha mãe, por me mostrar que não existem sonhos pequenos, que não existem objetivos inatingíveis e por continuar a lutar por um futuro melhor. As minhas conquistas também são tuas, e espero ter-te sempre a caminhar a meu lado.

Um obrigada especial às amizades que tenho construído e nutrido nos últimos anos. À Sofia por me ter acolhido na sua casa, por todo o carinho, por ser a minha "mãe alemã" e por ter partilhado o amor da Cookie comigo. Aos OV por tornarem estes últimos anos memoráveis e por terem partilhado comigo esta viagem académica. À Mariana e à Beatriz por toda a amizade e por me mostrarem que, na realidade, a distância não se mede em quilómetros.

E finalmente um obrigada ao João. Obrigada por estares sempre ao meu lado, por apoiares as minhas decisões e por me acompanhares nos meus sonhos. Pela tua infinita paciência e constante amor, *when I look at you I can feel it, I look at you and I am home.*

"Nothing in life is to be feared, it is only to be understood. Now is the time to understand more, so that we may fear less".

- Marie Curie

Resumo

A modalidade de terapia com hadrões, baseada em partículas aceleradas, é capaz de libertar dose com alta precisão a um volume de tumor específico sem comprometer, em princípio, o tecido saudável circundante. A principal vantagem desta modalidade terapêutica é o seu preciso alcance (pico de Bragg), no entanto incertezas na determinação deste alcance podem levar à possível irradiação de tecido saudável ou subdosagem do volume de tratamento do tumor durante a libertação do feixe. De forma a evitar os riscos associados com estas incertezas, margens de segurança necessitam de ser aplicadas durante o tratamento. Com o objetivo de diminuir estas margens, diferentes abordagens para verificação do feixe *in-vivo* têm sido propostas. Uma delas, a câmara de Compton, explora a cinemática de dispersão de Compton dos raios gama *prompt* incidentes através de interações nucleares entre o feixe de partículas incidente e o tecido orgânico.

A câmara de Compton da Ludwig-Maximilians-Universität Munich (LMU), sob estudo nesta tese, é composta por um detetor de dispersão (que consiste em seis camadas de detetores *double-sided silicon strip* (DSSSD)) e um detetor de absorção (um cristal monolítico de cintilação de $LaBr_3:Ce^{3+}$ acoplado a um tubo fotomultiplicador (PMT) multiânodo e sensível à posição). Devido ao design empilhado do detetor de dispersão, a câmara de Compton da LMU permite, não apenas localizar a energia do fotão incidente, mas também o eletrão de Compton disperso. A energia e posição de interação do fotão incidente permitem o cálculo do ângulo de dispersão de Compton, que representa a abertura do cone de Compton, cuja superfície indica a possível origem dos raios gama incidentes. Ao permitir a localização do eletrão, é possível melhorar a eficiência de reconstrução da câmara e reduzir a posição da fonte a um segmento de arco.

O principal objetivo desta tese foi otimizar a performance do detetor de absorção da câmara de Compton da LMU por redução do seu sistema de leitura de um PMT com 256 segmentos para um PMT com apenas 64 segmentos. Em particular, o detetor de absorção da câmara de Compton foi caracterizado, onde a sua resolução

energética, reconstrução da posição de interação dos fotões incidentes no cristal e a sua resolução espacial foram o principal foco deste trabalho.

A melhor resolução energética para o sistema sob estudo foi alcançada operando o detetor a voltagens entre -900 e -950 V, onde um valor de 4.3(1)% a 662 keV foi obtido.

A determinação da posição de interação dos fotões na superfície do cristal de cintilação $LaBr_3$:Ce^{3+} foi realizada usando o algoritmo *k-Nearest-Neighbor* (k-NN) e a sua versão melhorada o algoritmo *Categorical Average Patterns* (CAP), ambos desenvolvidos pela TU Delft para aplicações em PET. Estes algoritmos comparam a distribuição da amplitude de luz 2D do fotão disperso absorvido pelo cintilador com uma biblioteca de referência de distribuições de amplitude de luz 2D, adquirida irradiando perpendicularmente a superfície do cintilador com uma fonte de fotões colimada. As bibliotecas de referência necessárias foram geradas utilizando duas fontes colimadas, ^{137}Cs e ^{60}Co. Uma quantificação fidedigna da resolução espacial do detetor depende da qualidade da biblioteca de referência adquirida.

Uma resolução espacial ótima de 2.9(1) mm (FWHM) foi alcançada experimentalmente, utilizando o PMT com 64 segmentos, a 1.17 MeV e 1.33 MeV utilizando o algoritmo CAP. O valor obtido é comparável com o obtido previamente com um PMT com 256 segmentos, onde uma granularidade de 64 canais foi criada artificialmente por somatório através de Software [1, 2]. Para além disso, uma correlação entre a energia dos raios gama e a resolução espacial foi observada, de tal modo que quanto mais alta a energia dos raios gama incidentes melhor será a reconstrução da posição de interação. Esta tese de Mestrado provou que reduzindo experimentalmente a granularidade do PMT do detetor de absorção da LMU câmara de Compton, de 256 para 64, a performance do sistema é melhorada e a sua complexidade é reduzida. Pela primeira vez, o objetivo de design previsto de 3 mm para a resolução espacial do detetor de absorção da câmara de Compton da LMU foi ultrapassado experimentalmente para uma energia de 1.3 MeV. Devido à melhoria observada para a resolução espacial com o aumento da energia dos fotões, é esperado que a resolução espacial se mantenha dentro do valor desejado de 3 mm, ou até melhore, para energias de fotões superiores (4 - 6 MeV) relevantes em terapia de hadrões.

Palavras-chave: terapia com hadrões, imagem com *prompt*-gama, câmera de Compton, detetor de cintilação.

Abstract

The hadron therapy modality, based on accelerated particles, is capable of high-precision dose delivery to a specific tumour volume without, in principle, compromising the surrounding healthy tissue. The main advantage of this therapy modality is its well-defined range (Bragg peak), but uncertainties in the determination of this range can lead to possible irradiation of healthy tissue or under-dosing of the tumour treatment volume during the beam delivery. In order to avoid the risks associated with these uncertainties, safety margins need to be applied during treatment. With the goal of decreasing these margins, different approaches for in-vivo beam range verification have been proposed. One of these, the Compton camera, exploits the Compton scattering kinematics of the incident prompt gamma rays created through nuclear interactions between the incident beam particles and the organic tissue.

The Ludwig-Maximilians-Universität Munich Compton camera, under study in this thesis, is composed of a scatter detector (consisting of six layers of double-sided-silicon strip detectors (DSSSD)) and an absorber detector (a monolithic $LaBr_3$:Ce^{3+} scintillation crystal coupled to a multi-anode position-sensitive photomultiplier tube (PMT)). Due to the stacked design of the scatter detector, the Ludwig-Maximilians-Universität Munich (LMU) Compton camera allows not only for the tracking of the incident photon origin, but also of the Compton scattered electron. The energy and interaction position of the incident photon enables the calculation of the Compton scattering angle, which represents the opening angle of the so-called Compton cone, whose surface indicates the possible origin of the incident γ rays. By enabling the electron tracking, the camera's reconstruction efficiency is enhanced and the possible photon source position is reduced to an arc segment.

The main objective of this thesis was to optimize the performance of the LMU Compton camera absorber detector by reducing its readout system from a 256-fold segmented multi-anode position sensitive Photomultiplier Tube (PMT) to a 64-fold PMT granularity. In particular, the Compton camera absorber was characterized, where its energy resolution, the reconstruction of the interaction position of the

incident photons in the crystal, and the component's spatial resolution were the main focus of this work.

The best energy resolution for the system under study was achieved by operating the detector at bias voltages ranging from -900 to -950 V, where a value of 4.3(1)% at 662 keV was determined.

The determination of the photon interaction position on the $LaBr_3$:Ce^{3+} scintillator crystal's surface was performed using the k-Nearest-Neighbour (k-NN) algorithm and its improved version the Categorical Average Patterns (CAP) algorithm, both developed at TU Delft for PET applications. These algorithms compare the 2D light amplitude distribution of the scattered photon absorbed by the scintillator with a reference library of 2D light amplitude distributions, acquired by perpendicularly irradiating the scintillator's surface with a collimated photon source. The required reference libraries were generated using two different collimated sources, ^{137}Cs and ^{60}Co. A reliable quantification of the detector's spatial resolution depends on the quality of the acquired reference library.

An optimum spatial resolution of 2.9(1) mm (FWHM) was experimentally achieved, using a 64-fold segmented PMT, at 1.17 MeV and 1.33 MeV using the Categorical Average Patterns (CAP) algorithm. The obtained value is comparable to the one previously achieved with a 256-fold segmented PMT, where a PMT granularity of 64 channels was artificially created by software summation [1, 2]. Moreover, a correlation between the gamma ray energy and spatial resolution was observed, such that the higher the energy of the impinging γ ray the better the interaction position reconstruction will be. This Master thesis has therefore proven that by experimentally reducing the number of PMT readout channels of the LMU Compton camera absorber detector, from 256 to 64, the system's performance is improved and its complexity is reduced. For the first time, the envisaged design goal of 3 mm spatial resolution for the absorber detector of the LMU Compton camera was surpassed experimentally for a 1.3 MeV photon energy. Due to the observable improvement of the spatial resolution with the increase of the photon energy, it is expected that the spatial resolution will stay within the desired value of 3 mm, or even improve, for higher photon energies (4 - 6 MeV) relevant in hadron therapy.

Keywords: hadron therapy, prompt-gamma imaging, Compton camera, scintillation detector.

List of Acronyms

ASIC Application Specific Integrated Circuit.

CAP Categorical Average Patterns.
CGDR Categorical Gaussian Distributed Replacement.
CRT Coincidence Resolving Time.

DAQ Data Acquisition System.
DOI Depth-Of-Interaction.
DSSSD Double-Sided-Silicon Strip Detector.

FWHM Full Width at Half Maximum.

IVI Interaction Vertex Imaging.

k-NN k-Nearest-Neighbour.

LMU Ludwig-Maximilians-Universität Munich.
LOR Line-Of-Response.

MCFD Constant Fraction Discriminator module.
MQDC Charge-to-Digital Converter module.

PET Positron Emission Tomography.
PMT Photomultiplier Tube.
PTV Planning Treatment Volume.

RSP Relative Stopping Power.

S/B Signal-to-Background Ratio.
SOBP Spread Out Bragg Peak.

TOF Time-of-Flight.

UV Ultraviolet.

List of Figures

List of Tables

Contents

1

Introduction and Motivation

The purpose of this chapter is to provide an introduction and motivation for this thesis. The first part of this chapter gives a short introduction to hadron therapy and its advantages when compared to conventional photon-based radiotherapy, followed by the origin of ion beam range uncertainties associated with particle therapy. The second part of this chapter focuses on in-vivo range verification techniques being investigated for range monitoring during ion beam treatment. A brief introduction to these techniques will be given, starting with the most recent approach of ionoacoustic studies, followed by the use of charged secondary particles, positron-annihilation photon studies and finally studies using prompt γ-rays. In conclusion, this thesis' context, objectives and structural organization will be explained.

1.1 Hadron Therapy

According to the International Agency for Reasearch on Cancer in 2012, there were 14.1 million new cancer cases and 8.2 million cancer deaths, nearly 1 in 6 of all global deaths. Therefore there is an increased need of scientific and economic efforts in developing various cancer treatment modalities, mainly radiotherapy and chemotherapy. The Health Economics in Radiation Oncology project has shown that the need for radiotherapy in Europe is expected to increase by 16 % until 2025 [3].

The development of conventional radiotherapy started after the discovery of X-rays in 1895 by Wilhelm Conrad Röntgen [4]. This therapy is based on bremsstrahlung photons, which are generated with a linear accelerator [5]. In recent years an innovative cancer therapy has been developed, as an alternative to conventional radiotherapy (i.e. photon-based radiotherapy), known as hadron therapy, which is based on accelerated charged particles [6], that is capable of high-precision dose delivery. This treatment modality was first proposed by Robert R. Wilson in 1946 [7] and

in 1990 the first hospital-based proton therapy center was founded in Loma Linda, California [8]. Since 1954 about 150,000 patients have been treated with particle therapy worldwide, 86% of which have been treated with protons [9].

The increasing clinical interest in hadron therapy is a result of its characteristic interaction of charged particles in matter. As it can be seen in Fig. 1.1, while photon beams have a decreasing dose deposition with depth, the energy deposited at a certain penetration depth of charged particle beams (e.g. protons or carbon ions) is inversely proportional to the ion's energy, forming a high-dose region at the end of the particle range, known as the Bragg peak [10].

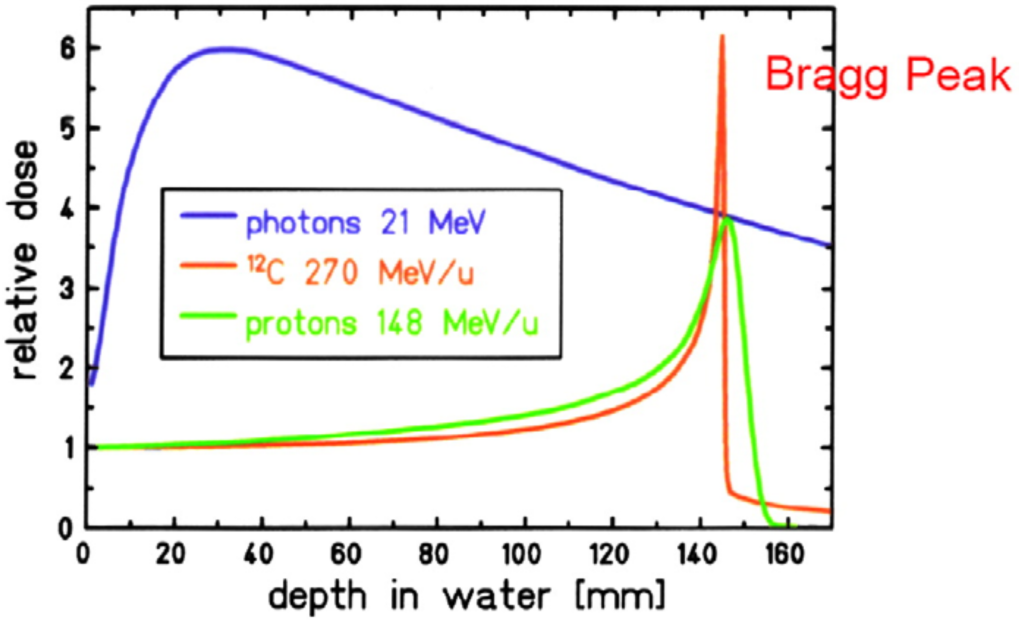

Figure 1.1: Depth-dose profiles of photons, protons, and carbon ions [10].

By delivering protons within a range of energies, the resulting Bragg peaks are combined forming the Spread Out Bragg Peak (SOBP) with a specific plateau width adjusted to the targeted tumour volume [10], creating a longitudinal conformality of the required dose [11]. In Fig. 1.2 is possible to see, represented by the black curves, the variation of the proton beam energy and the resulting SOBP, represented by the dashed blue curve [12]. Using particle beams instead of photon beams can increase the therapeutic ratio, defined as the ratio between tumour control and normal tissue complications [12]. This is possible due to the ability of a highly precise dose localization for tumour therapy with no dose in the normal tissue beyond the Bragg peak.

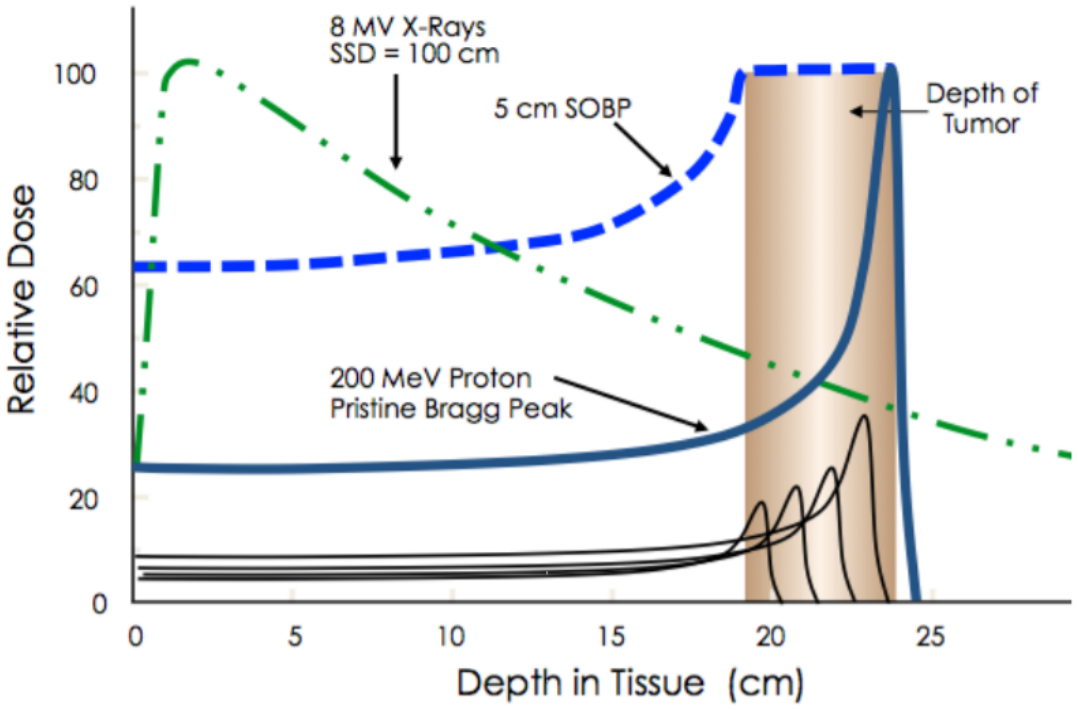

Figure 1.2: Illustration of a depth-dose profile of an 8 MeV X-ray beam (green dash-dotted curve) and a 200 MeV proton beam (blue curve). A variation of the proton beam energy results in the black curves forming the SOBP (dashed blue line) [12].

The depth-dose profile shown in Fig. 1.1 highlights the advantage of using proton beams to deliver a high radiation dose to a specific tumour volume, without compromising the surrounding tissue. Despite this high accuracy, there are uncertainties encountered when such a beam is delivered to the target volume. These uncertainties can be caused either by the treatment planning or by the treatment delivery. With respect to the latter the uncertainties are caused by: patient mispositioning, organ motion or anatomic changes between fractions, such as tumour shrinking or weight loss. The uncertainties from the planning itself result from: estimation of the tumour volume by the clinician and the estimation of the tissue's Relative Stopping Power (RSP) values deduced from X-ray CT [13]. When using photons, a small deviation can be accepted, however, in particle therapy the healthy tissue is immediately damaged. In order to avoid the risks associated with these uncertainties, safety margins are applied in the Planning Treatment Volume (PTV). Usually such margins in proton therapy are [2.5-3]% of the proton range +[2-3]mm, depending on the hospital policy [14]. In order to reduce the safety margins, an accurate in-vivo range verification technique is mandatory, both in proton and ion-beam therapy.

1.2 Ion beam range verification techniques

Over the last years, following the beginning of using particle therapy as a treatment modality, much research has been focused on developing different approaches for *in-vivo* range verification techniques. This section is dedicated to explaining different approaches for *in-vivo* range verification that are based on different types of secondary emission, generated by the interaction of the ion beam with the human body's constituents. Secondary emission can either consist of thermoacoustic waves that arise from shock-like heat deposition in the tissue or from prompt or delayed gamma rays created through nuclear interactions or radioactive decay processes. Some secondary emissions are shown in Fig. 1.3. In the left panel it is possible to see a schematic representation of the generation of an ionoacoustic ultrasound signal, where pulsed, shock-like and localized energy deposition in tissue produces a local increase in temperature, and the resulting thermal expansion launches a thermoacoustic pressure wave. Secondary gamma rays can be produced through two distinct processes. Inelastic nuclear interactions between the beam and the medium constituents can produce short-lived β^+ unstable radioisotopes, such as ^{11}C and ^{15}O, that decay via positron emission, leading to the annihilation of the positrons with electrons to produce pairs of simultaneous 511 keV gamma rays emitted in approximately opposite direction (Fig. 1.3 middle panel). Inelastic nuclear scattering processes, as well as fragmentation reactions, can also result in excited nuclei, which decay to the ground state by emitting multi-MeV prompt gamma rays (Fig. 1.3 right panel) [15].

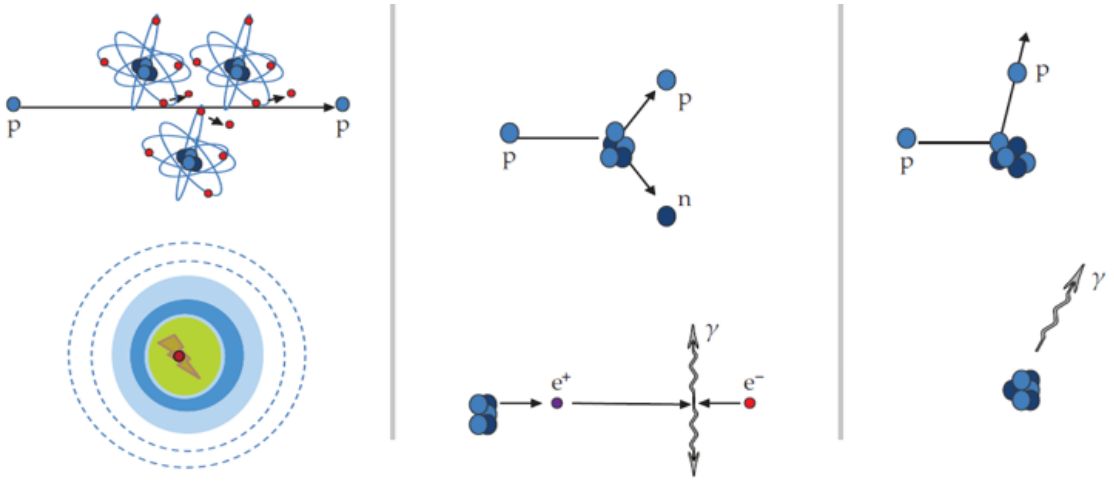

Figure 1.3: Due to the interaction between the proton or ion beam with tissue, different types of secondary emissions can occur. From left to right: ionoacoustic ultrasound signal, positron annihilation γ rays and prompt γ rays [15].

In the following subsections different *in-vivo* range verification approaches, based on the above mentioned secondary emissions, will be presented and discussed.

1.2.1 Ionoacoustic signal detection

The ionoacoustic method is a non-nuclear technique based on the thermoacoustic effect induced by the ion beam [16]. This effect is caused by the deposition of energy in tissue by the ions within a short time of a few microseconds, generating heat in a small tissue volume in the range of millimetres and thus generating an ultrasound signal. The detection of the thermoacoustic waves can provide an accurate localization of the Bragg peak within the patient during the irradiation [17]. Sulak et al. first reported in 1979 the induction of acoustic waves using proton beams and in the 1990s the applicability of this technique was first clinically investigated in Japan at the Proton Medical Research Center Tsukuba [18]. Due to new-generation beam therapy systems that use compact pulsed accelerators and monoenergetic narrow pencil beams, ionoacoustics has gained renewed and growing interest in the research community [15]. The Medical Physics department of LMU latest results in ionoacoustic tomography based on the detection of ion-induced ultrasound waves showed that ion range imaging is possible with submillimetre accuracy [16]. Although this technique seems promising, due to the attenuation of the induced thermoacoustic waves in tissue, its applicability has to be further investigated.

1.2.2 Charged secondary particles

The analysis of the charged particles created during nuclear fragmentation in the patient and subsquently leaving the patients body can also be used to determine the particle range. Amaldi et al. (2010) [19] first proposed using these particles by introducing the method of Interaction Vertex Imaging (IVI), which aims at reconstructing the nuclear emission vertex distribution and correlating it with the Bragg peak position, via the detection of secondary protons [20]. There are two possible approaches for the detector configuration: double-proton detection by means of two forward-located trackers and single-proton detection in coincidence with the incoming carbon ion, detected by means of a beam hodoscope. These two approaches were investigated with the help of Monte Carlo simulations, showing that single-proton imaging is the best solution due to the fact that double-proton imaging reduces too much the statistics of the available signal sample. When using IVI the uncertainties will be mainly due to heterogeneities at the end of the ion path and statistical

fluctuations [21].

1.2.3 Positron-annihilation photons

As mentioned before, during hadron therapy secondary gamma-rays are produced in the patient's body due to interactions of the ion beam in tissue. These interactions can result in positron-emitting isotopes, therefore the use of Positron Emission Tomography (PET) is a promising method for verification of ion beam range, having been first proposed by Maccabee et al. in 1969 [22]. The main β^+ emitting isotopes produced in nuclear reactions between an ion beam and soft tissue, ^{11}C, ^{13}N and ^{15}O, are presented in Table 1.1 [23].

Isotope	**Half-life (min)**	**Mode of Decay (%β)**	**Nuclear reaction channels**
^{11}C	20.4	99.77	^{12}C(p,pn)^{11}C ^{14}N(p,2p2n)^{11}C ^{16}O(p,3p3n)^{11}C
^{15}O	2	100	^{16}O(p,pn)^{15}O
^{13}N	10	100	^{16}O(p,2p2n)^{13}N ^{14}N(p,pn)^{13}N

Table 1.1: Main β^+ decaying isotopes produced in nuclear reactions between an ion beam and soft tissue together with their half-life, decay mode and nuclear reaction channels [23].

So far the only applied method for an *in situ* monitoring of the ion beam range for clinical use is PET imaging. Range verification using PET-based activity measurements can be performed either in-beam (measurement during the irradiation), in-room (measurement immediately after irradiation) or off-line (measurement after irradiation)[24], as illustrated in Fig. 1.4. In-beam PET uses an unconventional PET instrumentation integrated in the beam delivery, having the first proposed prototype been a dual-head PET device installed at the ion therapy beamline of the Lawrence Berkeley Laboratory (LBL) [23]. The main advantage of this technique is that, because the acquisition is performed on-line, the distribution of positron emitters is mostly influenced by the biological washout. However, this technique shows some disadvantages, mainly the geometric constraints due to the need of an opening for the beam portal and flexible patient positioning, leading to the use of double-head PET systems. The use of this configuration leads to poor image quality and, due to the use of specialized PET devices, higher costs. This approach has been used in

some facilities, such as the Gesellschaft für Schwerionenforschung (GSI) in Darmstadt, Germany [25]; the Heavy Ion Medical Accelerator (HIMAC) in Chiba, Japan [26]; the CATANA Proton therapy Center in Catania, Italy [27] and the National Cancer Center (NCC) in Kashiwa, Japan [26]. In order to overcome the system's low sensitivity and limiting field of view, Yamaya et al. at the National Institute of Radiological Science (NIRS) in Japan are currently developing an "OpenPet" system. This system uses Depth-Of-Interaction (DOI) detectors, thus improving the spatial resolution in the gap produced by the reconstruction of images only from oblique lines-of-response [28].

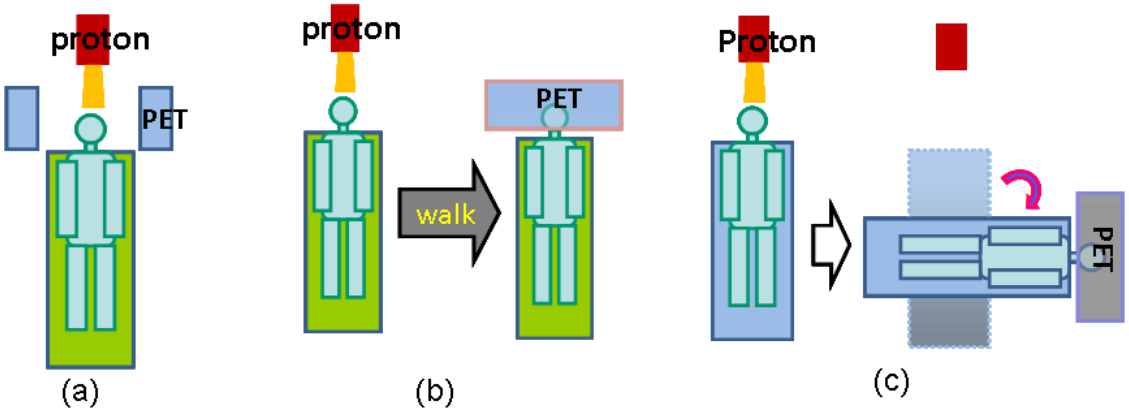

Figure 1.4: There are three different modalities for PMT verification of ion beam range, namely in-beam PET (a), offline PET (b) and in-room PET (c) [23]

The in-room and offline PET methods are easier and more affordable to implement, since a standard PET system is used [29]. The in-room PET technique uses a nearby PET scanner for immediate measurement after the irradiation, detecting reasonable activity, since a short-time passes between the irradiation and measurement. As expected the image quality is inferior to the one acquired with the in-beam PET, since there is a reduction of the statistics. Moreover, there is the need to have PET equipment allocated only for the range verification. The less costly solution is to use the offline PET technique that uses a conventional PET scanner, which is also used for diagnosis, in a nearby room. Nonetheless, due to the rapid decay and biological washout, the images acquired with this technique predominately show activity from radioisotopes with a longer half-time than the time it takes to transfer the patient, thus focusing on the ^{11}C activity. Furthermore, a potential mispositioning of the patient can increase uncertainties such that a prolonged patient scan is required to compensate for the low activity signal strength [24].

1.2.4 Prompt gammas

1.2.4.1 Prompt-gamma spectroscopy

Prompt gamma-ray spectroscopy is a recent method currently being developed at the Massachusetts General Hospital in Boston, that consist on verifying the range of a proton beam by directly relating measurements of discrete prompt gamma-ray lines, mainly induced from ^{12}C and ^{16}O (since they are the main isotopes in human tissue), to nuclear reaction cross sections. The aim of this approach is to develop a method entirely based on quantitative physics models that is robust in the presence of tissue with an unknown elementary composition [30]. In order to characterize the prompt gamma-ray emission differential cross sections, measurements were performed along the lateral side of the proton beam path for energies in the 0-150 MeV range in a tissue equivalent phantom. The performance of the prototype was evaluated with a proton beam, showing a precision of 1.0-1.4 mm [30].

1.2.4.2 Prompt-gamma timing

The prompt gamma timing method is based on the transit time of the therapy particles from entering the patient's body until stopping in the target volume.

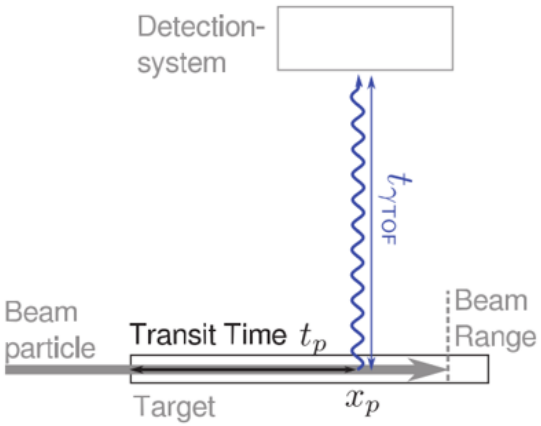

Figure 1.5: Prompt gamma-ray emission during particle irradiation [31].

This transit time is about 1-2 ns in case of protons with a 5-20 cm range, and can be measured through the time difference between the time of entrance to the irradiation target and the arrival time of the corresponding prompt gamma-rays at the detector. This time difference not only incorporates the particle transit time through the material (t_p), but also the time of flight ($t_{\gamma TOF}$) of the prompt gamma

to the detector [31], as it is shown in Fig. 1.5. The transit time becomes larger as the ion interaction is located more deeply in the target volume. This technique for ion beam range verification, first proposed by Testa et al. [32] in 2010, is still under investigation for clinical use. However, recent studies [31, 33] have shown promising results.

1.2.4.3 Compton Camera

The use of a Compton camera for medical imaging was first proposed in [34]. The Compton camera uses the registration of successive interactions of the incident photons in position-sensitive detectors. From these interactions it is possible to exploit the respective Compton scattering kinematics induced by the detector material, allowing for the reconstruction of the origin of incident gamma rays via the determination of the Compton scattering angle. The direction of an incident photon can be restricted to a cone spanned by the Compton scattering angle and, via the superposition of multiple cones (via several incident photons), it is possible to derive the vertex of the photon generation. This approach, when compared to the ones mentioned before, has the advantage of being able to provide 3-D images. The design of the Compton camera differs, depending on whether or not Compton-scattered electrons are intended to be tracked. The simplest design of a Compton camera, where the Compton kinematics is only based on the scattered photon, requires two detection stages: a scatter detector and an absorber. The scatter detector is usually formed by a low-Z material in order to increase the probability of the Compton scattering interaction, while the absorber detector, placed behind the scatterer, is made of a high-Z material to enhance the photo-absorption efficiency. The incoming photon interacts with the scatterer and is deflected, transferring part of its energy to the Compton-scattered electron, while the scattered photon is absorbed in the absorber detector. The energy and interaction position of the incident photon is measured in both components of the camera. Consequently the Compton scattering kinematics enables the calculation of the Compton scattering angle θ, according to the following equation:

$$cos(\theta) = 1 - m_e c^2 \left(\frac{1}{E_{\gamma,2}} - \frac{1}{E_{\gamma,1}} \right) \tag{1.1}$$

where $m_e c^2$ is the electron rest energy and $E_{\gamma,1}$ and $E_{\gamma,2}$ are the energy of the incident and scattered photon, respectively. This scattering angle represents the opening angle of the so-called Compton cone, whose surface indicates the possible

origin of the incident γ rays. To constrain this position several Compton scattering events need to be reconstructed in order to obtain their intersection and therefore determine more accurately the photon source position. By replacing the single scatterer by multiple thin detector layers the electron tracking is enabled. The additional information gained from the Compton recoil electron helps to enhance the camera reconstruction efficiency and the camera sensitivity to the photon source position by reducing the Compton cone to an arc segment.

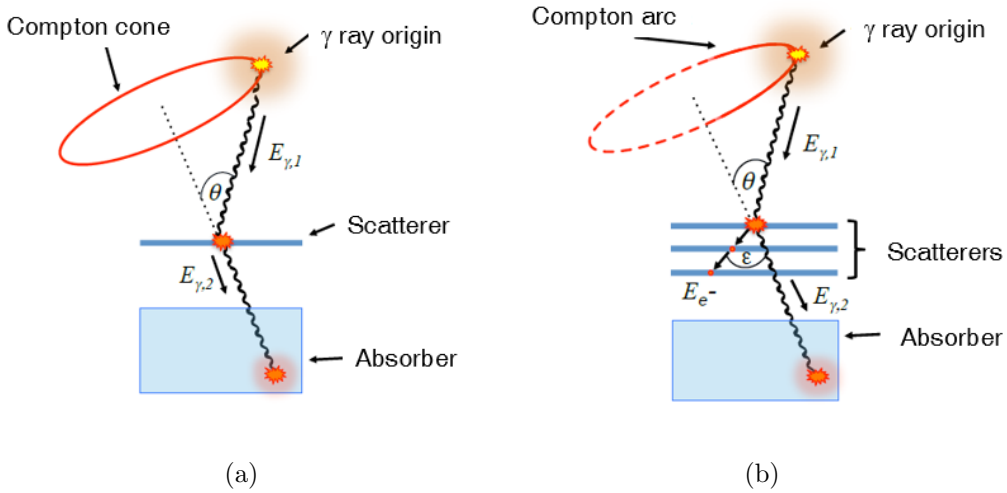

(a) (b)

Figure 1.6: Illustration of the basic principle of a Compton camera with only one scatterer (a) or with several scatterers (b). When using only one scatterer the Compton scattering angle (θ) defines the Compton cone that indicates the possible gamma-ray source position. By adding more scatterers it is possible to track the recoil Compton electron, reducing the probability of the source position from a cone to an arc segment [5].

Different detector configurations have been investigated in groups all around the world, varying in detector materials, configuration and geometry. In Lyon, a detection system that combines a beam hodoscope together with the Compton camera is under development. The hodoscope tags the incident ions and the Compton camera detects the emitted prompt gamma rays. Consequently, the prompt-gamma origin is reconstructed by intersecting the ion trajectory given both by the hodoscope and the Compton camera [35]. This Compton camera prototype is formed by double sided silicon strip detectors ($90 \times 90 \times 2$ mm^3, 2×64 strips) as a scatter and an absorber detector composed of 100 BGO blocks ($38 \times 35 \times 30$ mm^3 for each block). Geant4 simulations have been performed showing promising results for this setup [36]. In Texas, at the Department of Radiation Physics of the University of Texas, a Compton camera based solely on semiconductor detectors is being studied with

simulations for a three-stage system using germanium detectors. The advantage of a three-stage Compton camera is that it does not rely on full absorption of the gamma ray in order to determine the initial spatial and energy information necessary for imaging reconstruction [37]. In Tokyo, a handheld Compton camera based on pixelated Ce:GAGG scintillators, consisting of two scattering layers and an absorbing layer was developed and is under experimental trials [38]. The results obtained so far show that the camera has achieved a high efficiency for high-energy gamma rays and a reduced acquisition time. A prototype consisting of a scatter layer of cadmium zinc telluride (CZT)($2 \times 2 \times 0.5$ cm^3) and a lutetium oxyorthosilicate (LSO) absorber ($5.2 \times 5.2 \times 2$ cm^3) was commissioned at the OncoRay-National Center for Radiation Research in Oncology in Dresden. A three-plane Compton camera prototype based on $LaBr_3$(Ce) crystals coupled to SiPMs was developed in Valencia. This camera, named MACACO, consists of three layers; the first one made of a $LaBr_3$(Ce) crystal ($27.2 \times 26.8 \times 5$ mm^3) and the second and third made of two $LaBr_3$ crystals (35×36 mm^2) of 5 and 10 mm thickness, respectively. Each layer is coupled to four SiPM arrays. Recent experimental results using ^{22}Na and ^{88}Y sources, at a 4 cm distance from the first detector, revealed a position resolution (FWHM) of 4 and 3.5 mm, respectively [39]. Lastly, a Compton camera prototype with electron tracking capability is under development at Ludwig-Maximilians-Universität Munich (LMU). This thesis will present a collaboration on the development of this prototype, and therefore the camera will be further discussed in Chap. 3.

1.2.4.4 Gamma-PET

Due to the interaction of the hadron beam with the human tissue not only 511 keV positron annihilation photons are produced, but there is also the possibility of an emission of a third prompt γ-ray originated from the deexcitation of an excited β^+-decay daughter nucleus. The gamma-PET technique makes use of this third γ-ray by combining a PET system with one or several Compton cameras in order to detect the two 511 keV annihilation photons in coincidence with the third photon. By reconstructing the source position of the prompt photon and determine the Line-Of-Response (LOR) from the positron annihilation photons it is possible to reconstruct the source distribution in 3 dimensions from individual events.

In Fig. 1.7 it is possible to see the schematical geometry of the γ-PET setup used for simulations using four Compton cameras. This nuclear medical imaging technique, presented by Lang et al. [40], is able to reach sub-millimeter spatial resolution. Latest results have achieved a spatial resolution around 0.4 mm (FWHM)

in each direction of a ^{22}Na point source, showing that this technique has promising applications also for nuclear medicine, where ^{44}Sc is an intensively studied candidate for diagnostics [41].

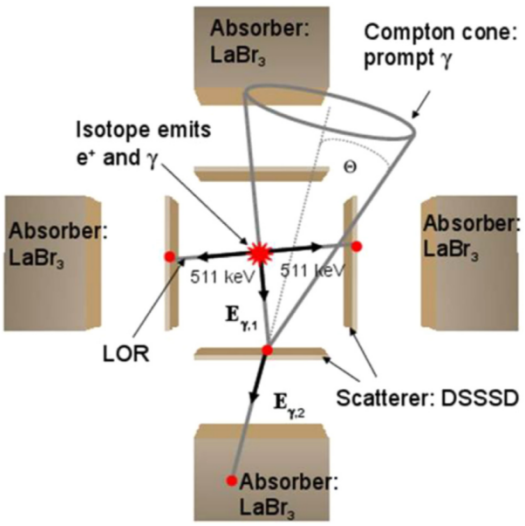

Figure 1.7: Schematics of the principle of the γ-PET technique. The emitted γ-ray will undergo Compton scattering and subsequently will be absorbed in an absorber detector, allowing for the determination of the position and energy of the final interaction. The intersection of the LOR, determined by the positron annihilation, with the Compton cone will give the source origin in 3 dimensions [40].

1.3 Thesis context and objective

The Compton camera prototype system presented in this thesis is currently under development at the chair of Medical Physics at the Ludwig-Maximilians-Universität Munich (LMU). During its commissioning, done in the framework of a previous PhD thesis [5], the two main camera components chosen were: a $LaBr_3$:Ce^{3+} crystal scintillator, acting as an absorber detector, read out by a 16 $\times$ 16 multianode Photomultiplier Tube (PMT) (H9500 from Hamamatsu [42]), which features 256 segments each with an area of 3 $\times$ 3 mm^2 and a scatter component composed by six layers of Double-Sided-Silicon Strip Detectors (DSSSDs), each with an active area of 50 $\times$ 50 mm^2 and a thickness of 0.5 mm. However, recent studies preformed in the framework of two Master theses [1, 2], have shown, through software manipulations, that an improved spatial resolution of the absorber detector can be achieved when using a reduced number of 64 readout channels. This means that by reducing the number of readout channels we cannot only simplify the whole system and reduce the readout electronics, but also improve the system performance. Therefore, this

thesis' main objective will be to experimentally study the performance of a recently acquired absorber detector, a $LaBr_3:Ce^{3+}$ monolithic scintillator, read out by an 8×8 multianode position sensitive PMT (H8500 from Hamamatsu [43]) featuring only 64 segments with an overall area of 49×49 mm. Namely the detector's spatial resolution was the subject of an intensive study. This work begins with an overview of the physics behind the interaction of radiation with matter and the relevant detection principles in Chap. 2. In Chap. 3 the LMU Compton camera prototype characterization is given with special focus on its new absorber component and readout electronics, since they make up the basis of this thesis' investigations. The characterization of the absorber component under study is presented in the following Chap. 4. Firstly the time resolution, previously determined in the scope of an ongoing PhD thesis, and the relative energy resolution, acquired has a 2D map covering the crystal's surface and evaluated for different PMT supply voltages, are presented. The photon interaction determination follows, where the methods and algorithms used are described in detail and the light amplitude reference libraries are presented. To conclude Chap. 4, the spatial resolution of the $LaBr_3:Ce^{3+}$ monolithic scintillator read out by a 64-segmented PMT is experimentally determined, as a function of different parameters, constituting the main contribution of this thesis. Moreover, during this chapter comparisons will be given between the experimentally obtained results and the ones previously acquired by software manipulation of the raw data. This thesis ends with Chap. 5, where overall conclusions from the work presented before are given together with an outlook of the work that is being pursued in our group.

2

Radiation interaction and γ-ray detection

The purpose of the second chapter of this thesis is to give an overview of the physics behind the interaction of radiation with matter, as well as the relevant detection principles. The first part of this chapter describes the three main interactions that occur when electromagnetic radiation interacts with matter: photoelectric effect, Compton scattering and pair production. The second part focuses on the detection of γ rays such as they are produced in the interaction between energetic particle beams and organic tissue. More specifically, a short description of radiation detectors is given, followed by a more thorough explanation of scintillation detectors, as being the most relevant detectors type for this thesis project.

2.1 Photon interaction with matter

Radiation can be classified into two main categories: non-ionizing, when the radiation does not ionize matter, and ionizing, when it does. As can be seen in Fig. 2.1, ionizing radiation can be further divided into directly and indirectly ionizing radiation. Photons are indirectly ionizing radiation and can interact with the atom, nucleus or an orbital electron of the whole absorber. Its interaction with the nucleus can be directly with the nucleus itself (photo disintegrations) or via its electromagnetic field (pair production). Moreover, the interactions between the photon and an orbital electron can occur with either a loosely bound electron (Thomson scattering, Compton scattering, triplet production) or with a tightly bound electron (photoelectric effect, Rayleigh scattering).

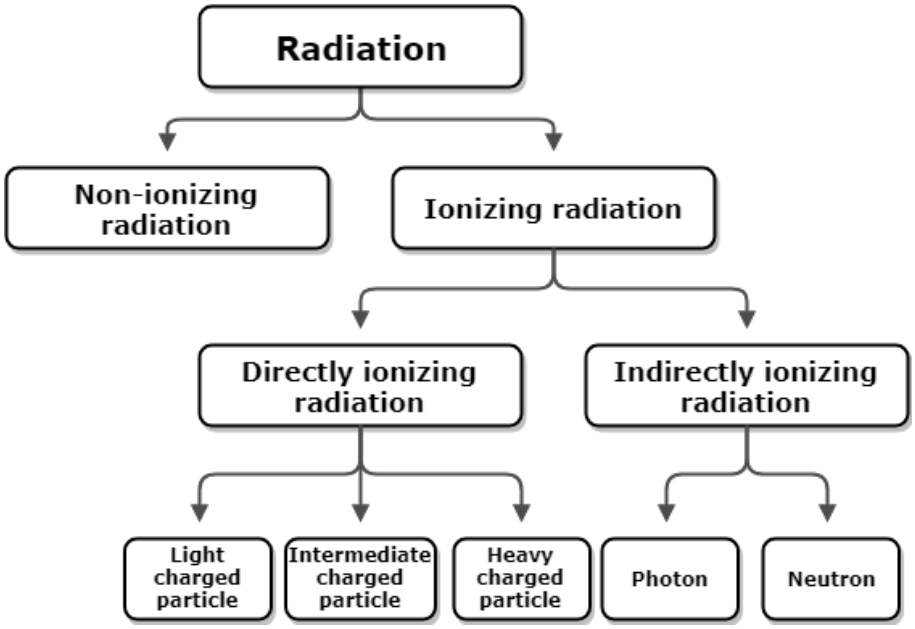

Figure 2.1: Classification of radiation via its interaction with mattter.

The probability of an interaction depends on the photon energy, density and atomic number of the absorber. The three major interaction processes used in detection systems are the photoelectric effect, Compton scattering and, if energy allows, pair production.

2.1.1 Photoelectric Effect

The photoelectric effect is the interaction between a photon and a bound electron of an absorber atom, where the incident photon transfers all its energy to the electron. This interaction is shown schematically in Fig. 2.2. The ejected electron, called photoelectron, is ejected with kinetic energy Φ if the photon energy exceeds the binding energy of the previously bound electron. This kinetic energy is equal to the difference between the incident photon energy hv and the electron binding energy, E_b.

$$\Phi = hv - E_b \tag{2.1}$$

The emission of the photoelectron will result in a vacancy in the atomic shell, which will be filled by a higher-shell electron. The resulting transition energy will be emitted either as a characteristic photon or as a series of, one or more, Auger electrons.

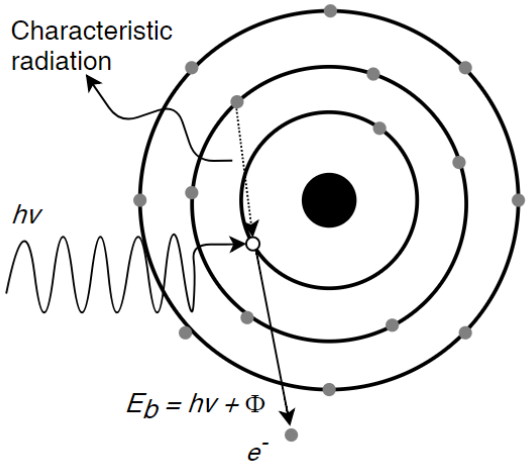

Figure 2.2: Schematic diagram of the photoelectric effect.

As can be seen in Fig. 2.3, the atomic cross section τ_a represented by the mass attenuation coefficient, as a function of the incident photon energy hv has a sawtooth-like structure. The sharp discontinuities, or absorption edges, occur when the photon energy coincides with the binding energy of a particular electron shell.

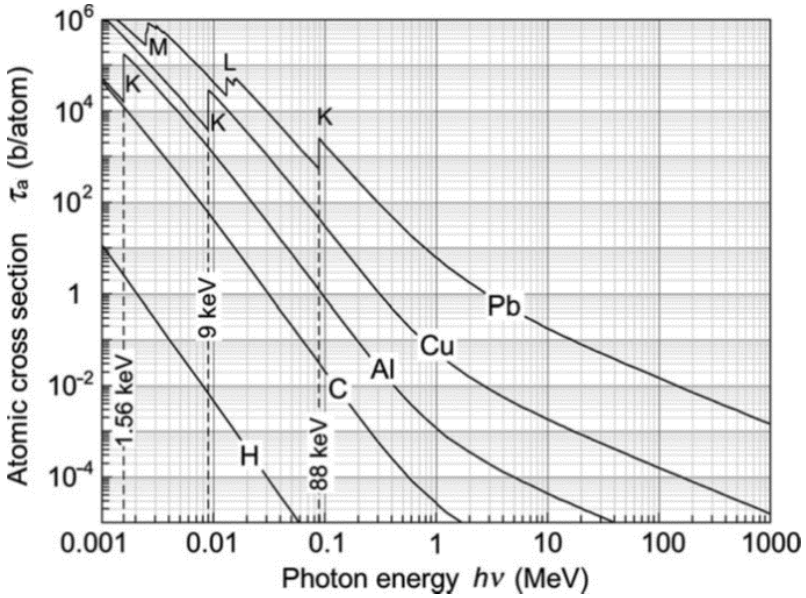

Figure 2.3: Photoelectric atomic cross section as a function of the photon energy for different absorbers [44]. K, L and M-shell absorption edges are specifically labelled.

Although there is no valid analytic expression for the cross section per atom over all ranges of photon energy and atomic number Z of the absorber a rough

approximation is given by:

$$\tau_a \cong \text{constant} \times \frac{Z^n}{E_\gamma^{3.5}} \tag{2.2}$$

where n is the power for the Z dependence of τ_a and it varies between 4 and 5. Due to the need of simultaneously conserving the total energy and momentum, the photoelectric interaction cannot occur between a photon and a free electron.

2.1.2 Compton Scattering

Compton scattering is the incoherent or inelastic interaction between an incident photon and a loosely bound orbital electron of an absorber atom. Fig. 2.4 illustrates this interaction, where part of the incident photon energy is transferred to the electron initially assumed to be at rest, resulting in a scattered photon with an energy that is smaller than the one of the incident photon, as well as a recoil electron with a recoil angle of ϕ. The Compton photon scattering angle θ is defined as the angle between the incident photon direction and the scattered photon direction, whereas the recoil electron angle ϕ is the angle between the incident photon direction and the direction of the recoil electron.

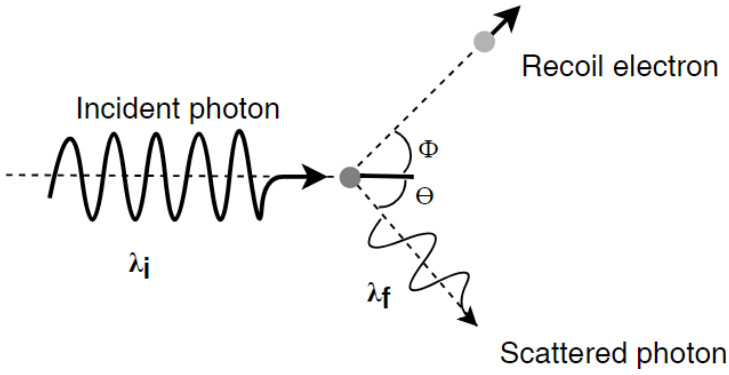

Figure 2.4: Schematic diagram of the Compton scattering process.

In contrast to the photoelectric effect, the conservation of energy and momentum allows for this interaction to also occur with a free electron. These conservation laws can be used to derive the Compton wavelength shift relationship between the

incident and scattered photon

$$\Delta\lambda = \lambda_f - \lambda_i = \lambda_C(1 - cos\theta) = \frac{\pi h}{m_e c}(1 - cos\theta) \tag{2.3}$$

where λ_f and λ_i are the wavelengths of the scattered and incident photon, respectively, m_e is the electron rest mass, h is the Planck constant and c is the speed of light. Due to the conservation of total energy and the relation between energy and wavelength it is possible to derive Eq. (2.3) in order to express the scattered photon energy E_f as a function of θ and of the incident photon energy E_i:

$$E_f = \frac{E_i}{1 + \frac{E_i}{m_e c^2}(1 - cos\theta)} \tag{2.4}$$

The scattering angle θ has a range between 0 and π [radians], while the corresponding recoil electron angle ϕ ranges from $\frac{\phi}{2}$ (for $\theta = 0$) to $\phi = 0$ (for $\theta = \pi$). This means that the recoil electron angle is confined to the forward hemisphere with respect to the direction of the incident photon, while the photon scattering angle can experience scattering in forward, sideward, or backward direction. The total energy of the recoil electron is the sum of its kinetic energy and its rest energy ($E_e = m_e c^2 + E_k^e$). The kinetic energy of the electron depends on the incident photon energy and photon scattering angle, and it can be expressed, using the energy conservation principle from Eq. (2.3), by

$$E_k^e = E_i - E_f = E_i \left[\frac{\frac{E_i}{m_e c^2}(1 - cos\theta)}{1 + \frac{E_i}{m_e c^2}(1 - cos\theta)} \right] \tag{2.5}$$

For a given incident photon energy the kinetic energy of the electron will range from a minimum value of zero, for a scattering angle of 0 degrees, to a maximum value given by

$$(E_k^e)^{\max} = E_i \left(\frac{2\frac{E_i}{m_e c^2}}{1 + 2\frac{E_i}{m_e c^2}} \right) \tag{2.6}$$

for a scattering angle of π (backscattering). This means that when the incident photon is barely deflected (forward scattering) there is minimum energy transfer to the electron, while the maximum energy transfer occurs in the scenario of backscattering.

The angular distribution of scattered gamma-rays can be described by the

Klein-Nishina formula, first proposed in 1928, for the differential scattering cross section

$$\frac{d\sigma}{d\Omega} = Zr_0^2 \left(\frac{1}{1+\alpha(1-cos\theta)} \right)^2 \left(\frac{1+cos^2\theta}{2} \right) \left(1 + \frac{\alpha^2(1-cos\theta)^2}{(1+cos^2\theta)[1+\alpha(1-cos\theta)]} \right) \tag{2.7}$$

where $\alpha \equiv \frac{hv}{m_0c^2}$ and r_0 is the classical electron radius. In Fig. 2.5 it is possible to observe the cross section as a function of the scattering angle for various incident photon energies. A tendency for forward scattering is observed for high values of γ-ray energy.

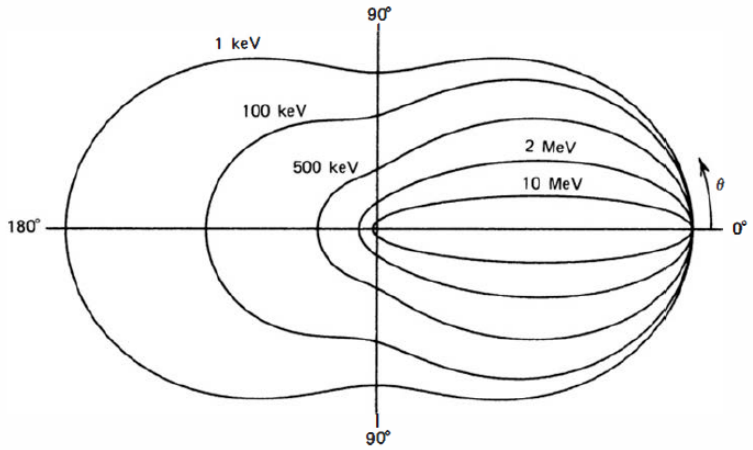

Figure 2.5: Compton scattering cross section as a function of the photon scattering angle for various incident photon energies. With the increase of the photon energy, the scattering angle becomes smaller and forward scattering increasingly dominates [45].

2.1.3 Pair Production

Pair production occurs when an incident photon with an energy exceeding two times the electron rest energy ($2m_ec^2$ =1.022 MeV) directly interacts with the atomic nucleus converting its energy into an electron-positron pair, as illustrated in Fig. 2.6. The pair produced has a total energy of $E_{\text{pair}} = 2\gamma m_e c^2$ and a total momentum of $p_{\text{pair}} = 2\gamma m_e v$.

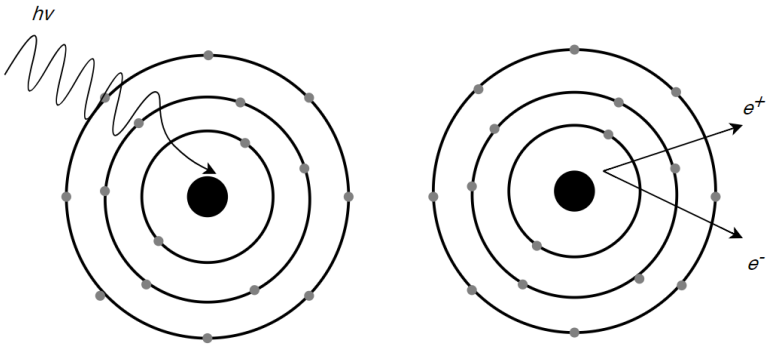

Figure 2.6: Schematic representation of pair production.

The two particles produced have identical rest masses and rest mass energies. Due to charge conservation their charge magnitude is the same but of opposite sign, with the positron e^+ being positive and the electron e^- negative. The electron is considered free and stationary, while the positron soon loses all of its kinetic energy in thermalizing collisions before undergoing annihilation with an orbital electron. This annihilation results in two photons each with an energy equal to $m_e c^2 = 0.511$ MeV, that move in (almost) opposite directions thus ensuring charge, energy and momentum conservation. Although there is no simple expression for the probability of this interaction to occur, its magnitude varies, approximately, with the square of the absorber atomic number Z^2.

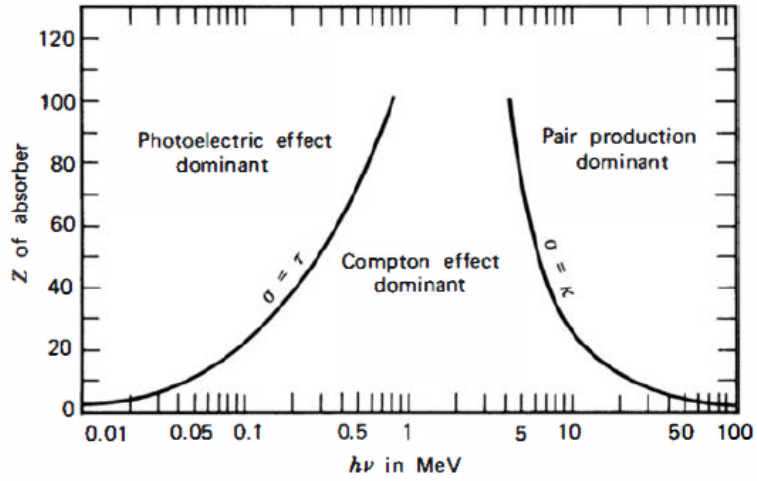

Figure 2.7: Relative importance of the three major types of γ-ray-matter interaction. The lines show the values o Z and $h\nu$ for which two neighbouring effects are equally probable [45].

The relative importance of these three processes (photoelectric effect, Compton scattering and pair production) for absorbers with different atomic number (Z) and

gamma-ray energies ($h\nu$) is illustrated in Fig. 2.7. As it can be seen, the photoelectric effect dominates for lower energies. The line at the left represents the energy at which this effect and the Compton scattering are equally probable as a function of the absorber atomic number. In turn, the line on the right represents the energy at which Compton scattering and pair production are equally probable, being that pair production is more likely to happen for higher energies.

2.2 Radiation Detectors

The basic principle of any radiation detector is the interaction of radiation with matter, which happens through a variety of different mechanisms. The three main interactions that occur in a γ-ray detector via photon-matter interactions were previously explained in Sect. 2.1. Free electric charge carriers resulting from the interaction are collected. The detector's performance can be judged through the measurement of several physical characteristics, such as energy and time resolution. The most important characteristics in the context of this thesis are:

1. **Energy resolution**, which measures the ability of a detector to distinguish between gamma-rays with energies that are close to one another. Therefore, the lower the value the better the detector can distinguish between two photons whose energies lie near each other. This characteristic can be acquired by examining the response of the detector to a monoenergetic source of radiation. Fig. 2.8 illustrates an energy spectrum acquired with a ^{137}Cs calibration source, where a 662 keV photo-peak is present.

   The (relative) energy resolution can be obtained from the energy spectrum by dividing the Full Width at Half Maximum (FWHM), defined as the width of the distribution at a level that is half the maximum ordinate of the peak, by the location of the peak centroid:

   $$ER = \frac{FWHM}{E_0} = \frac{\triangle E}{E} \times 100[\%] \tag{2.8}$$

   For peaks whose shape is Gaussian with standard deviation σ, the FWHM is given by 2.35σ. The energy resolution is therefore a dimensionless fraction, often expressed as a percentage. Normally, scintillation detectors used in γ-ray spectroscopy show an energy resolution (at 662 keV) between 3% and 10%, whereas the energy resolution of semiconductor diode detectors can be as low as $\leq 1\%$. Due to some fluctuations, the energy resolution of a detector

can be imperfect. These fluctuations can arise from drifts of the operating characteristics of the detector during the course of the measurements, random noise within the detector and instrumentation system, and statistical noise arising from the discrete nature of the measured signal itself [45].

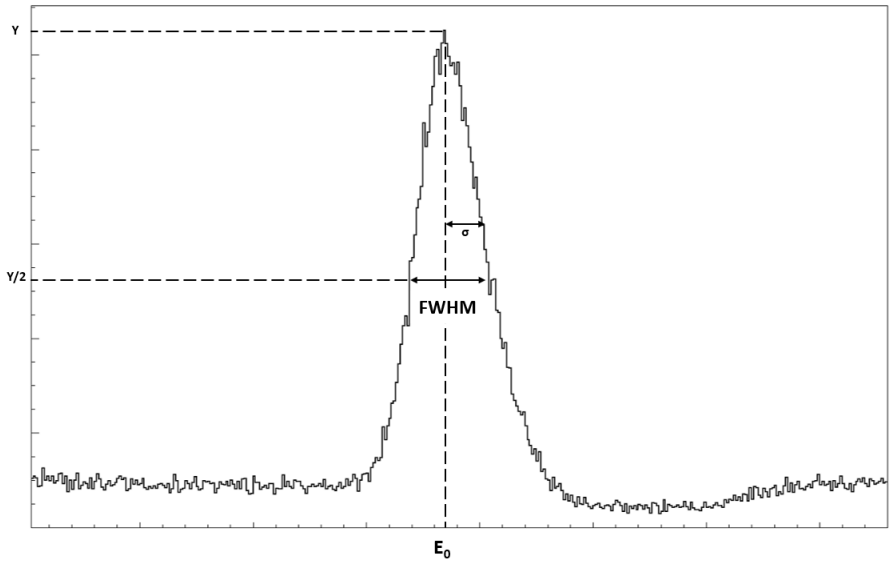

Figure 2.8: Energy spectrum acquired with a ^{137}Cs calibration source. In order to obtain the energy resolution the photo-peak FWHM value and the location of its centroid (E_0) need to be determined.

2. **Time resolution**, gives information on the minimal interval between two interactions that can be temporally resolved. It is defined as the FWHM of a time peak obtained by measuring the distribution of the registered time intervals between two simultaneous interactions, as for example the detection of two coincident γ-rays emitted by a calibration source (e.g. ^{60}Co).

3. **Detection efficiency**, defined as the percentage of the radiation emitted by the source that is detected. In perfect conditions the counting efficiency can be up to 100%. However, realistic detectors will never reach exactly 100% efficiency, dependent on the interaction mechanism, detection type, material properties, charge collection, field properties, etc. The detection efficiency can either be intrinsic, where it depends only on the detector properties, or absolute, where it also depends on the details of the counting geometry. The absolute efficiency ε_{abs} is given by the ratio between the number of events recorded and the number of radiation quanta emitted by the source, whereas the intrinsic efficiency ε_{int} is given by the ratio between the number of events recorded and the number of radiation quanta incident on the detector. Consequently, ε_{int} does not consider all emitted photons, but only the ones entering

the detector, while ε_{abs} takes into account the solid angle covered by the specific detector. The detection efficiency can also be characterized by the nature of the event recorded. A photopeak efficiency can be used instead of the total efficiency, counting only the interactions that deposit the full energy (i.e. photo-peak energy) instead of considering all recorded events. This full-energy peak can be seen at the high-energy side of the differential pulse height spectrum illustrated in Fig. 2.9 [45]. In turn, the events that only deposit a fraction of the incident radiation energy appear on the left of this photopeak. Therefore, in order to obtain the number of full-energy events, the total area under the full-energy peak must be determined. Usually, the photopeak efficiency is used in spite of the total efficiency, since the number of full energy events is not sensitive to perturbing effects such as, for example, scattering from surrounding objects. It is important to know the detector efficiency, e.g., in order to measure the absolute activity of a radioactive source.

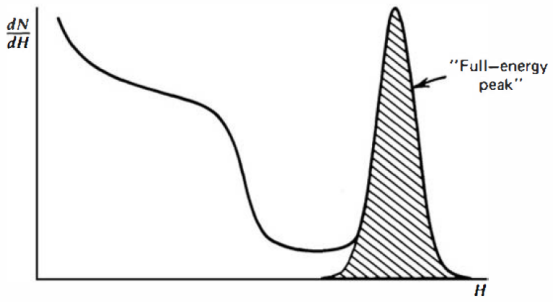

Figure 2.9: Full-energy peak in a differential pulse height spectrum [45].

4. **Dead time**, defined as the amount of time that must separate two events in order for them to be recorded as two separate pulses. If an event occurs too quickly following a preceding event it will be lost due to the dead time. This effect is more probable in cases where there are high counting rates and therefore there is a need to include some correction in order to compensate for these losses.

There are several different types of radiation detectors, however, in this chapter, the focus will be laid on scintillation detectors, since the absorber component of the LMU Munich Compton camera, being the subject of study in this thesis, is a $LaBr_3$:Ce^{3+} monolithic crystal, which belongs to this category.

2.2.1 Scintillation Detectors

Scintillation is a luminescence process induced by ionizing radiation in a transparent dielectric medium. More specifically, a scintillator is any material that after irradiation by an energetic photon can release a multitude of low-energy visible or near-Ultraviolet (UV) photons. In a scintillation detector gamma-rays interact with the scintillator material, leading excited atoms in the material to de-excite to a lower-energy state and thus emitting scintillation light. The scintillation light is typically detected by a photomultiplier tube and amplified to a measurable electronic signal. A typical scintillation detector setup can schematically be seen in Fig. 2.10.

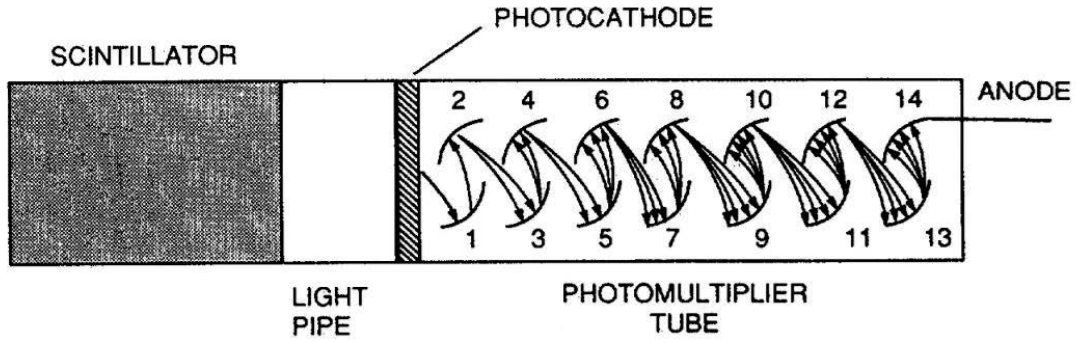

Figure 2.10: Sketch of the typical arrangement of components in a scintillation detector. An incoming photon will interact with the scintillator leading to the emission of scintillation light, which will therefore be transported through the light pipe towards the photocathode of the photosensor. There, the scintillation light is converted into electric charges leading to the generation of an electronic signal [46].

An incoming photon interacts with the scintillator crystal, leading to the emission of visible or UV scintillation light, which is transported through a light guide into the photocathode of the PMT that acts as a photosensor. There the scintillation light is converted into electric charges (electrons), which are then accelerated by a strong electric field in the PMT. Due to the acceleration, the electrons collide with the electrodes (called dynodes) in the tube, releasing additional electrons and thus increasing the electron flux. This flux is multiplied in a multi-stage amplification process by a factor of 10^4-10^6 from the photocathode to the anode and the final charge is then collected in the anode where a measurable electronic signal, proportional to the energy deposited by the incoming γ-ray in the scintillation medium, is generated.

The choice of scintillator material is mainly influenced by the intended application. Scintillators can be found in both organic and inorganic materials, as explained

below.

In an organic scintillator the fluorescence process, meaning the prompt emission of visible radiation from the material following its de-excitation, occurs from transitions among energy levels of a single molecule. The emission of fluorescence light is therefore independent of the molecular species physical state. The energy level scheme of these materials has symmetry properties, making them suitable for producing a measurable light output in the visible or near UV spectral range. Depending on the deposited energy in the medium, an electron is excited to an energy state and then de-excited rapidly back to the ground state emitting fluorescence light. Because the decay time of most organic scintillators is only a few nanoseconds the prompt scintillation component is relatively fast.

On the other hand, the electrons in an inorganic scintillator have only discrete bands of energy available, due to the energy band structure found in the crystal lattice. The deposited energy in the scintillator, created by the interaction of the photon with the lattice atoms, leads to the excitation of an electron from the lower band, called valence band, across the band gap to the empty conduction band, creating electron-hole pairs. The emission of a photon, with an energy that exceeds the visible or near UV spectral range due to the high width of the gap is caused by the de-excitation of the electron back to the valence band. In pure crystals this process is inefficient, therefore, to enhance the probability of the emission of visible photons, dopants, called activators, are introduced to the lattice structure. These are typically fluorescent ions such as thallium (Tl) or cerium (Ce). The activators create special sites in the lattice that make possible the creation of energy states in the band-gap region, through which the electron can recombine with the positive hole, emitting therefore a lower energy photon in the visible spectral or near UV range that can activate the PMT. Fig. 2.11 illustrates this mechanism.

These excitation sites, called recombination or color centres, determine the emission structure of the scintillator. Due to the luminescence through the activator the bulk scintillator crystal is transparent for the scintillation light.

The most important characteristics of an inorganic scintillation detector are:

- **light yield**, i.e. the number of emitted visible photons per deposited MeV of incident photon energy.
- **decay time**, i.e. how long scintillation photons are released after a radiation interaction, which is determined by the mean lifetime of the states of the activator sites.

- **energy resolution**, $\frac{\Delta E}{E}$, and its linearity over the energy range of interest.
- **stopping power**, which depends on the Z-value of the material and determines the efficiency of the detector.

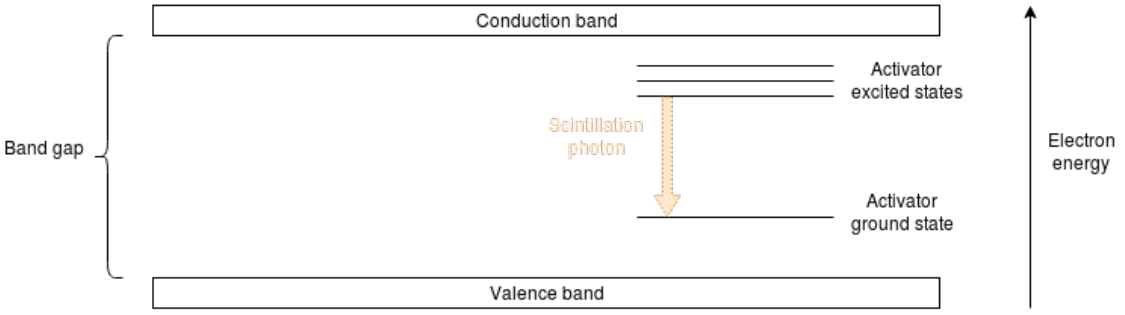

Figure 2.11: Energy band structure of an inorganic scintillator. Activators are introduced to the lattice structure of the material creating activator states. When an electron-hole pair is created it travels through the scintillator until it is captured by the activator states, causing the emission of scintillation light in the visible or near UV spectral range.

Some properties of the most commonly used organic and inorganic scintillators are presented in Table 2.1. As it can be seen, organic scintillators exhibit very fast decay times τ being the best choice for high-rate applications. However, inorganic scintillators have a higher light yield, which is nearly proportional to the deposited radiation energy, leading to a reduction of the statistical fluctuation and therefore resulting in a better time and energy resolution. Moreover, they are a favourable choice for gamma-rays and high energy charged particle detection, since inorganic crystals exhibit a high Z-value and density. Some inorganic scintillators are hygroscopic, as for example $LaBr_3:Ce^{3+}$, meaning that they have a high tendency to absorb moisture from the surrounding environment. Although being hygroscopic, $LaBr_3:Ce^{3+}$ and $CeBr_3$ exhibit the highest light yield and very good energy and time resolution. For these reasons, at the time of writing, the LMU Compton camera has two absorber components under study, a $LaBr_3:Ce^{3+}$ and a $CeBr_3$ scintillator.

Material	ρ (g/cm^3)	Z_{eff}	τ (ns)	LY (ph/MeV)	$\frac{\Delta E}{E}$ (%)	Hygr.?
Inorganic						
NaI(Tl)	3.67	51	230	38000	5	yes
$LaCl_3$:Ce^{3+}	3.79	60	28	46000	3	yes
$LaBr_3$:Ce^{3+}	5.08	47	16	63000	3	yes
$CeBr_3$	5.2	46	17	68000	4	yes
$Bi_4Ge_3O_{12}$(BGO)	7.13	74	300	8200	12	no
Lu_2SiO_5 :Ce^{3+}(LSO)	7.4	66	47	25000	10	no
Gd_2SiO_5 :Ce^{3+}(GSO)	6.71	59	60	9000	10	no
Y_2SiO_5(YSO)	4.54	34	70	24000	10	no
Organic						
BC-404, EJ 204, NE 104	1.03	-	1.8	∼10000	-	-
BC-408, EJ 200, Pilot F	1.03	-	2.1	∼10000	-	-
BC-418, EJ 228, Pilot U	1.03	-	1.4	∼10000	-	-

Table 2.1: Properties of common inorganic and organic scintillators. The table shows, from left to right, the mass density ρ, the effective atomic number Z_{eff}, the decay time τ, the light yield LY, the relative energy resolution $\frac{\Delta E}{E}$ at 662 keV (for small cylindrical crystals) and the hygroscopic characteristics of the material [45, 47].

3

Layout of the LMU Compton Camera prototype

Ion beam range verification can be accomplished by use of a Compton camera which exploits the Compton scattering kinematics of the incident energetic prompt photons induced in the detector material, as previously explained in Sect. 1.2.4.3. The LMU Compton camera prototype will be explained in this chapter. Both scatter and absorber components will be described, as well as the signal processing and data acquisition. Emphasis will be given to the absorber component of this system, since it constitutes the main focus of this thesis. To conclude the chapter a brief overview of the Camera's mechanical setup will be shown.

3.1 Compton Camera prototype

Besides allowing to discriminate the signal of prompt γ-rays that result from the interaction between the proton or ion beam and the organic tissue, the LMU Compton camera prototype also tracks the recoil Compton electron. The electron tracking enables the reconstruction of those events that are not fully absorbed in the last stage of the Compton camera, thus increasing the reconstruction efficiency. Due to this capability, the scatter component needs to have multiple layers to allow for the tracking of the electron trajectories by detecting interactions between the electron and the detector material. Furthermore, to avoid an early absorption of the Compton electron, the scatter detectors need to be thin enough, while providing a high scattering probability in order to produce sufficient Compton-scattering events. Therefore, the scatter detector component is composed of six layers of DSSSD, each with an active area of 50×50 mm^2, a thickness of 0.5 mm and a distance of 10 mm between each other. The first DSSSD layer is placed 50 mm away from the γ-ray source and at a distance of 85 mm from the front surface of the absorber

component. The latter is a scintillation detector, more specifically a monolithic $LaBr_3$:Ce^{3+} crystal, with a volume of 50.8 × 50.8 × 30 mm^3, chosen for its excellent time and energy resolution. Some preliminary studies have also been done in order to study $CeBr_3$ as a future alternative to the currently used $LaBr_3$:Ce^{3+} scintillator, providing a cheaper solution with comparable time and energy resolution. Fig. 3.1 illustrates the configuration of the LMU Compton camera prototype, designed for small animal imaging, indicating as well some geometrical specifications as chosen through simulations performed in a previous PhD thesis [8].

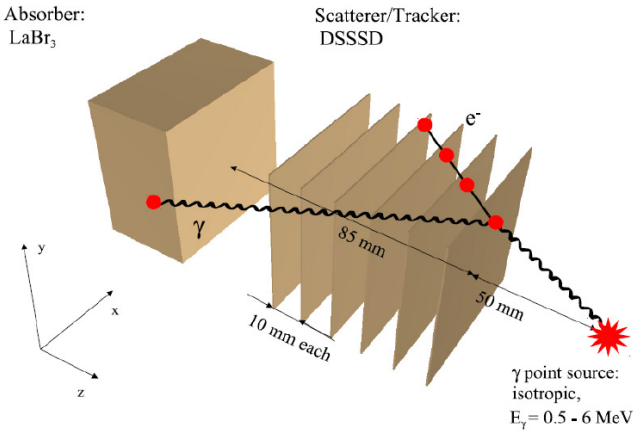

Figure 3.1: LMU Compton camera geometrical arrangement adjusted as a compromise between mechanical constraints and the camera performance envisaged for small animal irradiation purposes [8].

The Compton camera setup, namely the scatterer and absorber detectors, as well as the signal processing and mechanical components will be described in the following subsections. However, the main focus of this chapter will lie on the absorber detector, since this thesis is primarily dedicated to study its performance.

3.1.1 Double-sided-silicon-strip scatter detectors

The scatter component of the LMU Compton camera prototype consists of a stack of six DSSSD layers as seen in Fig. 3.2. Each DSSSD detector has an active area of 50 × 50 mm^2 and a thickness of 500 μm. The detector has 256 strips in total, 128 strips on the front side (p-side) and another 128 on the back side (n-side), each strip with a 390 μm pitch size. Each layer can be read out via 64-channel high-density multi-pin connectors at each of the four sides.

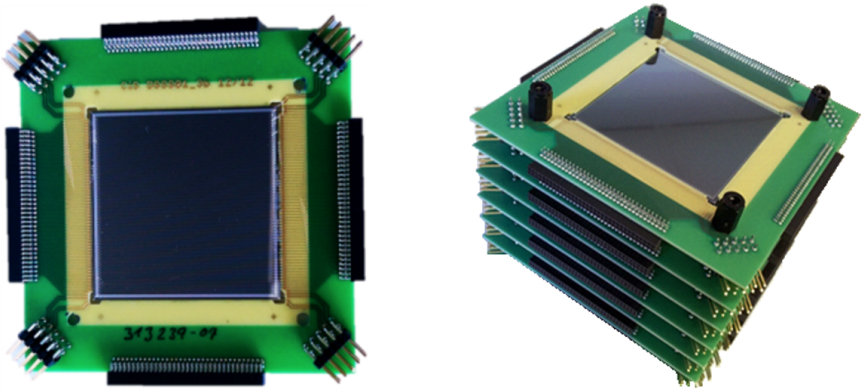

Figure 3.2: Single DSSSD (left) and stacked array of six DSSSD detectors (right). For details see text.

In the "standard" readout configuration, which was used for the purpose of the measurements described in this thesis, the strip signals are processed by front-end (FE) electronic boards that contain 4 charge integrating GASSIPLEX Application-Specified Integrated Circuit (ASIC) chips [48], having a total of 24 boards coupled to the six DSSSD layers (4 per layer). To read out the 24 FE boards 4 bus cards are needed.

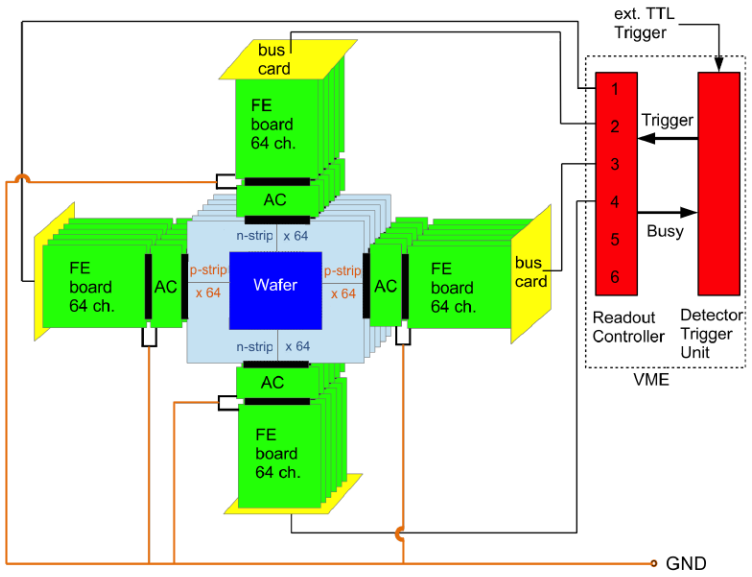

Figure 3.3: Scheme illustrating the geometrical arrangement of the six DSSSD layers and their readout electronics based on the GASSIPLEX ASIC chip. Each DSSSD layer has 256 signal channels that are read out by four FE boards. On each side of the silicon detectors there are 6 FE boards, connected via a bus card. This card collects and transfers the data to a VME-based readout controller. Since the trigger is provided by the absorber, a VME-based trigger unit is also needed [5].

The scatterer data is then merged and synchronized with the absorber data into a common list-mode data stream. The trigger in this configuration has to be provided by the absorber detector, since the GASSIPLEX Application Specific Integrated Circuit (ASIC) chips possess no trigger capability. Finally, the data is transferred through the VME-based readout controller to the acquisition PC using a PowerPC (PPC) RIO-3 frontend CPU via an Ethernet cable.

3.1.2 Absorber detectors

The purpose behind this subsection is to characterize the absorber component of the LMU Compton camera. Although the main topic of this thesis is to study the performance of a $LaBr_3:Ce^{3+}$ crystal currently used as the absorber detector, some preliminary studies with a $CeBr_3$ crystal have also been performed. Therefore, in order to compare some performance observables between the two absorbers, a characterization of this crystal will also be given.

3.1.2.1 $LaBr_3:Ce^{3+}$ crystal

The current absorber component of the LMU Compton camera is formed by a $50.8 \times 50.8 \times 30\ mm^3$ monolithic cerium-doped lanthanum tribromide ($LaBr_3:Ce^{3+}$) scintillation crystal, commercialized by Saint-Gobain Ceramics & Plastics Inc. under the name BrilLanCe^{TM}380 [49]. A reflective coating was chosen for the crystal, in order to support the process of light collection, after a systematic study was carried out for both absorptive and reflective scenarios [50]. This crystal was chosen due to its favourable characteristics, some of them presented in Table 2.1, mainly its high light yield (63000 ph/MeV), excellent energy resolution at low photon energies (3% at 662 keV) and fast decay time (16 ns). Although the material presents a rather low effective atomic number (Z_{eff}=47) and density (ρ=5.29 g/cm^3) when compared to other inorganic scintillator materials, the photon power energy can be enhanced by increasing the crystal volume. Due to its characteristics the $LaBr_3:Ce^{3+}$ detector has an excellent time resolution, which allows the use of the Time-of-Flight (TOF) technique for neutron-γ discrimination, together with an excellent energy resolution allowing for a more accurate reconstruction of the prompt-γ origin. However, this material presents two main disadvantages: its internal radioactivity and hygroscopicity. Due to the latter, the crystal must be maintained in dry conditions in order to prevent its degradation due to air humidity and is therefore encapsulated in a light and air tight aluminum box. Although necessary, the aluminum layer surrounding

the material may reduce the detector's performance by absorption and scattering. The $LaBr_3$:Ce^{3+} internal radioactivity occurs due to the presence of the unstable ^{138}La isotope and to the radiochemical impurities of ^{227}Ac and its daughters. Whereas the ^{138}La activity dominates for energies below 1.6 MeV, the contamination due to ^{227}Ac and its daughters affects the γ spectrum for energies between 1.6 MeV and 3 MeV. Through radiochemical material purification it is possible to solve the ^{227}Ac contamination that occurs during the crystal production process [51], unfortunately a simple solution for ^{138}La removal has not yet been found. ^{138}La is the only natural occurring radioactive isotope of lanthanum, with an abundance of 0.0902% and a half-life of $1.06(4) \times 10^{11}$ years [52].

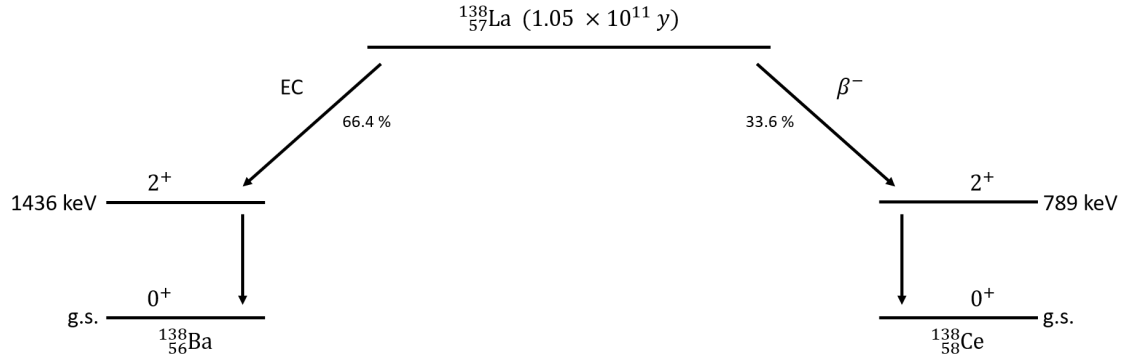

Figure 3.4: ^{138}La decay scheme.

As evident from its decay scheme, Fig. 3.4, ^{138}La decays with a 66.4% probability by electron capture (EC) into ^{138}Ba, emitting 1436 keV γ rays, and with 33.6% via β-decay into ^{138}Ce with the emission of 789 keV γ rays. The internal activity spectrum can be measured by shielding the detector against room background with lead. Fig. 3.5 shows such a spectrum acquired for 4 hours with a $50.8 \times 50.8 \times 30$ mm^3 lead shielded monolithic $LaBr_3$:Ce^{3+} crystal. At the beginning of the spectrum it is possible to see the β^- continuum at low energies, representing 33.6% of the ^{138}La decay, with an end point of 255 keV. Moreover, the 789 keV γ-ray from the $2^+ \rightarrow 0^+$ groundstate transition in ^{138}Ce is visible at higher energies. However, since it is in coincidence with the β continuum, its photopeak is broadened. The next prominent photopeak corresponds to the 1436 keV γ ray emitted in coincidence with the capture of X rays, originating when the Ba K (35.5 keV) and L (4.5 keV) levels are filled following K-electron or L-electron capture, respectively. Therefore, this photopeak is shifted either to 1440 keV or 1472 keV, when detected together with ^{138}Ba L or K rays, respectively. At the end of the spectrum, beyond this photopeak energy, the presence of low level alpha particles resulting from the ^{227}Ac contamination is revealed. Although undesirable, the $LaBr_3$:Ce^{3+} scintillator internal activity can be

turned into an advantage. For example, prominent structures such as the 1436 keV photopeak can be used for energy calibration purposes. Furthermore, the crystal's internal activity can be used to mimic a homogeneous and isotropic external irradiation of the crystal, helping to assess the spatial crystal homogeneity, as will be shown in Sect. 4.3.3.

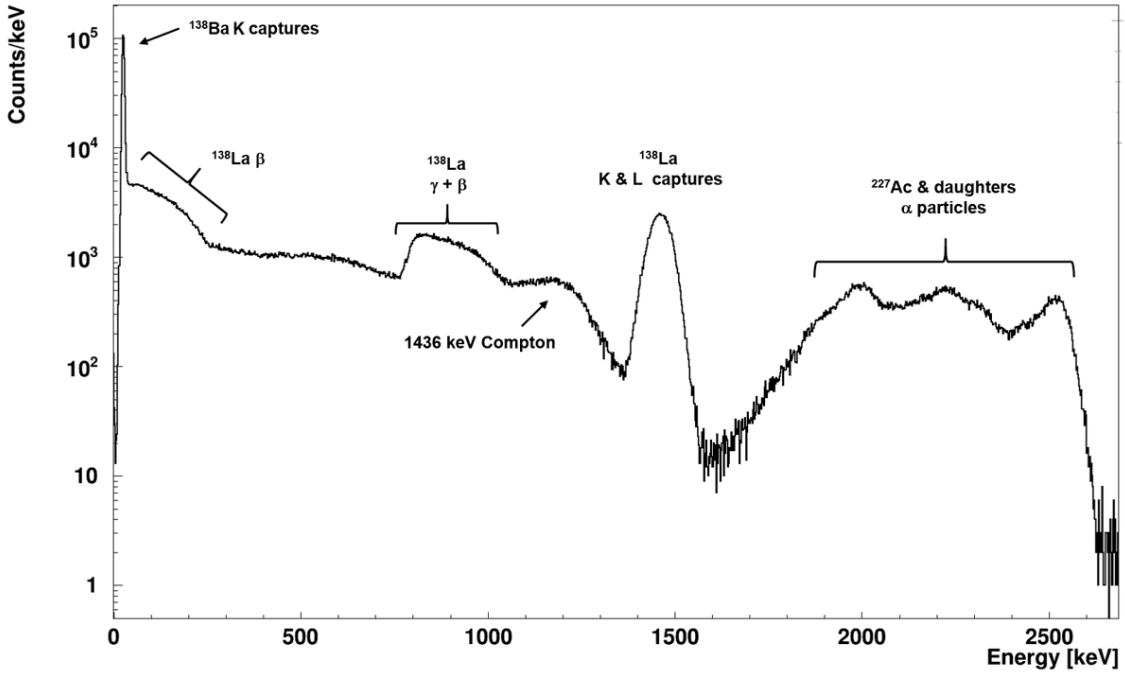

Figure 3.5: Internal radioactivity energy spectrum of a monolithic 50.8 × 50.8 × 30 mm^3 $LaBr_3$:Ce^{3+} scintillator acquired from a four hours measurement.

3.1.2.2 $CeBr_3$ crystal

Cerium bromide ($CeBr_3$), a recently developed crystal [53], has become a material of interest for high-resolution γ-ray spectroscopy. A crystal of this material, with identical dimensions of 51 × 51 × 30 mm^3 as the previously studied $LaBr_3$:Ce^{3+} crystal, has been investigated as a potential alternative for $LaBr_3$:Ce^{3+}, since it shares many of its favourable characteristics, namely the fast decay time (17 ns), high light yield (68000 ph/MeV) and excellent energy resolution (4% at 662 keV), as is evident from Table 2.1, at a considerably lower price. The scintillation light emitted by the $CeBr_3$ is in the same wavelength (380 nm) region as the one emitted from $LaBr_3$:Ce^{3+}, therefore it can be read out with the same photon sensors. Unfortunately the $CeBr_3$ crystal is also hygroscopic and was therefore purchased from Scionix [54] already encapsulated in an aluminum housing with one side covered only by a quartz window, allowing for the produced light to be guided out of the

crystal to the photosensor. Since neither cerium (Ce) or bromide (Br) elements possess any naturally occurring radioactive isotope, $CeBr_3$ only exhibits background originating from alpha decays of various actinides. This α contamination in the crystal is also due to ^{227}Ac and its daughters [55] giving rise to structures appearing between 1.6 and 3 MeV in the crystal spectrum, as can be seen in Fig. 3.6. The small intrinsic background rate is expected to translate into a count rate of about 270 counts in the previously mentioned energy range, given the crystal size and the acquisition time. However, a higher count rate is observable in Fig. 3.6 probably due to additional contributions of room background and to photons from radioactive decay of (via cosmic radioaction) activated lead shielding blocks at 2.6 MeV. When compared to $LaBr_3$:Ce^{3+}, the $CeBr_3$ gamma-ray energy background spectrum shows a lower internal radioactivity (Fig. 3.6) by nearly an order of magnitude in the 0-3 MeV energy range [56], therefore the internal activity of this crystal can be considered negligible. We can conclude that the $CeBr_3$ crystal is a good alternative candidate for the current Compton camera absorber component, since it shows a similar performance without a high internal activity and is available at considerably lower cost.

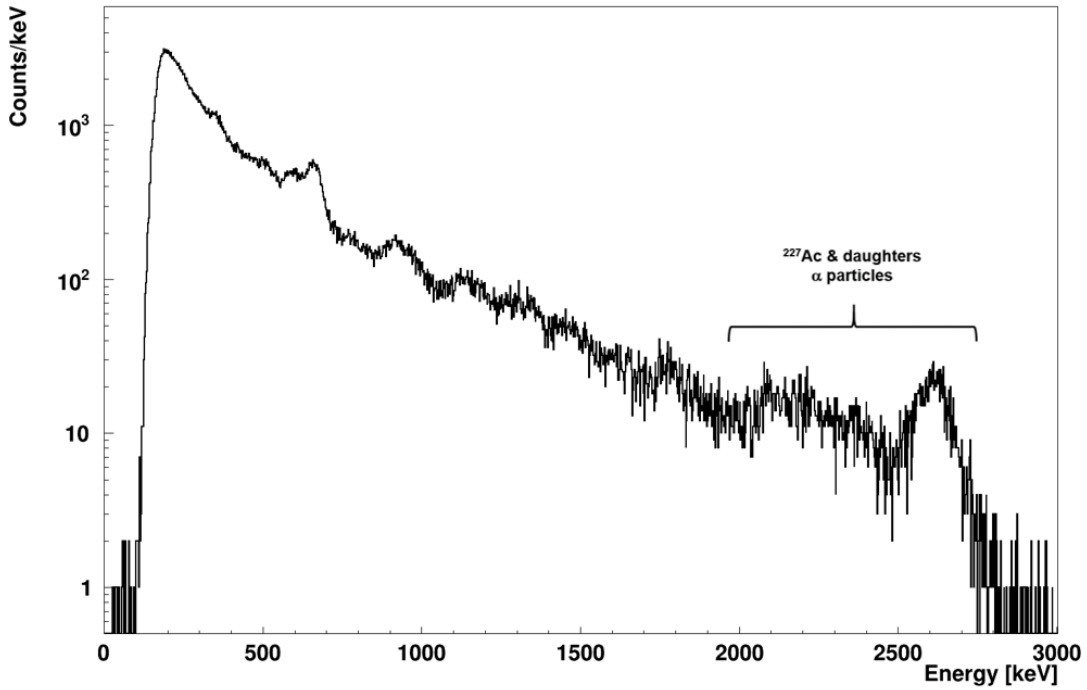

Figure 3.6: $CeBr_3$ crystal background γ-ray spectrum acquired from a one hour measurement.

3.1.2.3 Electronic signal processing and data acquisition

As explained in Sec. 2.2.1, after irradiating the scintillator material, the excited atoms will de-excite to lower-energy states, thus emitting scintillation light. This light will be detected by a pixelated PMT that converts it into photoelectrons producing a measurable electronic signal, which will be processed through the electronic chain and analyzed by the Data Acquisition System (DAQ). The monolithic $LaBr_3:Ce^{3+}$ scintillator crystal under study is read out by an 8 x 8 multi-anode position sensitive PMT (H8500 fabricated by Hamamatsu [43]), with a large effective area of 49 × 49 mm^2 and an anode size of 5.8 × 5.8 mm^2. This 64 pixel PMT can be operated with a supply voltage between (-)700 V and (-)1100 V. Fig. 3.7 shows a photograph of the detector coupled in our laboratories using an optical coupling grease (BC-630 Silicone Grease manufactured by Saint-Gobain Crystals [57]) for light guidance.

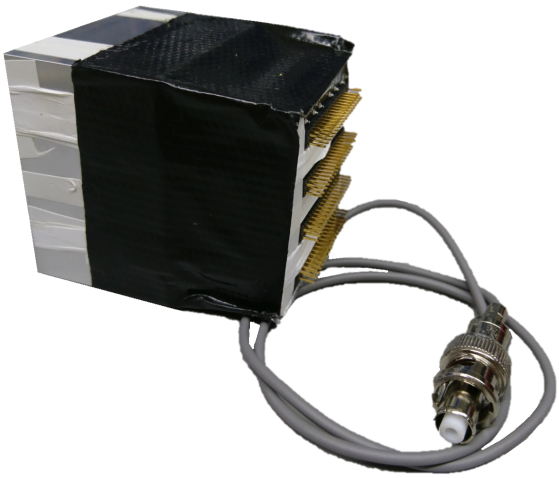

Figure 3.7: Photograph of the $LaBr_3:Ce^{3+}$ crystal coupled to an 8 × 8 multi-anode PMT (H8500 from Hamamatsu) [43].

The block diagram of the $LaBr_3:Ce^{3+}$ scintillator readout electronics is shown in Fig. 3.8. The signals of the 64 PMT segments are sent to specifically designed adapter boards via four 16-pin high-density coaxial ribbon cables in order to transfer the signals to 10 ns LEMO cables. The 64 signals are then transferred by the LEMO cables into four Constant Fraction Discriminator modules (MCFD-16 from Mesytec [58]), each handling 16 input channels. For each of the 64 input signals, the Constant Fraction Discriminator modules (MCFDs) amplify the energy signal and create an amplitude-independent logical signal. Moreover, for each channel a logic output signal is generated that acts as an individual gate in the subsequent digitizer module. The amplitude signals, as well as the logical gate signals, are then

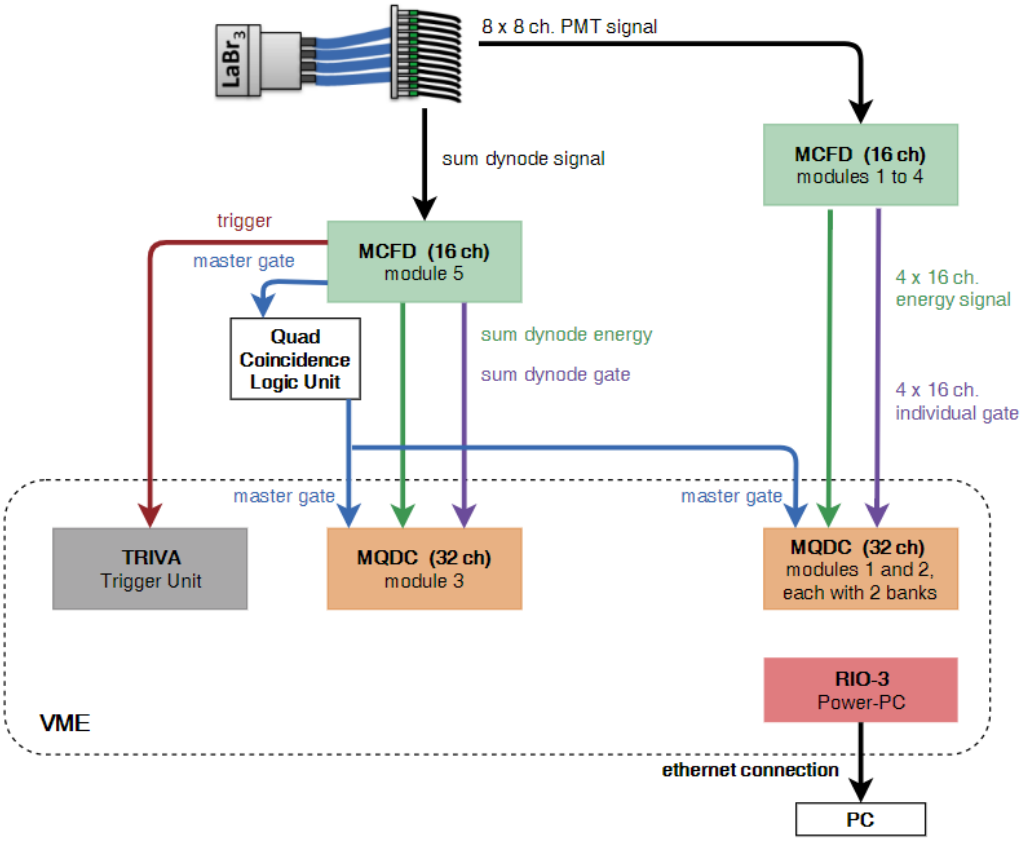

Figure 3.8: Block diagram of the $LaBr_3$:Ce^{3+} signal readout and data acquisition electronics.

fed into Charge-to-Digital Converter modules (MQDC-32 from Mesytec [59]) that can process 32 channels each, divided in two input banks. Each input bank of the Charge-to-Digital Converter module (MQDC) is responsible for all 16 signals of one MCFD. The MQDC modules integrate the incoming signal over the duration of the individual gate, providing energy information of each individual channel, which is only possible if the individual gates precede the amplitude signal. Therefore, both the signals and the gates need to be delayed via 13 m and 8 m flat ribbon cables, respectively [8]. In addition to the signals from the 64 individual segments, a sum signal is directly extracted from the sum-dynode output of the PMT and fed to a fifth MCFD module, via a 10 ns LEMO cable. The common logic output signal from this module is used to generate the trigger signal for the DAQ system, produced when the sum dynode signal is exceeding its energy threshold. This signal is sent to a TRIVA 5 VME trigger unit (built by GSI [60]), as well as a master gate, needed for the operation of each MQDC module. This gate is needed in order to ensure a synchronized data acquisition for all the channels. The output signal of the sum-dynode MCFD module is connected to a Quad Coincidence Logic Unit

operating in OR mode that splits the master gate into identical copies and sends it to each MQDC module, opening a time window during which a signal can be acquired. The acquired data is sent to the control PC via a PowerPC (PPC) RIO-3 frontend CPU (operated with the real-time operational system LynxOS [61]) and processed by MARABOU [62], an MBS and ROOT [63] based acquisition system.

In the following Table 3.1 the most relevant settings, for the work presented in this thesis, used for the MCFD and MQDC modules are summarized. The configuration parameters for both single channels and sum dynode are present. While the configuration parameters of the MCFD modules are set using its front panel, the ones of the MQDC modules are changed through chips on the VME-based board. The polarity was set according to the output signal, positive for the sum dynode and negative for the single channels. The gain, or amplification factor, in the MCFD is chosen depending on the energy range of the γ ray that interacts with the scintillation detector, adjusted to avoid signal saturation. Since the PMT pixels have a large effective area, there is no need for a high amplification factor, therefore a gain of 3 was chosen for the single channels, while for the sum dynode a gain of 1 was sufficient. The dead time was adjusted to be 300 ns, thus not unnecessarily longer than the recovery time of the MQDC estimated to be 250 ns. The gain jumpers of the MQDC modules can be exchanged in order to define the dynamic range of interest. A default value of 500 pC was kept for all the single channels, whereas the jumper for the sum dynode signal was chosen as 1.5 nC.

Signal	**MCFD parameters**			**MQDC parameters**
	polarity	gain	dead time (ns)	gain jumper (nC)
single channels	negative	3	300	0.5
sum dynode	positive	1	300	1.5

Table 3.1: Configuration parameters for the MCFD and MQDC modules used for processing the 64 PMT signals for the single channels and the sum dynode signal.

The width of the master gate, which corresponds to the OR output of the MCFD module processing the sum dynode signal, was set to 160 ns. It should be noted that increasing the master gate too much can lead to a decreasing of the recorded events due to the increase of dead time. Moreover, more noise or random background events will be integrated. The minimum allowed time between the start of the master gate and the start of the individual gate is 2 ns, and the amplified analogue signal should

not start earlier than 6 ns after the falling edge of the individual gate. Due to the importance of fulfilling these requirements, in order not to lose events and to ensure a correct integration of the signal, they were both set to 10 ns. The analogue energy signal, individual and master gate, and respective timing relation, are sketched in Fig. 3.9.

The same readout system is used for the recently acquired $CeBr_3$ scintillator crystal, normally coupled to an 8 x 8 multi-anode position-sensitive PMT (H12700 fabricated by Hamamatsu [64]). The main difference between the PMT used for the $LaBr_3$:Ce^{3+} (H8500) and the more modern one used here (H12700) are the gain, which is higher for the H8500 (7×10^5), and the quantum efficiency, which is higher for the H12700 (30%). The specifications of the different mentioned PMTs can be seen in Appendix A.

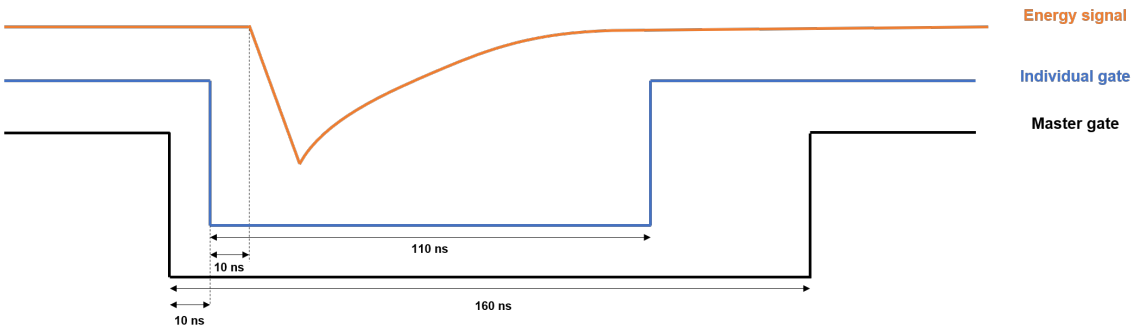

Figure 3.9: Timing relation used for the input signals of the MQDC signals for the integration of the input energy signal of individual PMT segments.

3.1.3 Mechanical setup

In order to give an overview of the camera setup, its mechanical arragement will be explained in this section. Since the focus of this thesis is to study the absorber component and not the performance of the camera as a whole, only a brief explanation will be given. A more detailed description can be found in [5]. Photographs of the Compton camera setup during a beam time at the Maier-Leibnitz-Laboratorium (MLL) in Garching, namely its a) front view, b) back view and c) the closed camera container box can be seen in Fig. 3.10. It should be noted that the scatter component readout system (2) detailed in the figure has been recently acquired from the company Mesytec, replacing the GASSIPLEX-based readout system described earlier. This new DAQ system is currently being commissioned with our setup as part of Silvia Liprandi's ongoing PhD thesis work [65]. Further details will be given in this thesis' outlook. A mechanical support frame had to be designed and built in

order to position the Compton camera components, namely the DSSSD scatter array (1) and the $LaBr_3$:Ce^{3+} crystal (5). A cubic frame ($61.5 \times 55.8 \times 55.8$ cm^3) made of aluminum profile bars with additional support bars was built in our workshop. The DSSSD array forms a block and, together with the processing boards attached to the four sides, was attached to the front frame of the support cube. This arrangement can be seen in Fig. 3.10 a). The scintillator crystal and its adapter boards were mounted behind the scatter array, visible as item (5) in Fig. 3.10 b). The distances between the scatterer layers and the absorber were previously shown in Fig. 3.1. After the camera components were fixed, the frame was covered from all sides by 3 mm thick aluminum plates. An entrance window (7), made of a $\sim$30 μm thick aluminum foil, was inserted in the front plate in the center of the DSSSD detector in order to minimize the scattering probability of the photons prior of entering the Faraday cage. This way a light-tight box is formed, in order to minimize light exposure, and to form a Faraday cage against external electromagnetic perturbations. However, placing the camera components inside a tight aluminum box leads to a temperature increase, which could affect the detector's performance or in a more extreme case damage the electronics. Therefore, two temperature sensors were placed inside the camera ((3) and (4)) and a cooling system (6) was installed at one side of the camera cage, guaranteeing that it operates at a constant temperature, typically between 17 and 20^{o}C. The Compton camera is placed on top of a height-adjustable support stand, allowing to adjust the camera position relative to the target. For example in Fig. 3.10 the stand's height was adjusted such that the beamline (8) would be on the level of the center of the DSSSD detector's active area.

Figure 3.10: Photographs of the Compton camera mounted at a beamline of the Maier-Leibnitz-Laboratorium (MLL) in Garching during a beam time at the local Tandem accelerator. In a) the front view of the camera is presented, where the DSSSD detector (1) and its readout system (2) are visible, while in b) there is shown the back view from where the absorber component (5) and temperature sensors ((3) and (4)) are visible. In c) the closed Compton camera can be seen with the cooling system on the right side (6) and with the entrance window (7) as well as the beam line (8) with exit window flange and cylindrical water target in the front.

4

Characterization of the absorber detector

As previously mentioned in Sect. 1.3, when the LMU Compton camera prototype was first commissioned, a readout of the $LaBr_3$:Ce^{3+} crystal scintillator through a 16 $\times$ 16 multi-anode position sensitive PMT (H9500 from Hamamatsu [66]) featuring 256 segments, each with an area of 3 $\times$ 3 mm^2 was acquired. However, previous Master theses studies [1, 2] have shown, through a combination of signal channels via software offline analysis, that a similar or even improved spatial resolution of the absorber detector can be achieved when using a reduced number of readout channels. Therefore, in order to reduce the complexity of the readout electronics and to simplify the whole system, a new scintillator crystal was acquired and coupled to a PMT with only 64 segments, as described in Sect. 3.1.2.3. In contrast to the older $LaBr_3$:Ce^{3+} scintillator, which was already coupled and encapsulated together with its readout sensor by the manufacturer inside a light and air tight aluminum housing, the crystal studied in this thesis was self-coupled in our laboratory. A description of the coupling procedure can be seen in Appendix C. In this chapter a thorough characterization of this new detector will be given. Firstly, the detector time resolution will be presented. Secondly, the position-dependent energy resolution was investigated by scanning the detector's front surface with a ^{137}Cs collimated source and a step size of 6.08 mm. Moreover, the relative energy resolution was evaluated as a function of the high voltage applied to the PMT. The time and position-dependent energy resolution were also determined for the recently acquired $CeBr_3$ crystal in order to compare the performance of both crystals. Each detector requires its own reference dataset, resulting in the need to acquire a reference library for the new $LaBr_3$:Ce^{3+} crystal. This way the photon interaction position determination is enabled as well as the quantification of the spatial resolution. The algorithms used in our group to reconstruct the photon interaction position within a monolithic scintillator are going to be explained, followed by a description of the experimental setup

used for the reference library acquisition. Correction factors were applied to the raw data to ensure that the response of all PMT pixels was consistent and therefore those transformations will be described. The acquired reference libraries will then be presented. Towards the end of the chapter, the performed systematic study of the spatial resolution of the $LaBr_3$:Ce^{3+} scintillation detector, as a function of different parameters, will be presented and discussed.

4.1 Time resolution

The time resolution of the detector under study was determined in the framework of Tim Binder's ongoing PhD thesis work using a coincidence method. The time resolution of a reference detector was determined through the measurement of the Coincidence Resolving Time (CRT) between two simultaneously emitted γ rays from a ^{60}Co source. This measurement was done using two identical reference plastic detectors (BC-418 manufactured by Saint-Gobain Crystals [67]) coupled to fast PMTs (XP2020Q from HZC Photonics [68]). Both signals were read out by the same electronics and then the time resolution of one of them, $\Delta T_{reference}$, was calculated by

$$\Delta T_{reference} = \sqrt{\frac{(\Delta T_{total-plastic})^2}{2}} \tag{4.1}$$

where $\Delta T_{total-plastic}$ is the total time resolution obtained from the coincidence time peak obtained between two identical plastic scintillators. Afterwards, while keeping the previous readout electronics parameters, one of the reference detectors was replaced by the $LaBr_3$:Ce^{3+} scintillation crystal coupled to the H8500 PMT. Using the time resolution $\Delta T_{reference}$ of the reference detector (281(2) ps (FWHM)) and the combined time resolution ΔT_{total} (410(2) ps (FWHM)) of the plastic and the crystal scintillator, the time resolution of the crystal scintillator can be determined:

$$\Delta T_{LaBr_3:Ce^{3+}} = \sqrt{(\Delta T_{total})^2 - (\Delta T_{reference})^2} \tag{4.2}$$

The measured CRT, equivalent to the combined time resolution, was ΔT_{total} = 387(2) ps (FWHM). Using the previously determined time resolution of the plastic detector and Eq. (4.2), it was determined that the time resolution for this scintillation crystal is 266(3) ps (FWHM). This procedure was repeated for the other two crystal scintillators currently under study in our group, namely a $CeBr_3$ crys-

tal coupled to an 8 × 8 multi-anode position sensitive PMT (H12700A-10) and a $LaBr_3$:Ce^{3+} detector read out by a 16 × 16 multi-anode position-sensitive PMT (H9500). The coincidence time peaks of the photons simultaneously emitted by the source and measured by the setup described above can be seen, for all the crystals, in Fig. 4.1.

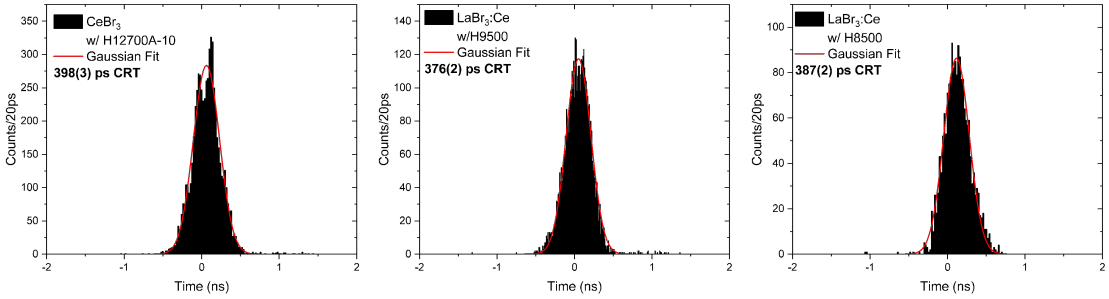

(a) (b) (c)

Figure 4.1: Coincidence time peak of the photons simultaneously emitted by a ^{60}Co source measured by a plastic scintillator and the three crystal scintillators currently under study: a) a $CeBr_3$ scintillator coupled to an 8 × 8 multi-anode PMT (H12700), b) a $LaBr_3$:Ce^{+3} crystal coupled to a 16 × 16 multi-anode PMT (H9500) and c) a $LaBr_3$:Ce^{+3} scintillator crystal coupled to an 8 × 8 multi-anode PMT (H8500). The red curves show a Gaussian fit whose FWHM represents the coincidence time measured for each scintillator pair.

For the $CeBr_3$ scintillator crystal a time resolution of 281(3) ps (FWHM) was determined, whereas for the $LaBr_3$:Ce^{3+} detector with a 256-channel readout the time resolution was founded to be 250(2) ps (FWHM). The contribution of the electronics to the obtained values is the same in all cases since the identical signal processing chain was used in the three measurements. Therefore the different results only depend on the crystals and different PMTs, making the time resolution comparable. Most notably, the $CeBr_3$ detector exhibits only a slightly worse time resolution compared to the two cases of $LaBr_3$:Ce^{3+} crystals studied with different photosensors.

4.2 Relative Energy resolution

4.2.1 Position dependence

The relative energy resolution $\frac{\triangle E}{E}$ of the $LaBr_3$:Ce^{+3} scintillator, as defined by Eq. (2.8), coupled to a 64-fold segmented multi-anode PMT (H8500), was evaluated

under different conditions. The energy spectrum was derived from the sum dynode signal and processed by a MCFD module (MCFD-16 from Mesytec [58]) and digitalized by a MQDC (MQDC-32 from Mesytec [59]).

Firstly, a 2D energy resolution map, presented in Fig. 4.2 was acquired at 662 keV by scanning the $LaBr_3$:Ce^{+3} scintillator's front surface with a 1 mm collimated ^{137}Cs source in a step size of 6.08 mm, in order to irradiate in the center of each PMT segment, using the setup described later in Sect. 4.3.2.

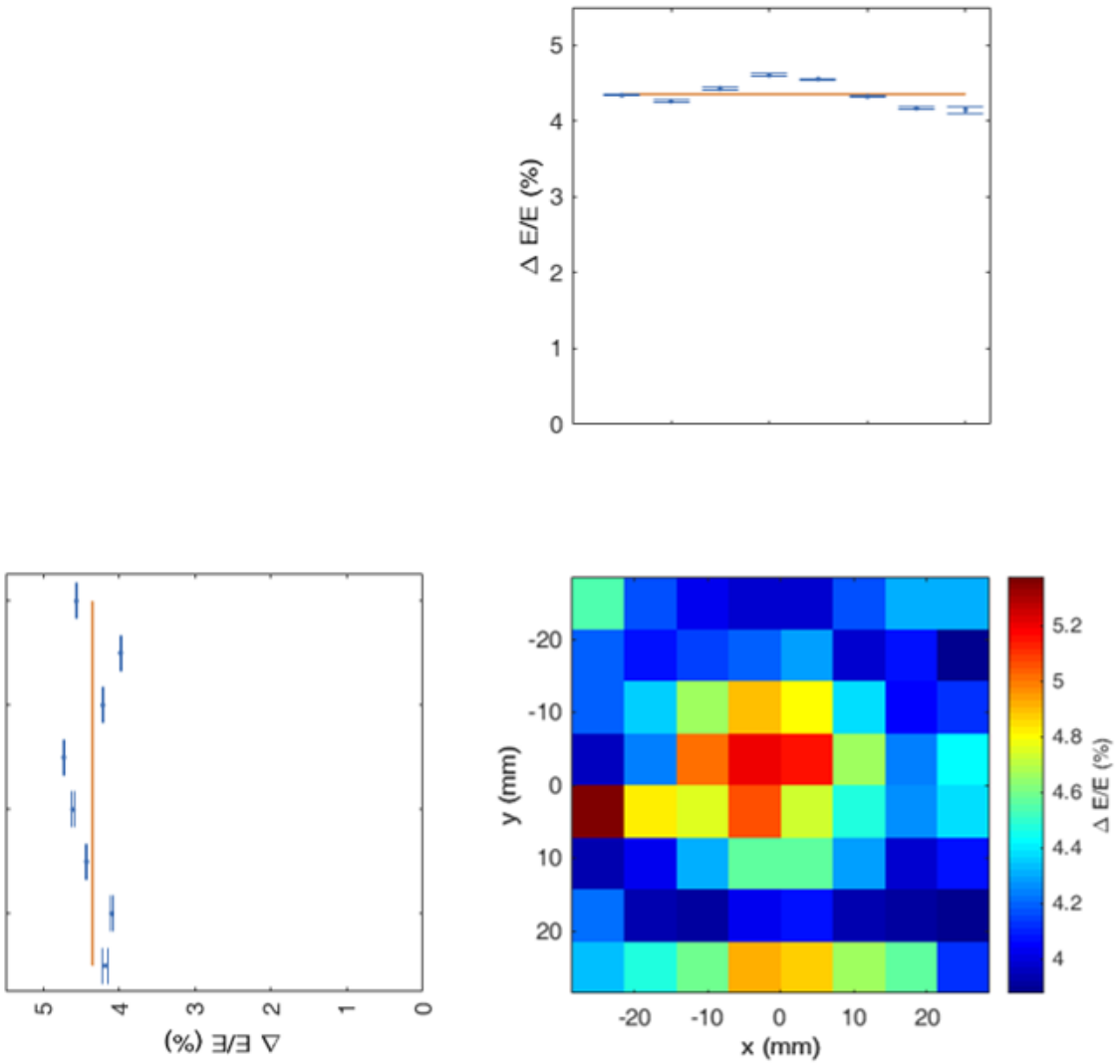

Figure 4.2: 2D energy resolution map acquired by scanning the $LaBr_3$:Ce^{+3} scintillator crystal (read out by a 64-fold segmented H8500 PMT) with a 1 mm collimated ^{137}Cs source with a step size of 6.08 mm in x and y directions, with both x and y projections. The horizontal orange lines denote the mean value obtained for the relative energy resolution of the x and y projections.

Given that the crystal is monolithic, we in principle expect to observe a position independent energy resolution, as observed by [5] for the first acquired absorber. However, a slight deterioration of the energy resolution can be expected at the crystal edges and corners, since in these irradiation positions the emitted scintillation light could be partially absorbed or scattered by the crystal surface finish or coating. Contrary to expectations, as is evident from the x and y projections in Fig. 4.2, obtained by integrating over the complementary dimension, the energy resolution reaches minimum values between 4.1%-4.5% at the detector edges, while the central region exhibits a slightly larger value of about 4.6%-4.8%.

In order to understand if this behaviour observed for the $LaBr_3:Ce^{+3}$ scintillator crystal coupled to the H8500 PMT (in the following called System 1) can be traced to the crystal itself or to the PMT, two additional studies were carried out with different systems. In order to test a potential crystal dependence, a new $LaBr_3:Ce^{+3}$ scintillator crystal (crystal II) was coupled in our laboratory to the same PMT (H8500) (System 2), while for testing the PMT influence, the scintillator crystal used in System 1 (in the following called crystal I) was coupled to a different PMT, an 8 $\times$ 8 multi-anode PMT (H12700) (System 3). Energy resolution maps were acquired also for both additional systems using the same method as described before. A similar position dependent energy resolution is observed for System 2 and 3, whose energy 2D resolution maps are presented in Fig. 4.3 and Fig. 4.4, respectively.

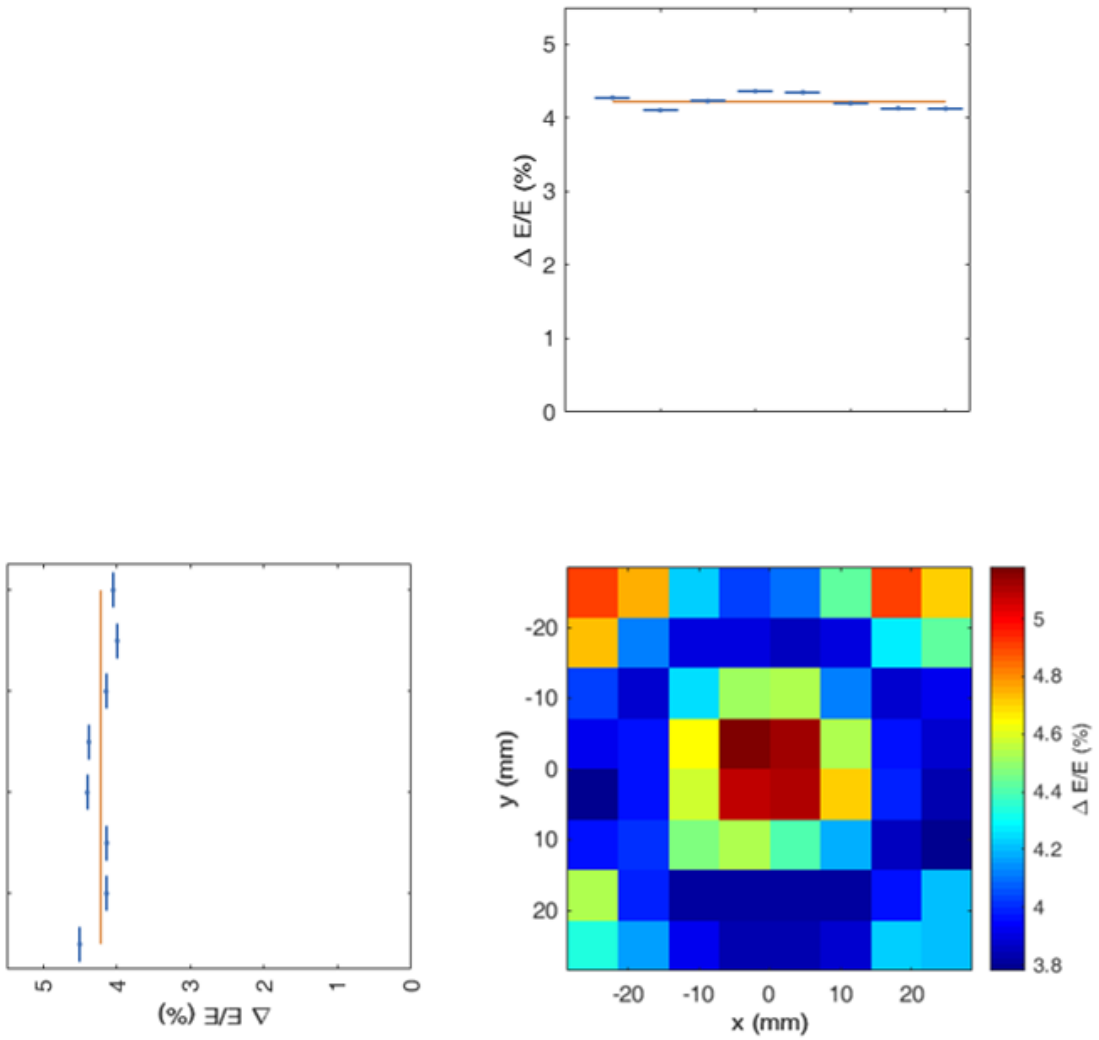

Figure 4.3: 2D energy resolution map acquired by scanning a new $LaBr_3$:Ce^{+3} scintillator crystal (crystal II) coupled to the H8500 PMT (System 2), with a step size of 6.08 mm in both x and y directions, using a 1 mm collimated ^{137}Cs source. The horizontal orange lines denote the mean value obtained for the relative energy resolution of the x and y projections.

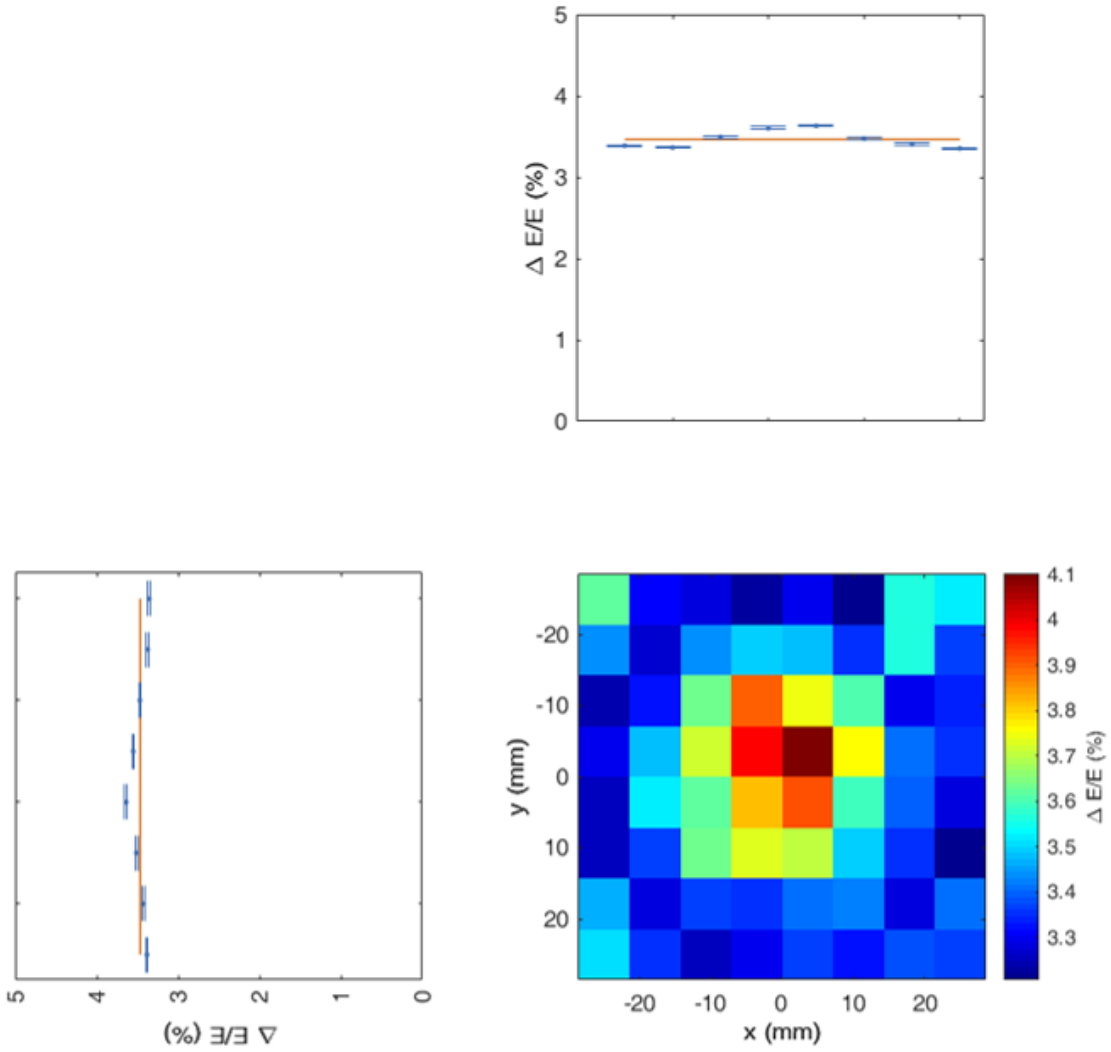

Figure 4.4: 2D energy resolution map acquired by scanning the $LaBr_3$:Ce^{+3} scintillator crystal of System 1 this time coupled to the H12700 PMT (System 3). The scan was performed with a step size of 6.08 mm in x and y directions, using a 1 mm collimated ^{137}Cs source. The horizontal orange lines denote the mean value obtained for the relative energy resolution of the x and y projections.

The corresponding variances σ^2 for the x and y projections are listed in Table 4.1. The two crystals used in this study are monolithic, therefore their energy resolution should only vary slightly with the irradiation position thus low values of the variances are expected for the three systems. Indeed, although the previously shown 2D energy resolution maps exhibit some variation of the energy resolution with the irradiation position for all systems, the resulting variance values ($\sim 0.01\% - 0.07\%$) amount to typically less than 1% of the values determined for the energy resolution ($\sim 3 - 5\%$) making them acceptable.

As can be inferred from Table 4.1, System 1 shows an average variance more

than twice as large than the one observed for the other systems. The average energy resolution varies only slightly between System 1 and 2, as would be expected since the same PMT is used, however, it significantly improves for System 3. The better performance of this system is more likely due to the different PMT, the H12700, which features a higher quantum efficiency compared to its predecessor version H8500. These findings do not lead to an explanation for the counter-intuitive slight position dependency energy resolution of System 1. However, it can be concluded that the observation for System 1 is consistently seen in all three systems, leading to the conclusion that this behaviour may not be traceable to a single component.

	System 1		**System 2**		**System 3**	
	$LaBr_3$:Ce^{3+} I + H8500		**$LaBr_3$:Ce^{3+} II + H8500**		**$LaBr_3$:Ce^{3+} I + H12700**	
	x	**y**	**x**	**y**	**x**	**y**
σ^2 (%)	0.03	0.07	0.01	0.03	0.01	0.01
$\overline{\frac{\triangle E}{E}}$ (%)	4.3(1)		4.1(1)		3.4(1)	

Table 4.1: Variance σ^2 of the x and y projections of the position-dependent relative energy resolution and average energy resolution $\overline{\frac{\triangle E}{E}}$ at 662 keV for the three detector systems.

A 2D energy resolution map was also acquired for the $CeBr_3$ crystal coupled to the H8500 PMT (System 4) in order to compare the performance of this crystal with the $LaBr_3$:Ce^{3+}. The $CeBr_3$ scintillation crystal coupled to the H12700 PMT (System 5) energy resolution has been previously studied by Tim Binder during his Master Thesis [69], observing an average energy resolution of 3.5%, allowing for a comparison between the two readout systems. System 4's energy resolution map, displayed in Fig. 4.5, was acquired with the same method as described for the previous systems. Although a spatial dependence is also observed for this system, in contrast to the other presented systems the reduction of the energy resolution does not occur in the crystal center but in its corners. As mentioned before, this behaviour can be expected since in the crystal edges and corners the incident light may suffer scattering or absorption by the crystal surface finish and coating.

The resulting variances σ^2 of the x and y projections can be inferred at Table 4.2. The position-dependent trend of the current study is consistent with the findings obtained by Tim Binder for System 5 and follows the intuitive expectation. However, the observed average energy resolution of about 6.5% for System 4 is much larger than the one observed when using the H12700 PMT (System 5) as can be seen in

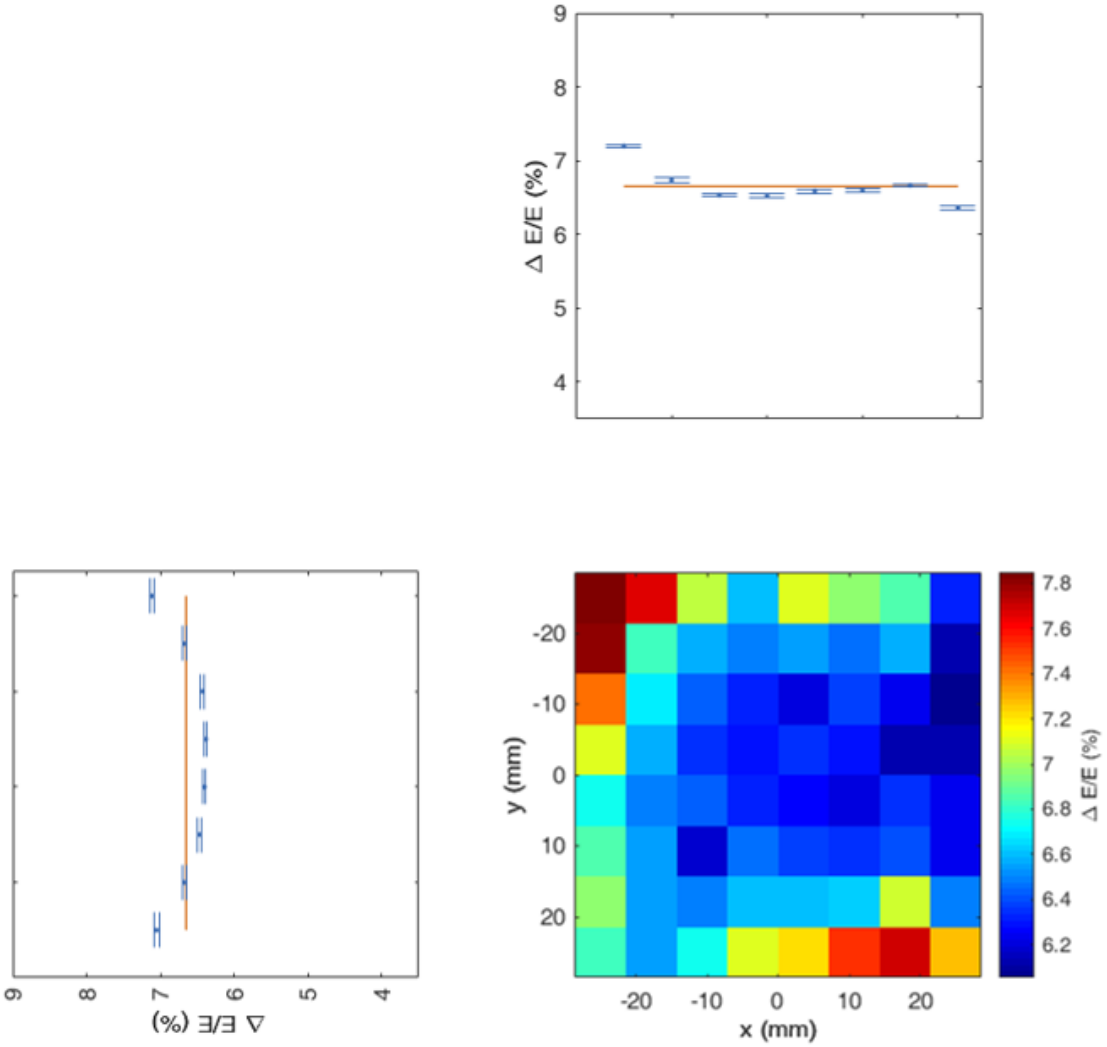

Figure 4.5: 2D energy resolution map acquired by scanning the $CeBr_3$ scintillator crystal coupled to the H8500 PMT (System 4) with a step size of 6.08 mm in both x and y directions, using a 1 mm collimated ^{137}Cs source. The horizontal orange lines denote the mean value obtained for the relative energy resolution of the x and y projections.

Table 4.2. This difference may arise from the improved performance of the H12700 PMT (mainly the higher quantum efficiency) compared to the H8500 PMT. This trend can already be seen when comparing System 1 and System 3 in Table 4.1, yet the much larger difference of $\frac{\triangle E}{E}$ in System 4 and 5 is surprising.

	System 4		System 5	
	$CeBr_3$ + H8500		$CeBr_3$ + H12700	
	x	y	x	y
σ^2 (%)	0.06	0.08	-	-
$\overline{\frac{\triangle E}{E}}$ (%)	6.5(1)		3.5(1)	

Table 4.2: Variance σ^2 of the x and y projections of the position-dependent relative energy resolution and average energy resolution $\overline{\frac{\triangle E}{E}}$ at 662 keV for the $CeBr_3$ detector system in study in this thesis (System 4) and the detector system previously studied by Tim Binder [69] (System 5).

In short, the obtained results for the four systems studied in the framework of this thesis lead to the following conclusions: the two studied $LaBr_3$:Ce^{3+} scintillation crystals show a slightly position dependent energy resolution, which deteriorates from the corners to the center independently of the coupled PMT. The overall relative energy resolution $\frac{\triangle E}{E}$ improves when using the more modern H12700 PMT compared to its predecessor model H8500. And finally the $CeBr_3$ scintillation crystal shows a position dependent energy resolution, which deteriorates in the corners and remains isotropic in the rest of the crystal, independently of the coupled PMT.

4.2.2 Energy resolution and PMT bias voltage

In a second measurement campaign, the relative energy resolution of the $LaBr_3$:Ce^{+3} (crystal I) was evaluated as a function of the applied high voltage to the PMT, in this case the model H8500, in order to determine an optimum operational voltage for the absorber detector. This study was performed for high voltages that ranged from -750 to -1100 V, with a step size of 50 V. According to the manufacturer, -1100 V is the maximum supply voltage that can be applied to the H8500 PMT, beyond this limit the performance of the PMT becomes unstable due to significant feedback effects. Isotropic point and collimated γ-ray calibration sources were used. While the isotropic point sources irradiate the detector homogeneously, the collimated calibration sources irradiate the detector in a specific area depending on the collimator's size. Although the resulting energy resolution should not differ when using point or collimated calibration sources, it was previously seen that the energy resolution for this system is (at least slightly) position dependent. Various isotropic point calibration sources, namely ^{60}Co, ^{137}Cs and ^{22}Na, were placed approximately 20 cm away from the detector in a central position. On the other hand, the collimated calibration sources ^{60}Co and ^{137}Cs were placed in two different positions:

first the collimator was positioned in the center of the detector's front surface and afterwards in front of its lower right corner, using the experimental setup described later in Sect. 4.3.2. In all cases the detector was irradiated for 15 minutes in order to ensure that sufficient statistics was acquired. The photon energies recorded range from 511 to 1332 keV. The different relative energy resolution values obtained as a function of the γ-ray energy, for each PMT voltage applied, are plotted in Fig. 4.6, Fig. 4.7 and Fig. 4.8.

The coloured curves parametrize the energy dependence of the relative energy resolution according to a two-parameter function expressed as

$$\frac{\triangle E}{E} = 100 \times \frac{\sqrt{A + B \times E}}{E} \tag{4.3}$$

where A and B are free parameters [70].

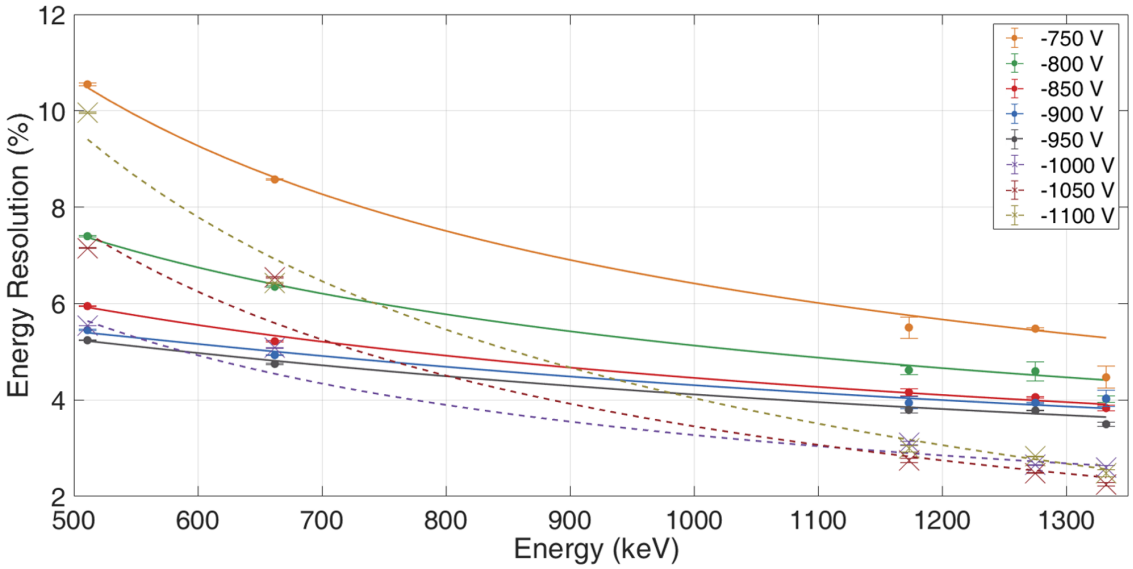

Figure 4.6: Relative energy resolution of the $LaBr_3$:Ce^{+3} (crystal I) as a function of the photon energy (keV) of isotropic γ-ray calibration sources placed 20 cm in front of the center of the detector surface for different PMT (H8500) supply voltages. The dashed lines represent PMT voltages $\geq$ 1000 V.

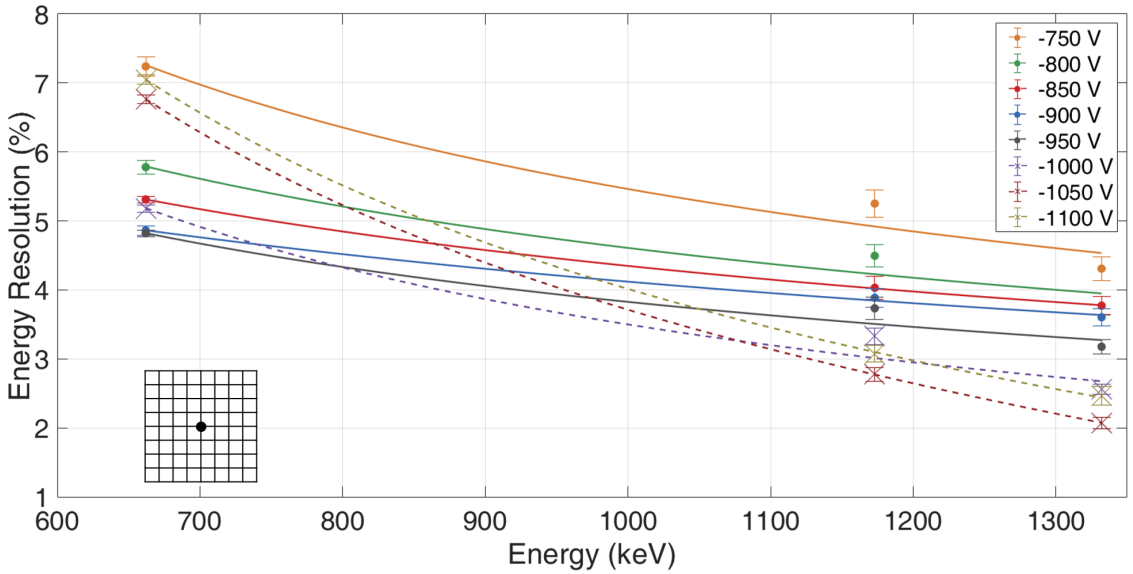

Figure 4.7: Relative energy resolution of the $LaBr_3$:Ce^{+3} (crystal I) as a function of the photon energy (keV) of collimated γ-ray calibration sources for different PMT (H8500) supply voltages. The dashed lines represent PMT voltages $\geq$ 1000 V. The insert illustrates the position of the collimated sources (blackdot) in front of the center of the detector.

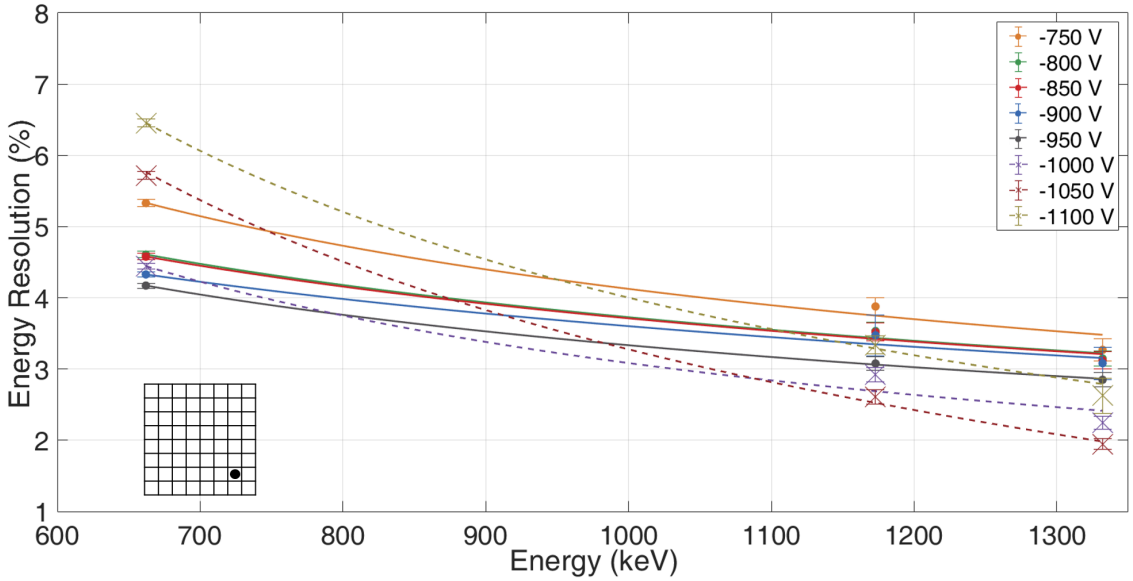

Figure 4.8: Relative energy resolution of the $LaBr_3$:Ce^{+3} (crystal I) as a function of the photon energy (keV) of collimated γ-ray calibration sources for different PMT (H8500) supply voltages. The dashed lines represent PMT voltages $\geq$ 1000 V. The insert illustrates the position of the collimated sources (blackdot) in front of the lower right corner of the detector.

From the analysis of the curves it can be concluded that in all cases the relative energy resolution improves with an increase of the photon energy for all PMT supply voltages applied. This trend is expected, since higher energy γ-rays have a higher depth of interaction in the scintillation crystal and therefore there is a higher probability of collecting all emitted scintillation light. Moreover, the amount of scintillation light produced by the detector increases with an increasing energy of incident γ rays, leading to an increase of the number of collected electrons in the PMT. Also the overall energy resolution improves when collimated sources are positioned in the detector's lower right corner (Fig. 4.8) compared to an irradiation of the crystal's center (Fig. 4.7), corroborating the results previously obtained and presented in Fig. 4.2 that consistently indicate an improved energy resolution of System 1 in the corner compared too the central region. For PMT bias voltages between -750 and - 950 V, the relative energy resolution improves with the increase of the absolute voltage. However, for values above -950 V, namely -1000, -1050 and -1100 V represented by the dashed lines in the graphs of Fig. 4.6 to Fig. 4.8, the relative energy resolution does not follow the same trend. For these high voltages the energy resolution starts to deteriorate for lower photon energies and to improve for higher ones as the high voltage is further increased. In order to better understand the correlation between the applied PMT voltage and the energy resolution, $\frac{\triangle E}{E}$ was plotted as a function of the PMT bias voltage for the different γ-ray energies, and different irradiation scenarios. Fig. 4.9 displays the bias dependent energy resolution for different isotropic point-source energies, while Fig. 4.10 and Fig. 4.11 show the same, but for irradiation scenarios of collimated sources in a central position in front of the center and the bottom right corner of the detector, respectively.

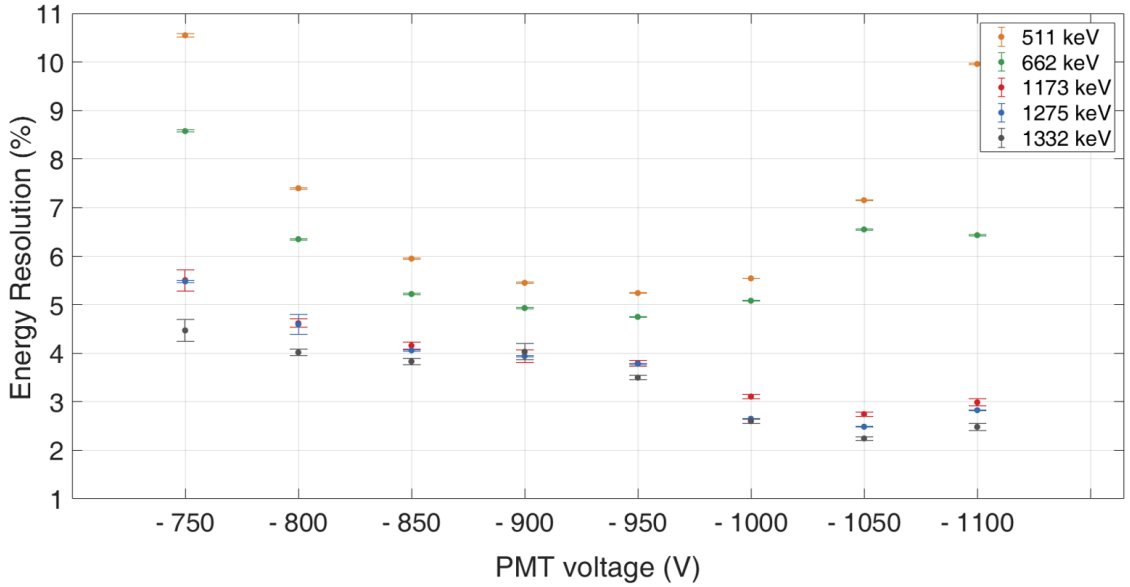

Figure 4.9: Relative energy resolution of the $LaBr_3$:Ce^{+3} (crystal I) as a function of the high voltage applied to the PMT (H8500) obtained with isotropic γ-ray point calibration sources

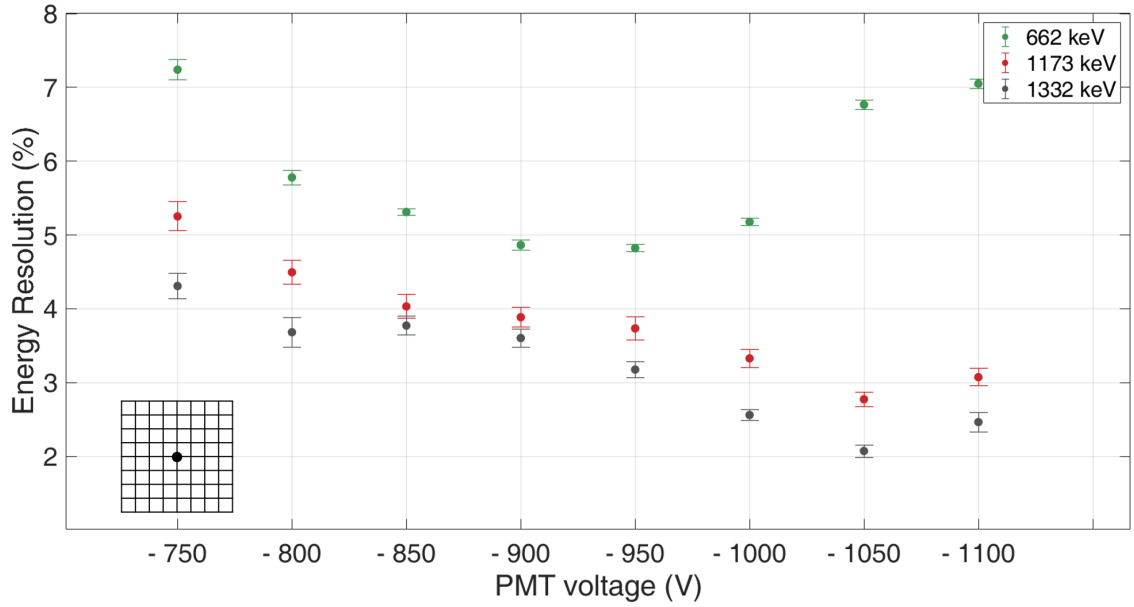

Figure 4.10: Relative energy resolution of the $LaBr_3$:Ce^{+3} (crystal I) as a function of the high voltage applied to the PMT (H8500) obtained with collimated γ-ray calibration sources. The insert illustrates the position of the collimated sources (blackdot) in front of the center of the detector.

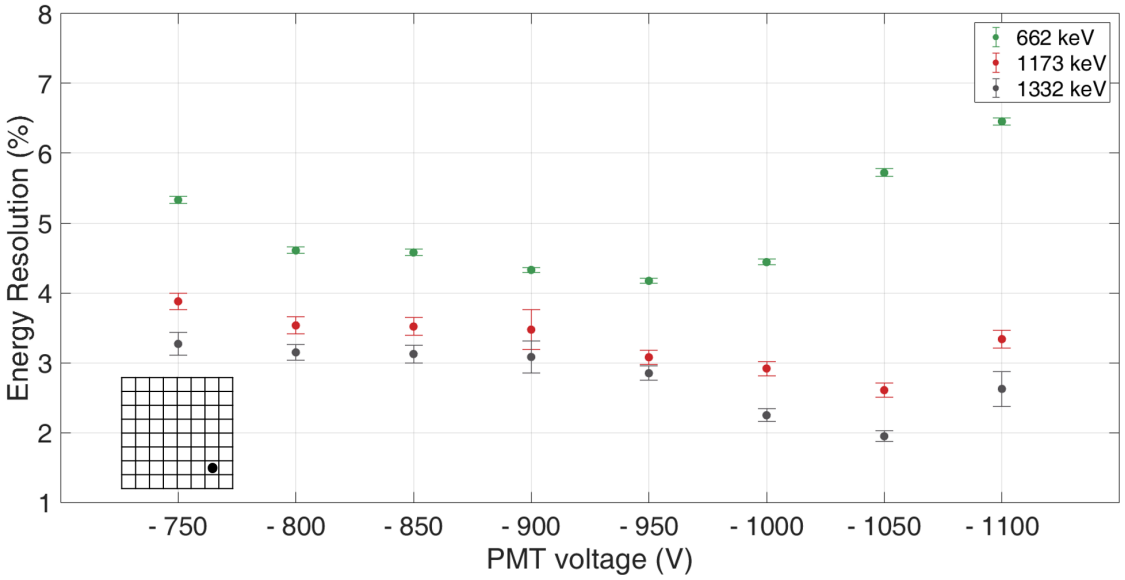

Figure 4.11: Relative energy resolution of the $LaBr_3:Ce^{+3}$ (crystal I) as a function of the high voltage applied to the PMT (H8500) obtained with collimated γ-ray calibration sources. The insert illustrates the position of the collimated sources (blackdot) in front of the lower right corner of the detector.

It is clear from these plots that for lower γ-ray energies (511 keV and 662 keV) the relative energy resolution reaches its minimum value in the range of -900 V to - 950 V and starts deteriorating as the absolute high voltage is further increased. However, for higher γ-ray energies (1173 keV, 1275 keV and 1332 keV) the minimum value is reached around -1000 V. The best energy resolution for this system (System 1), is therefore achieved by using bias voltages ranging from -900 to -950 V.

This systematic study was also carried out for System 2 and System 3, previously described in this section, using collimated γ-ray calibration sources placed in the region of the detectors' front surface that offer an improved energy resolution according to Fig. 4.3 and Fig. 4.4.

Fig. 4.12 and Fig. 4.13 show the energy resolution for System 2 as a function of the incoming photon energy for different PMT supply voltages and as a function of the applied high voltage for the different photon energies, respectively. These results match those observed for System 1, as can be expected, since both systems use the same H8500 PMT (coupled to different $LaBr_3:Ce^{3+}$ crystals of identical specifications).

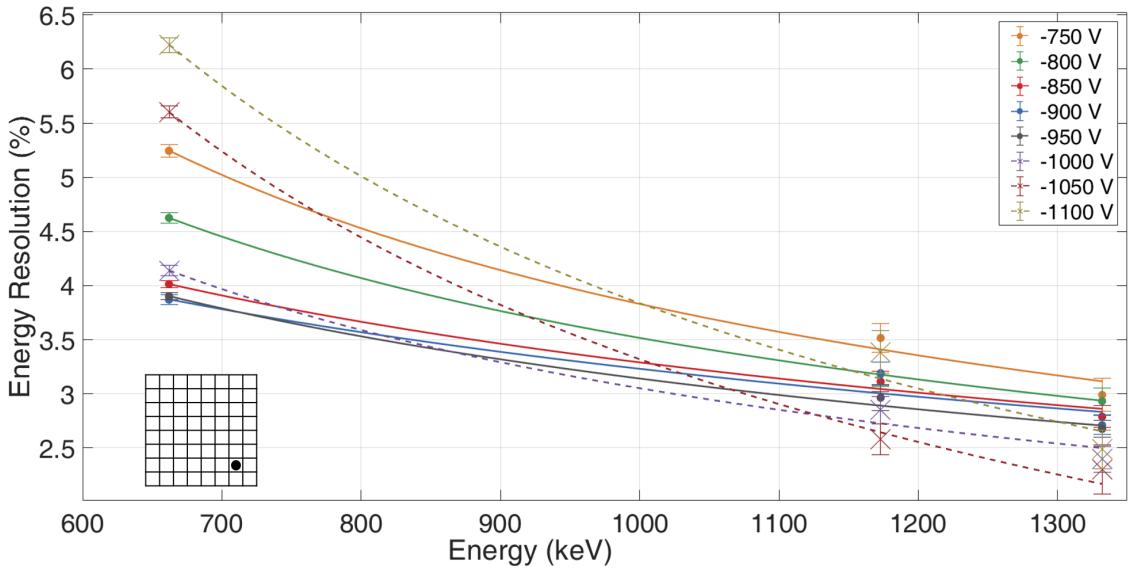

Figure 4.12: Relative energy resolution of System 2 as a function of the photon energy (keV) of collimated γ-ray calibration sources for different PMT (H8500) supply voltages. The dashed lines represent PMT voltages $\geq$ 1000 V. The insert illustrates the position of the collimated sources (blackdot) in front of the lower right corner of the detector.

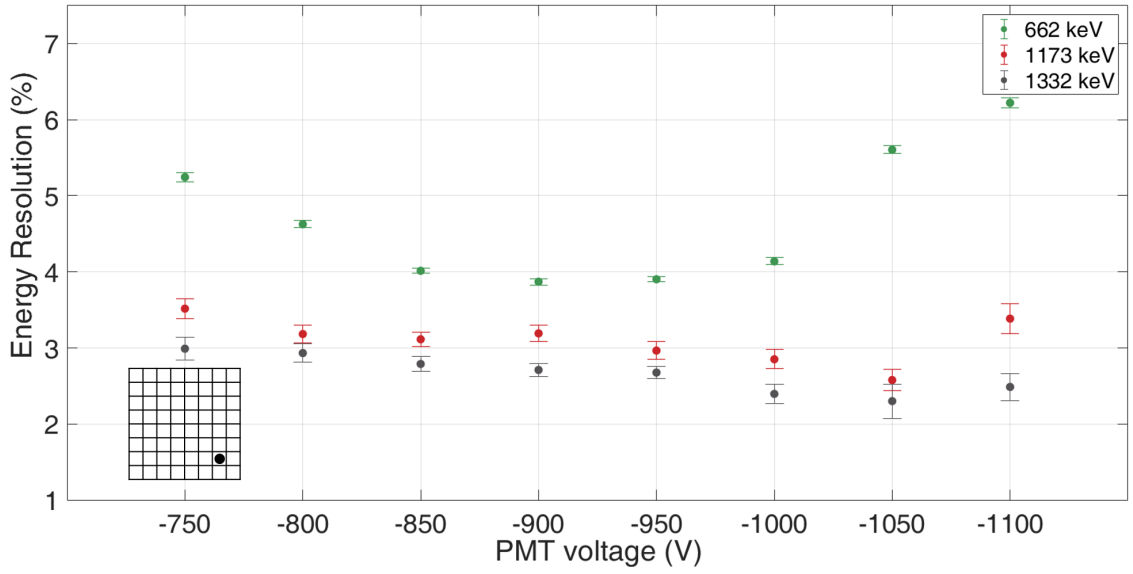

Figure 4.13: Relative energy resolution of System 2 as a function of the high voltage applied to the PMT (H8500) obtained with collimated γ-ray calibration sources. The insert illustrates the position of the collimated sources (blackdot) in front of the lower right corner of the detector.

Although for System 3 the PMT is different from the one used in System 1 and

2, the maximum supply voltage that can be applied is also -1100 V. Fig. 4.14 shows the energy resolution of System 3 as a function of the incoming photon energy of collimated γ-ray sources placed in a central position in front of the detector surface. For PMT voltages ranging from -750 to -950 V, the energy resolution has a tendency to improve with an increasing photon energy and PMT voltage. It should be noted that for the lower applied voltages (-750 V to -950 V), the energy resolution, for higher photon energies (1173 keV and 1332 keV), tends to be comparable within the uncertainties. However, as seen before for the H8500 PMT, for -1000 and -1050 V the energy resolution has a tendency to degrade for lower photon energies and to improve for higher ones. In contrast, for the highest absolute applied voltage at -1100 V, the energy resolution improves for lower photon energies but it tends to decline for higher photon energies.

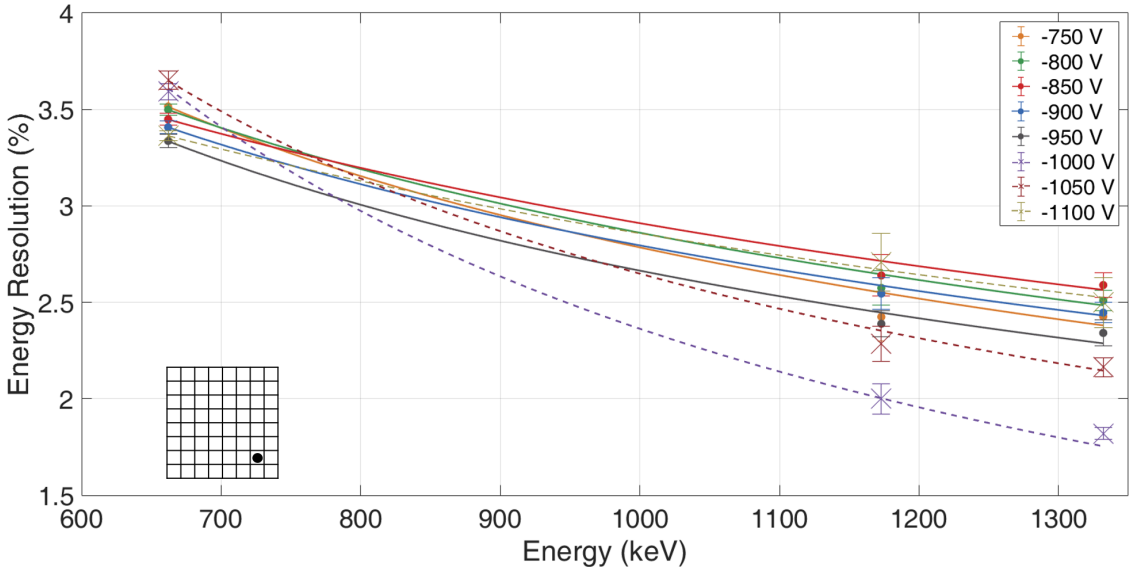

Figure 4.14: Relative energy resolution of System 3 as a function of the photon energy (keV) of collimated γ-ray calibration sources for different PMT (H12700) supply voltages. The dashed lines represent PMT voltages $\geq$ 1000 V. The insert illustrates the position of the collimated sources (blackdot) in front of the lower right corner of the detector.

Fig. 4.15 shows the energy resolution as a function of the PMT supply voltage. For a photon energy of 662 keV, the energy resolution tends to stay constant within the error bars for voltages lower than -950 V. At -950 V and -1100 V a minimum energy resolution is observed, however, for -1000 V and -1050 V the energy resolution tends to deteriorate. For higher photon energies of 1173 keV and 1332 keV the dependence of the energy resolution on the applied PMT voltage is similar to the one observed for System 1 and 2, where a minimum energy resolution is reached for

a PMT voltage around -1000 V. The observed differences between this system and System 1 and 2 occur due to the different performance of the PMTs, namely the differences of the quantum efficiency and gain.

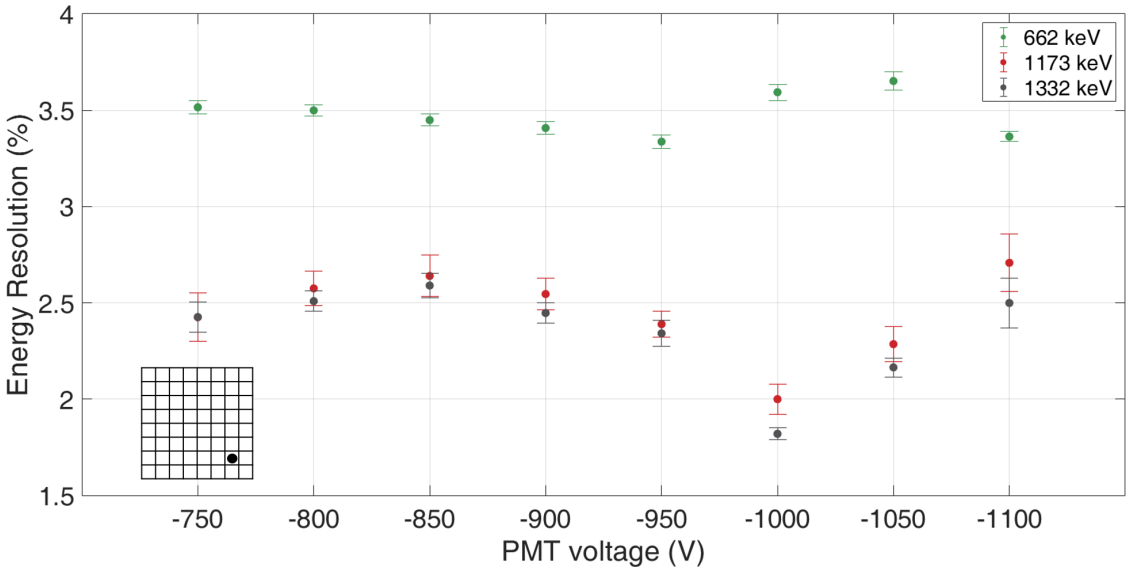

Figure 4.15: Relative energy resolution of System 3 as a function of the high voltage applied to the PMT (H12700) obtained with collimated γ-ray calibration sources. The insert illustrates the position of the collimated sources (blackdot) in front of the lower right corner of the detector.

Based on this systematic study it can be concluded that overall and as expected the energy resolution improves for higher photon energies. Moreover, for the three detector systems studied it was observed that for voltages ranging from -750 to -950 V the relative energy resolution improves with an increase of the absolute voltage. It is also observable that the detectors' performance for voltages beyond -1000 V declines. A possible explanation for these lattest results is that higher supply voltages lead to an increase in the PMT's dark current, due to the possible emission of electrons from the dynodes by the strong electric field, leading to electron losses between the dynodes. However, this effect should only be strongly effective for voltages exceeding the maximum supply voltage recommended by the manufacturer [71], while in our case merely an onset of this effect might have been observed.

4.3 Photon interaction position determination

4.3.1 Photon interaction position-reconstruction algorithms

In order to reconstruct the position in the crystal where the (first) photon interaction occured and to evaluate the crystal's spatial resolution, statistical methods based on the nearest neighbour rule were used. The formulation of a method using this rule was firstly introduced by Fix and Hodges [72] in 1951. Since then, this learning algorithm has been applied to many diverse applications. Maas et al. [73], for example, implemented it for photon interaction position reconstruction in monolithic crystal scintillator detectors. At TU Delft extensive work has been carried out to not only apply the method in medical physics for PET [74, 75], but also to improve the k-Nearest-Neighbour (k-NN) algorithm performance. Therefore, van Dam et al. [76] proposed several modified k-NN methods. Two of them are currently used by our group, namely the "k-NN smoothed" and the "CAP smoothed" algorithms, which will be explained in the following subsections. To use these algorithms, in order to determine the interaction position of a γ ray on the crystal's surface plane (since these algorithms do not provide depth-of-interaction capabilities), the detector needs to be calibrated before. This calibration is done by acquiring a large set of reference data, called reference library, with a collimated γ-ray source perpendicularly irradiating the crystal surface, as illustrated in Fig. 4.16, at a large number of known positions, in x and y directions.

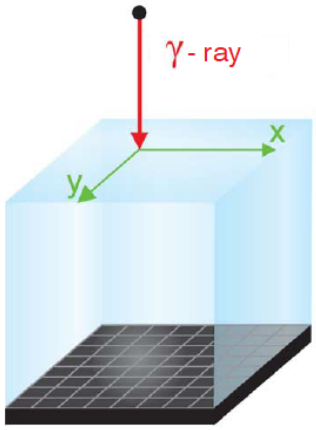

Figure 4.16: Illustration of the irradiation of the crystal surface of a monolithic scintillator with a perpendicularly irradiating collimated γ-ray source in an (x,y) known position and position-dependent scintillation light readout (figure adapted from [76]).

4.3.1.1 k-Nearest Neighbours (k-NN) smoothed algorithm

As previously mentioned, a reference library has to be acquired at a large number n_{pos} of known positions, in order to enable the use of the k-NN algorithm. For each irradiation position, the resulting 2D light amplitude distribution I = (I_1, I_2,..., I_N) is recorded, where N is the number of PMT pixels. The multiplication of the number of known positions n_{pos} recorded with the number of photopeak events recorded per position n_{epp} results in the total number of events contained in the reference library according to

$$n_{\text{tot}} = n_{\text{pos}} \cdot n_{\text{epp}} \tag{4.4}$$

In order to determine the interaction position of an unknown event, its measured 2D light amplitude distribution $I_{unknown}$ is compared to each of the reference entries $I_{reference}$ and the Euclidean distance D is calculated by

$$D = \sqrt{\sum_{i=1}^{N} (I_{unknown,i} - I_{reference,i})^2} \tag{4.5}$$

Afterwards, a subset of the reference library is created containing the k values that show the smallest values of D. These k values are commonly denominated "nearest neighbours". The coordinates of the nearest neighbours are then used to create a 2D histogram, called the k-NN histogram. In our group, the "k-NN smoothed" version was chosen, which means that the histogram is smoothed using a moving average filter of 5 × 5 bins before determining the irradiation position. The coordinates (x,y) of the maximum value of the smoothed histogram are then assigned to the unknown event position.

4.3.1.2 Categorical Average Patterns (CAP) smoothed algorithm

An improved version of the k-NN algorithm, proposed by van Dam et al. [76], was also used by our group. The CAP smoothed algorithm was chosen because of its superior performance with respect to the achievable spatial resolution determination. In this method the coordinates of the unknown event position of interaction are determined by calculating its Euclidean distances D (Eq. (4.5)) relative to those of all reference events. A subset of the reference library containing the k nearest neighbours light amplitude distributions is then created and an average light distribution

is calculated. This process is repeated for each irradiation position contained in the reference library. The subsets obtained are smoothed with a moving average filter, similar to the one used in the smoothed k-NN algorithm. Afterwards the Euclidean distances (Eq. (4.5)) of the unknown event relative to all average light distributions are calculated. The coordinates (x,y) of the k values with the minimum distances D are then assigned to the unknown event position.

4.3.2 Experimental setup

The experimental setup used to acquire the reference libraries, and therefore to evaluate the crystal scintillator's spatial resolution, is described in this section. The measurements were performed using two different γ-ray sources, a ^{137}Cs and a ^{60}Co source with an activity of 77.7 MBq and 15.2 MBq, respectively. While ^{137}Cs emits a 662 keV γ-ray, the ^{60}Co source emits two coincident γ rays of 1173 keV and 1332 keV. In order to acquire enough statistics at a sequence of known irradiation positions, the scintillator crystal, connected to a motorized translation stage, was placed in front of a stationary collimated source.

The collimated source was attached via a tantalum source holder to the backside of a DENSIMET ® (ρ=18.5 g/cm^3) collimator block (10 × 10 × 10 cm^3), which contains a central bore of ∼4 mm diameter, where a 1 mm collimator rod from WC can be inserted, as can be seen in Fig. 4.17. This collimation system was kept stationary and surrounded by lead shielding bricks in order to protect the environment from the high radiation emitted by the source and to ensure that the radiation reaches the detector only through the collimator front opening.

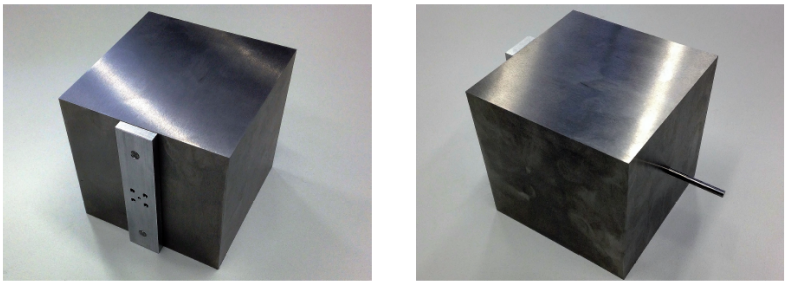

Figure 4.17: Photograph of the collimation system. This is composed of a DENSIMET® collimator block which contains a central bare of ∼4 mm diameter, a collimator tube rod from WC with an inner diameter of 1 mm, placed in the opening, and a tantalum source holder placed at the backside of the shielding block. The collimated source is attached with two screws to the source holder.

On the other hand, the $LaBr_3:Ce^{+3}$ scintillator crystal coupled to the H8500 PMT was positioned in an aluminum frame connected to a motorized translation stage by an aluminum arm, placing it as close as possible (i.e. with a distance of few mm) to the collimation system. This translation stage was used to move the detector in both x and y directions, in front of the collimated source. A length of 36 cm was chosen for the high-density ribbon cables that connect the PMT to the adapter boards in order to allow free movement during the detector movement. The translation stage, sketched in Fig. 4.18 (a), is remotely controlled by a step motor controller. The translation system is monitored and controlled via the MARABOU data acquisiton system [62], described in Sect. 3.1.2.3, an MBS and ROOT [63] based data acquisition system. This way it is ensured, by counting the number of events in a predefined photopeak-energy analysis gate, that the detector is irradiated in each position for the required time to acquire a preselected number of photopeak events.

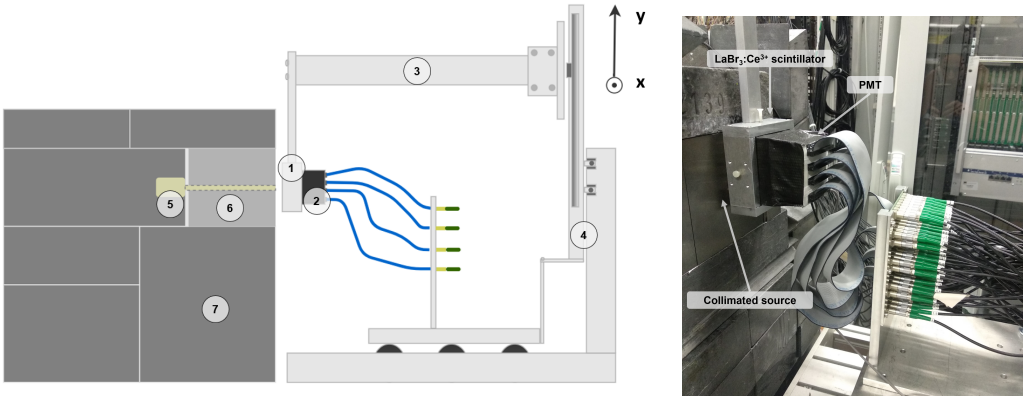

(a) (b)

Figure 4.18: Sketch a) and photograph b) of the experimental setup used for the 2D detector scan. The $LaBr_3:Ce^{3+}$ scintillator (1) coupled to the PMT (2) is supported by an aluminum frame and connected via an aluminum arm (3) to a motorized translation stage (4). The collimated source (5) is attached to a DENSIMET® block (6) and this system is surrounded by lead shielding bricks (7).

4.3.3 Correction Steps

The raw data needs to be corrected in order to ensure that the response of all PMT pixels is consistent. This correction process has 5 steps that are consecutively applied to the raw data's light amplitude distribution:

- **Gain Matching** As explained in Sect. 3.1.2.3, 64 electronic readout channels are needed to process the electronic signals from all PMT pixels. Each PMT segment is connected to its own MCFD channel, resulting in a variation of

the individual gains. In order to remove this gain variation, each channel gain is measured by feeding two pulser signals with different amplitudes (500 and 1000 mV) into the 64 LEMO signal cables. This pulser signals are generated by a digital detector pulse emulator (digital detector emulator DT5800 from CAEN [77]). The gain coefficient is then derived for each of the 64 channels, and the raw energy of the channels is calibrated using this parameter through the following equation:

$$E_{\text{corrected}} = \text{gain} \times E_{\text{raw}} + \text{offset} \tag{4.6}$$

- **Pedestal Subtraction** The electronic components of the MQDC produce a dark current, resulting in a low-amplitude peak, the so-called pedestal peak, added to the measured energy spectrum. As for the variation of the amplifier gain described before, the amplitude of this intrinsic noise varies from channel to channel. This motivates the need to measure the pedestal peak independently and subtract it from the digitized signal. In order to only acquire this peak, all energy signals and single gates from the MQDC are unplugged. A typical spectrum that can be acquired this way can be seen in Fig. 4.19. A Gaussian fit is then applied to the pedestal peak of every channel and an energy threshold corresponding to 3σ of the Gaussian peak width [5] can be used as a low energy threshold applied to the data during offline analysis.

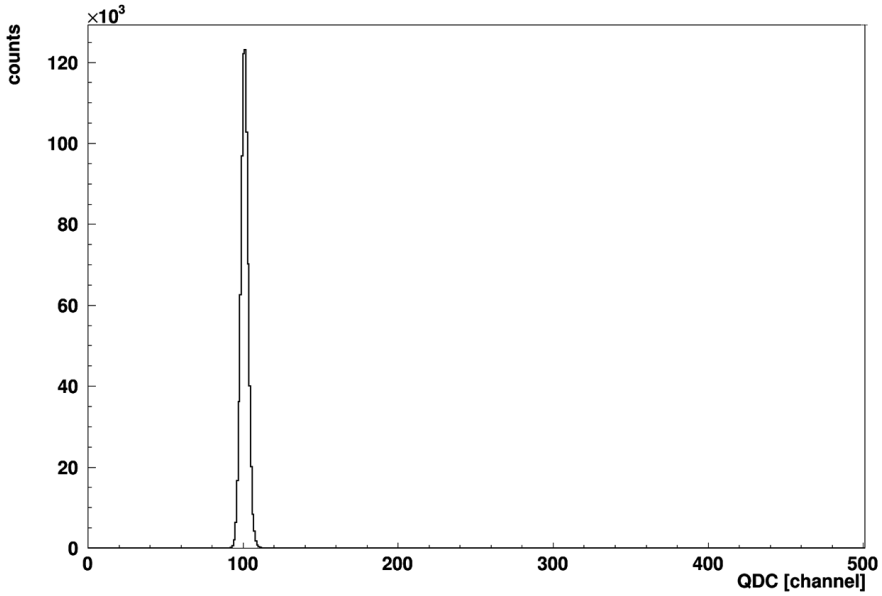

Figure 4.19: Pedestal peak acquired during measurements for one of the 64 PMT signal channels.

- **PMT non-uniformity** A non-uniformity matrix is provided by the PMT manufacturer (see Appendix B) in order to take into account the gain differences between each of the 64 channels of the PMT. Each value from this matrix is divided by the maximum value of all of them, resulting in correction factors that are then applied to the data to correct the 2D light amplitude distribution.
- **Spatial crystal homogeneity** By recurring to an isotropically emitting photon source, placed in front of the detector, it is possible to correct for a potentially anisotropic spatial response of the crystal due to scattering or reflection of the scintillation light in the corners and at the edges of the detector. However, the $LaBr_3$:Ce^{3+} scintillator's internal activity can be considered homogeneously distributed across the crystal volume, therefore offering an isotropic emission of radiation. In order to measure the crystal's internal radioactivity spectrum and acquire the inhomogeneous spatial response of the crystal, the crystal must be shielded from external background radioactivity by using lead blocks. Afterwards the registered energy is gated in the region of interest, i.e. in the photopeak energy region, in order to produce the position dependent correction matrix, which is then applied to the data.
- **Energy gating** Lastly, an energy gate around the photopeak energy region is applied to the energy spectrum. This step enhances the signal-to-background ratio for the incident γ rays of interest.

The measurement of the correction factors, with the exception of the PMT uniformity, which is provided by the manufacturer, is performed shortly before each reference library acquisition in order to assure that the potentially varying external (e.g. temperature) conditions of all measurements are taken into account and correction factors are adequately applied to the raw data during the acquisition process. The influence of applying the consecutive correction steps to the raw data during a 2D light amplitude distribution reference library acquisition can be seen in Fig. 4.20. It is possible to see the impact of these steps, since when all the corrections are applied, Fig. 4.20 (f), a correct visualization of the true irradiation position of the collimated source is obtained, represented in each subfigure by the white dot in the upper right corner.

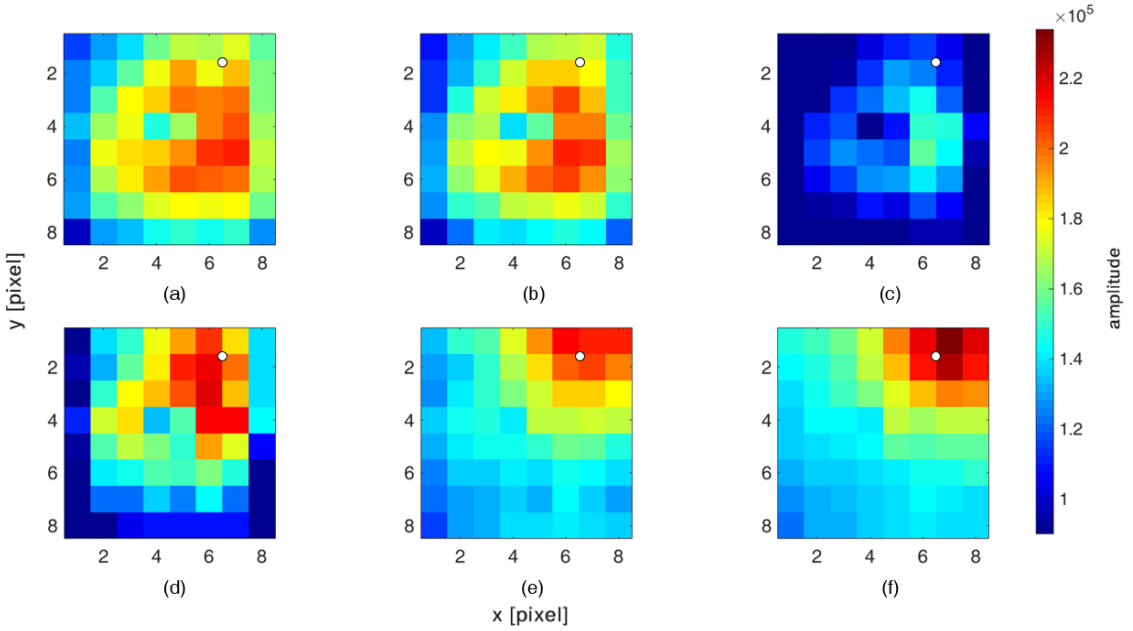

Figure 4.20: Consecutive correction steps applied to the raw data during a 2D light amplitude distribution acquisition with a ^{137}Cs collimated source. The white dot in each subfigure represents the real source position. From top to bottom and left to right: (a) raw data; (b) gain matching; (c) pedestal subtraction; (d) PMT uniformity; (e) spatial crystal homogeneity and (f) energy gating. For a detailed explanation of these correction steps see the main text.

4.3.4 Crystal edge scan

Measurement and fitting

Before starting the reference library acquisition, the exact location of the crystal inside its aluminum encapsulation has to be determined in order to calculate the starting coordinates of the scan. The location and exact crystal dimensions are determined by performing a so-called edge scan. This scan is performed by scanning the detector's surface across the edge regions in both x (x-scan) and y (y-scan) directions with a γ-ray collimated source and a fine step size of 1 mm using the experimental setup described in Sect. 4.3.2. The detector is positioned in front of the collimator by setting one of the coordinates to the central plane, while the other one varies from one edge region of the detector to the other. This way it is possible to visualize the crystal profile indicated by the increasing (rising edge) and decreasing (falling edge) number of counts registered in the photopeak as a function of the irradiation position. The intensity profile of the rising slope of the x-scan is

fitted by a Fermi function according to

$$f_r(x) = \frac{A}{1 + e^{\frac{x-x_0}{B}}} + C \tag{4.7}$$

where A, B and C are fit parameters, x_0 is the origin of the x axis and x is the irradiated position. The intensity profile of the falling slope is similarly fitted using an inverse Fermi function

$$f_f(x) = \frac{A}{1 + e^{\frac{x_0-x}{B}}} + C \tag{4.8}$$

The same fitting procedure is applied for the y-scan, where the x and x_0 values are replaced by y and y_0. Both fits provide inflection points which represent the starting and ending coordinates of the crystal. The width of the crystal, which ideally corresponds to the one provided by the manufacturer, can then be determined by calculating the distance between these two points.

Results

The crystal edge scans were measured using two different collimated γ-ray sources,^{137}Cs and ^{60}Co, and a collimator opening of 1 mm. The measurements were performed with a step size of 1 mm and a range of coordinates slightly larger than the actual crystal size, to ensure that the crystal edge is crossed. The acquisition time per irradiation position is presented in Table 4.3. Due to the higher activity of the ^{137}Cs source its edge scans were performed with a shorter time per position.

Source	**Time per position** (s)	
	x-scan	y-scan
^{137}Cs	760	760
^{60}Co	1080	1080

Table 4.3: Acquisition time per irradiation position used for the edge scans performed with ^{137}Cs and ^{60}Co collimated sources.

The performed x- and y-scans of the crystal edges using ^{137}Cs (662 keV) and ^{60}Co (1.17 MeV and 1.33 MeV) sources are shown in Fig. 4.21. In order to filter out only photopeak events, energy gates place around the photopeak energy were applied to the raw data. Obviously the statistics is superior in the edge scans performed

using ^{137}Cs compared to ^{60}Co, reflecting the fact that the ^{137}Cs source activity is much higher (∼5 times) than for the ^{60}Co source.

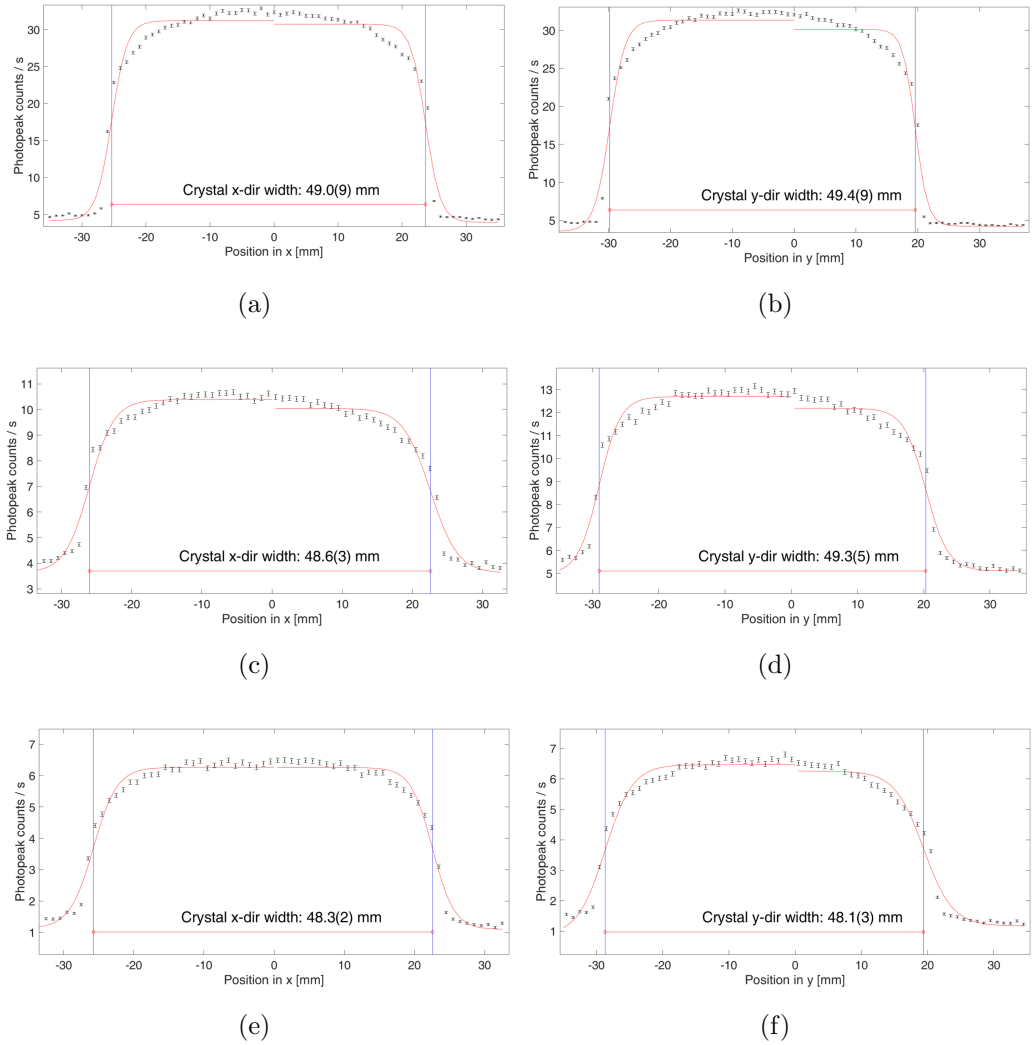

Figure 4.21: Crystal edge scans obtained using ^{137}Cs ((a) and (b)) and ^{60}Co ((c), (d), (e) and (f)) collimated sources, for both x and y directions. Already during data acquisition, photopeak counts are selected by gating in the region of the photopeak energies: (a) and (b) are obtained by gating on the 662 keV photopeak region of the ^{137}Cs source; (c) and (d) are obtained by gating on the 1.17 MeV photopeak region of the ^{60}Co source and (e) and (f) are obtained by gating on the 1.33 MeV photopeak region of the ^{60}Co source.

The Signal-to-Background Ratio (S/B), considering an average of the x- and y-scan, is ∼ 7.5 for ^{137}Cs, while for the ^{60}Co source it is ∼6 for the 1.33 MeV photopeak and ∼3 for the 1.17 MeV photopeak. The S/B is lower for the γ lines of the ^{60}Co source. Moreover, it is noticeable, when comparing the two profiles obtained by gating on the ^{60}Co photopeaks, that the background level is higher for

the 1.17 MeV (Fig. 4.21 (c) and (d)) than for the 1.33 MeV (Fig. 4.21 (e) and (f)) photopeak, since the former lies on top of the Compton continuum of the latter.

The calculated crystal widths deviate by $\sim$ 2% to $\sim$ 5.3% from the nominal crystal dimensions (50.8 $\times$ 50.8 mm^2) as provided by the manufacturer. This difference may occur due to the fact that some scattering occurs in the crystal edge regions leading to photopeak count rates lower in the edge positions than in the centre, which affects the fit quality in the flat-top region of the scan and consequently the inflection point value. Moreover, the crystals reflective wrapping may not be 100% efficient and a fraction of the scintillation photons may escape from the crystal.

4.3.5 Light amplitude reference libraries

After measuring the correction factors and determining the starting coordinates of the scan through the crystal edge scan, the reference libraries were acquired using two different collimated sources, ^{137}Cs and ^{60}Co, with an activity of 77.7 MBq and 15.2 MBq, respectively and a PMT voltage of -900 V. These were acquired at 102 $\times$ 102 irradiation positions (n_{pos}=10404) with a step size of 0.5 mm, which corresponds to the radius of the collimator opening, therefore scanning an area of 51 $\times$ 51 mm^2. In order to decrease the acquisition time, instead of defining the same acquisition time for all positions, as done for the crystal edge scan, a dynamic adjustment of the acquisition time per irradiation position was implemented ensuring that 600 photopeak events (n_{epp} =600) were recorded per irradiation position. The total library size will therefore be the number of photopeak events per position n_{epp} multiplied by the the total number of irradiation positions n_{pos}. In the case of the ^{137}Cs source reference library about 5 days of continuous measurement were required to scan the detector's front face. In comparison, since the ^{60}Co source activity is about 5 times lower than the ^{137}Cs source, the ^{60}Co source reference library was completed within 18 days. In order to acquire the reference libraries the DAQ is synchronized to the translation stage motor controller, which is controlled through the MARABOU acquisition system, allowing to apply the correction steps previously described already online. For each of the n_{pos} an ASCII file is generated containing the light amplitude distribution for each of the 64 channels and for each of the 600 recorded events. These files are afterwards converted into one MATLAB file, since the photon interaction position-reconstruction algorithms are applied using MATLAB. Subsets of the 2D light amplitude distribution reference libraries acquired with the ^{137}Cs source (gated at 662 keV) and the ^{60}Co source (gated at 1.17 MeV and

1.33 MeV) for 8 × 8 irradiation positions, covering the scintillators front surface, with a grid scan size of 6 mm, are shown in Fig. 4.22, Fig. 4.23 and Fig. 4.24, respectively.

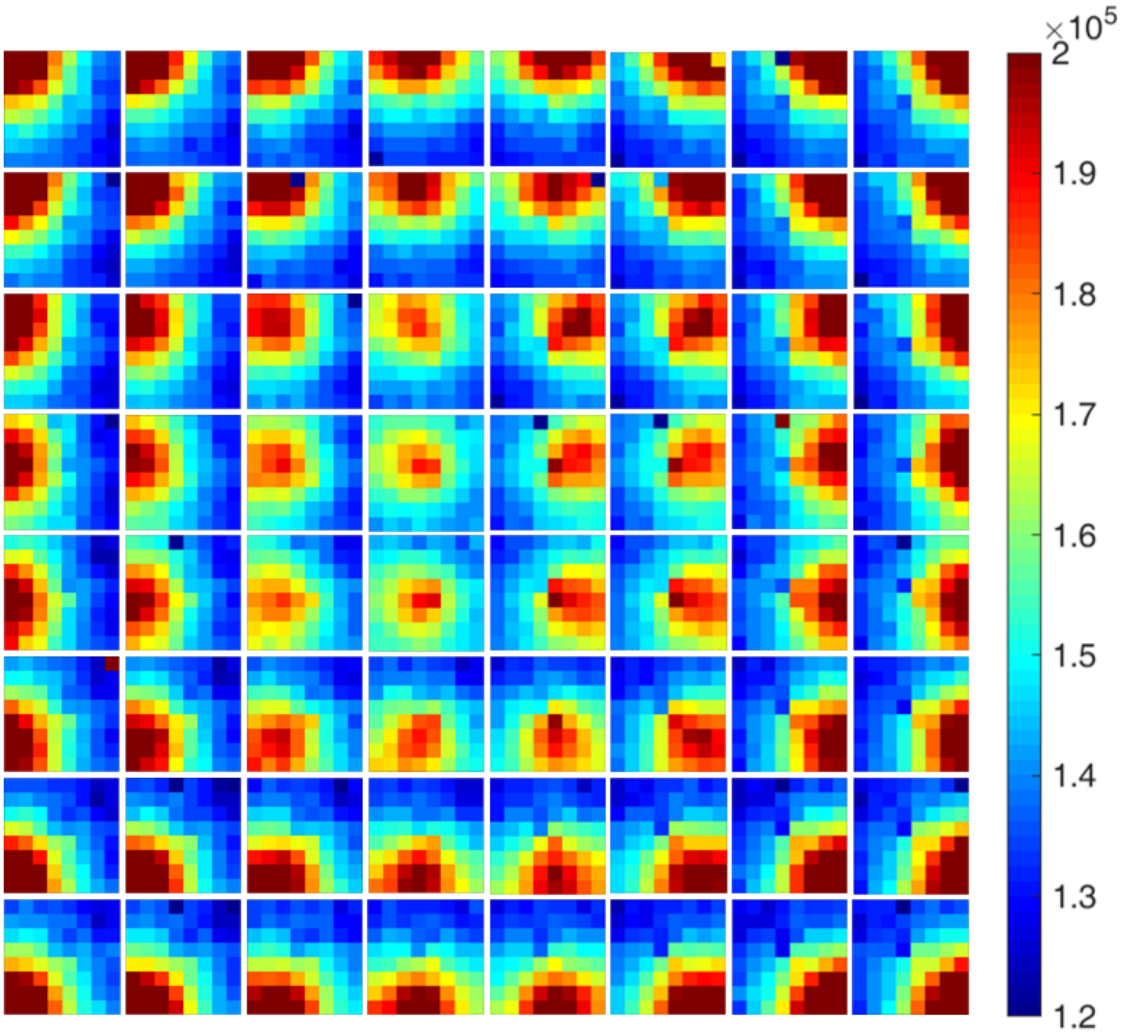

Figure 4.22: Series of 2D light amplitude distribution maps (from an 8 × 8 segmented PMT readout) acquired with a 1 mm collimated ^{137}Cs source and a 6 mm step size in x and y directions.

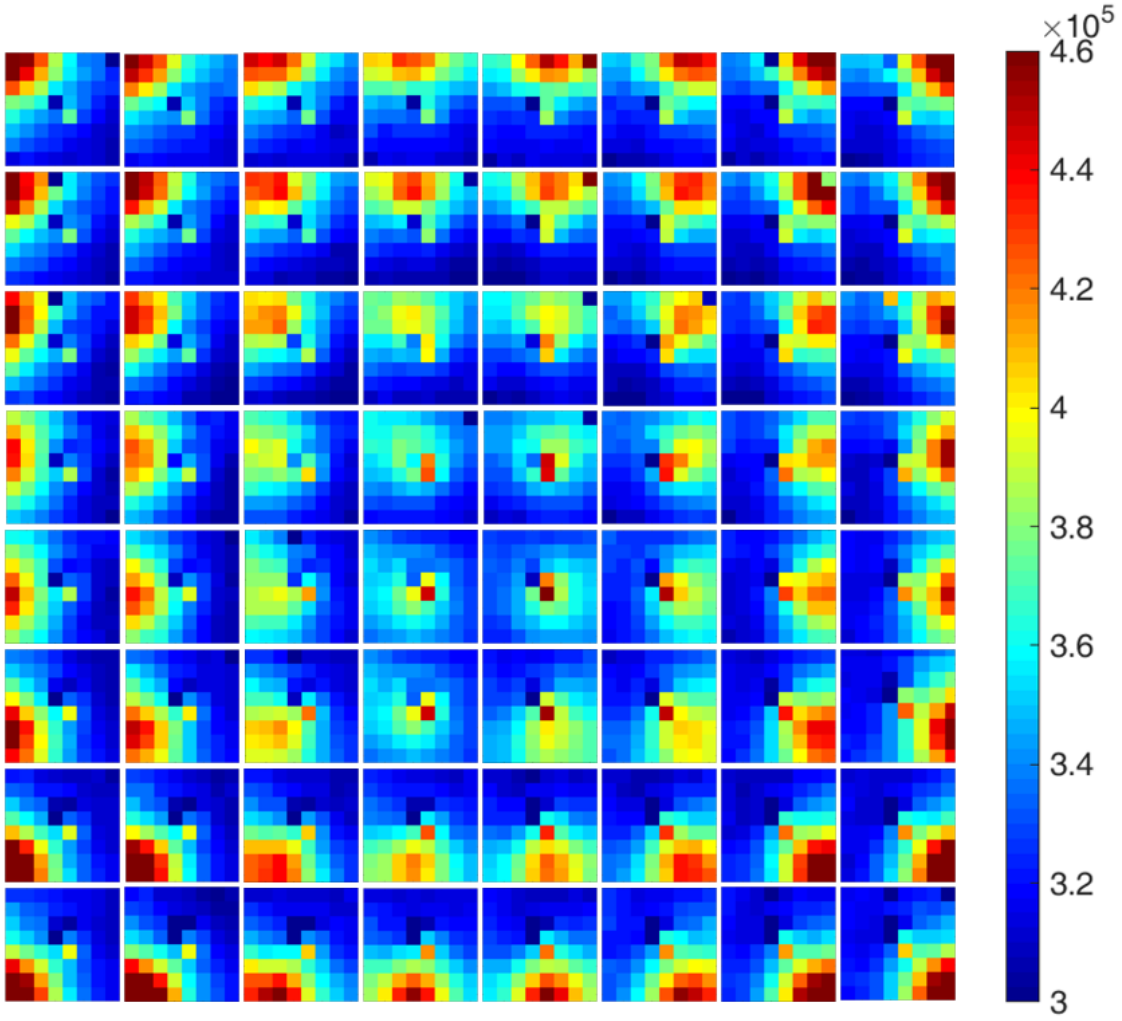

Figure 4.23: Series of 2D light amplitude distribution maps (from an 8 × 8 segmented PMT readout) acquired with a collimated ^{60}Co source, gated on the 1.17 MeV photopeak, and a 6 mm step size in x and y directions.

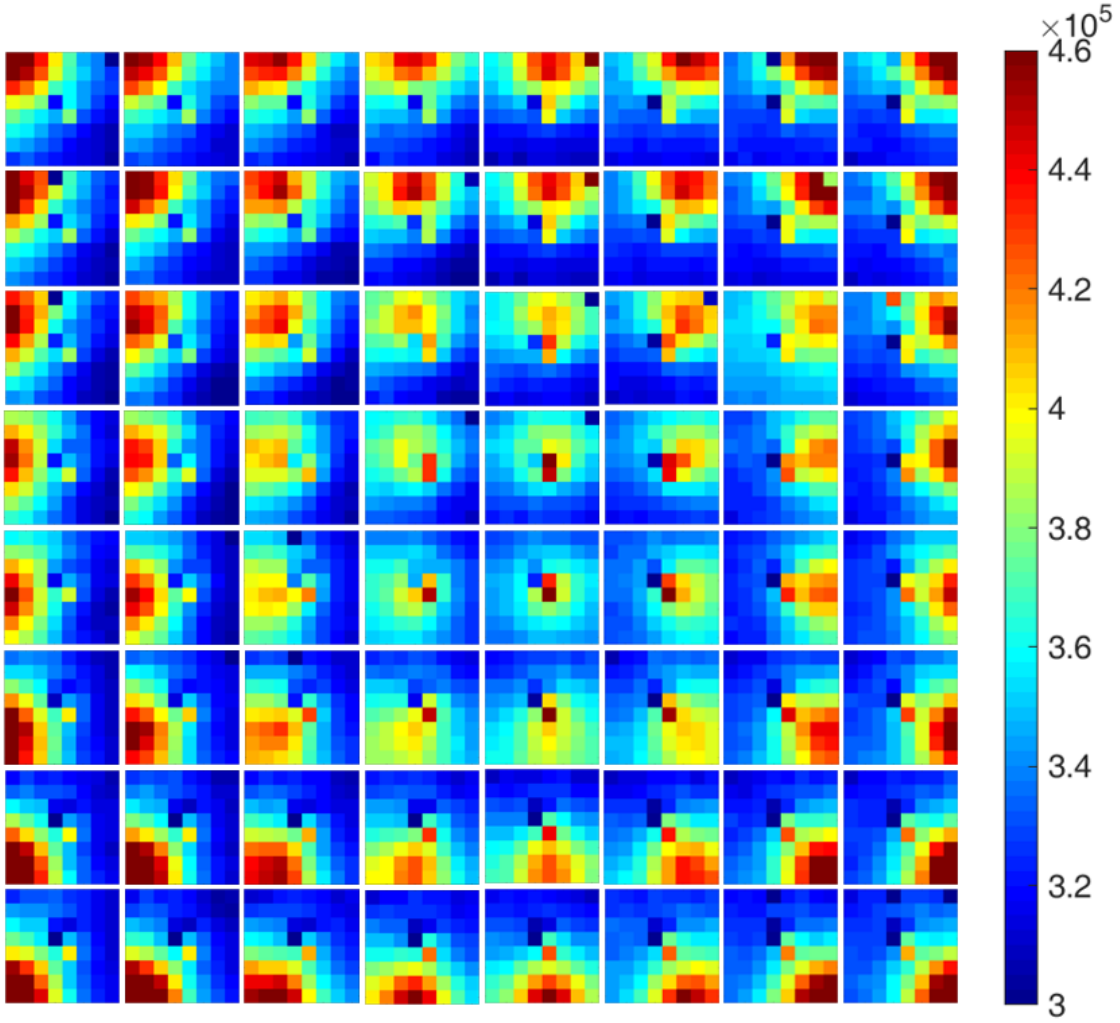

Figure 4.24: Series of 2D light amplitude distribution maps (from an 8 × 8 segmented PMT readout) acquired with a collimated ^{60}Co source, gated on the 1.33 MeV photopeak, and a 6 mm step size in x and y directions.

4.3.6 "Blank Pixel" Correction

The large amount of data produced in the electronic data acquisition is prone to data artifacts and signal loss in individual PMT segments in some of the recorded events. This signal loss is manifested by zeroes in the data stream of pixel intensities, named "raw zeroes". Besides these "raw zeroes" acquired in the raw data, "pedestal zeroes" can also occur. When the pedestal correction step is applied, all energy values below the previously determined threshold, which corresponds to the digital MQDC channel that separates the dark current region from the acquired physical signal, will be assigned as dark current. It may happen that for some pixels only low scintillation light amplitudes are acquired, leading to its value to be set to zero. In the framework of a previous Master Thesis by Michael Mayerhofer [2], the source of these zeroes, so called "blank pixels" was studied, however, it was not traceable to a specific hardware component, e.g., the step motor of the translation stage or the readout electronics. Therefore, due to the necessity of replacing the "blank pixels" with realistic physical values to achieve a meaningful determination of the photon interaction position in the crystal, different correction algorithms were studied. The developed Categorical Gaussian Distributed Replacement (CGDR) algorithm by Michael Mayerhofer was the one that showed more promising results when being applied to the reference libraries acquired for the Compton camera's first absorber crystal, which finally enabled to reach a sub-3mm spatial resolution [78].

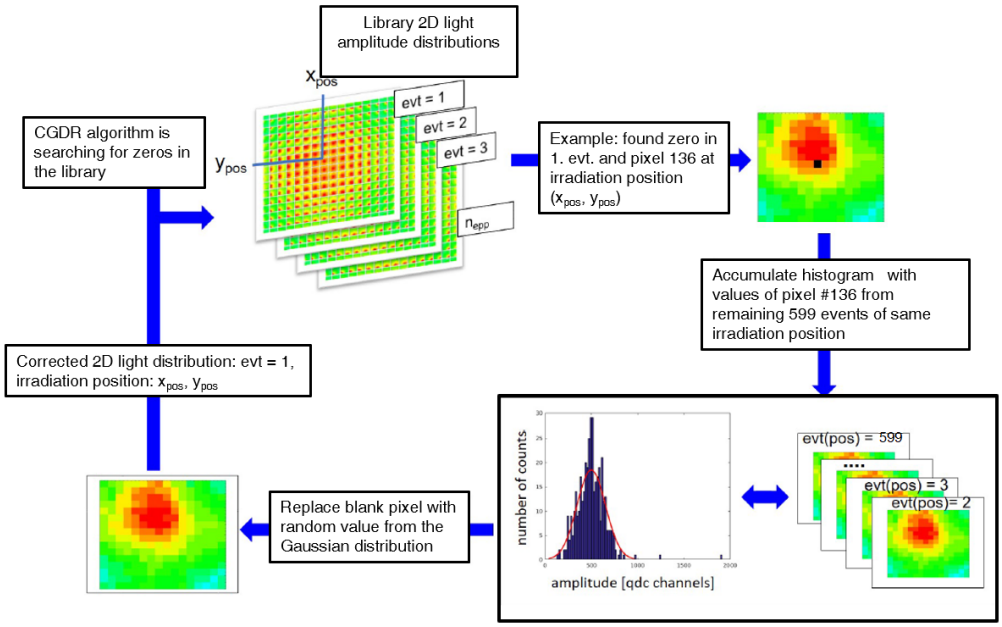

Figure 4.25: Categorical Gaussian Distributed Replacement (CGDR) flowchart (adapted from [2]).

This algorithm, which flowchart is shown in Fig. 4.25, identifies the positions of the "blank pixels" and generates the distribution of all non-zero values from the remaining ensemble of events measured at the same irradiation position, which is then parametrized by a Gaussian fit. Through this fit an amplitude value, between the standard deviation values -3σ and +3σ of the Gaussian distribution, is randomly picked and used to replace the "blank pixels" value.

The number of "blank pixels" present in the ^{137}Cs and ^{60}Co libraries acquired for the new Compton camera absorber component in the framework of this thesis, Sect. 4.3.5, is shown in Table 4.4. Even though the "blank pixels" represent only a small fraction of all entries in the acquired data, as seen in Table 4.4, they are still able to influence the correct determination of the spatial resolution. Therefore, there is a need to correct for their presence.

Source	**Nº of blank pixels**	**Fraction of all entries** (%)
^{137}Cs	$\sim 8 \times 10^5$	0.210
^{60}Co	$\sim 2 \times 10^4$	0.005

Table 4.4: Number and fraction of "blank pixels" contained in the ^{137}Cs and ^{60}Co reference libraries acquired for the new Compton camera absorber component, the $LaBr_3$:Ce^{3+} scintillation crystal coupled to a 64-segmented PMT (H8500).

In order to correctly apply the CGDR algorithm it must be ensured that the distribution of the light amplitude from the recorded events at the various irradiation positions follows a Gaussian distribution. Therefore, two positions were randomly picked and their light distribution was measured for a specific PMT pixel.

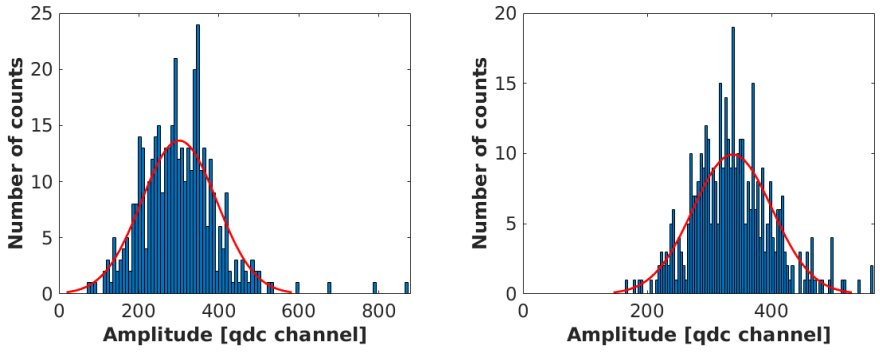

(a) (b)

Figure 4.26: Distribution of light amplitudes measured for two randomly chosen irradiation positions for specific PMT pixels. The number of acquired library entries per irradiation position was n_{epp}=600.

In both cases a Gaussian distribution was found (Fig. 4.26), as indicated by the Gaussian fit (red curve). Thus it is justified to apply the CGDR algorithm to the newly acquired data.

In order to check the quality of the replacement values, the generated light amplitudes were normalized to the standard deviation σ of their respective Gaussian distribution and accumulated in a histogram, as displayed in Fig. 4.27. The plot shows a Gaussian distribution indicating that the "blank pixels" values were replaced with accepted physical values in agreement with the distribution of the rest of the library at this specific library position.

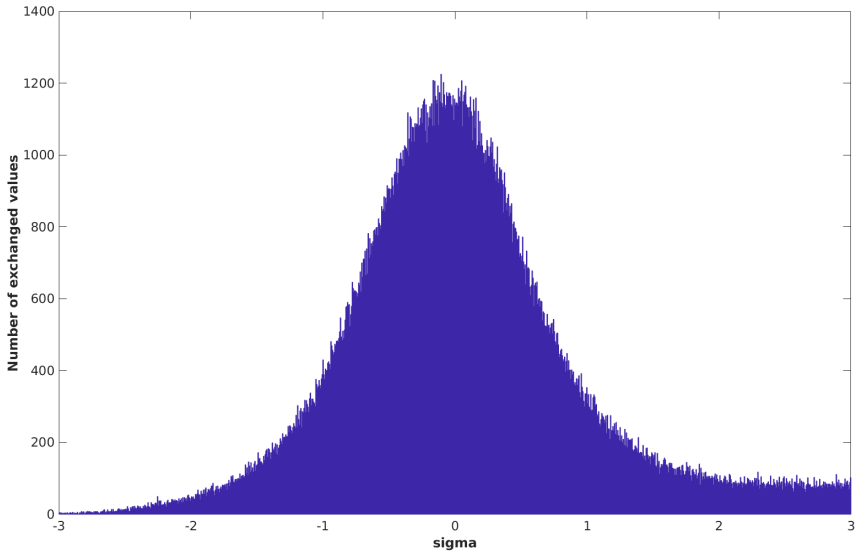

Figure 4.27: Histogram of the normalization of the replaced values of the "blank pixels", generated by the CGDR algorithm, to the standard deviation σ of their respective Gaussian distribution.

4.4 Determination of the absorber's spatial resolution

The last section of this chapter focuses on the determination and discussion of the absorber's spatial resolution. Firstly, the method used to derive the spatial resolution for the different reconstruction algorithms will be described. Secondly, the results obtained in previous studies for the first acquired absorber detector will be presented and discussed. Finally, the achievable spatial resolution for the new Compton camera absorber component, studied in this Master thesis, will be presented as a function of different parameters. The results obtained will be discussed and compared to the ones obtained for the previous absorber detector.

4.4.1 "Leave-one-out" Method

In Sect. 4.3.1 the "k-NN smoothed" and "CAP smoothed" algorithms are described in detail. These algorithms allow for determining the detector's spatial resolution through the so-called "leave-one-out" method. Fig. 4.28 schematically shows the workflow of the CAP smoothed algorithm as well as of the leave-one-out method. In order to use this method, one event from the previously acquired reference library is selected and treated as an "unknown" event, while the other reference events constitute the reference set. The interaction position of this event is then calculated using the CAP smoothed algorithm and subsequently compared to its true value. This method is repeated for all n_{pos} irradiation positions contained in the reference library. The coordinates differences $\triangle x$ and $\triangle y$ between the calculated and the true interaction positions are filled into an error histogram. The resulting average of the FWHM of the x and y projections of this histogram represents the spatial resolution.

4.4.2 Previous studies

In this subsection the reference libraries and spatial resolution values obtained for the first acquired absorber component, a $LaBr_3$:Ce^{3+} crystal coupled to a 256-fold segmented PMT (H9500), in the framework of previous Master theses [1, 2], will be presented and discussed. The spatial resolution was studied as a function of the k value of the chosen reconstruction algorithms (k-NN and CAP smoothed), the number of events per position n_{epp}, the scan pitch size, photon energy and PMT

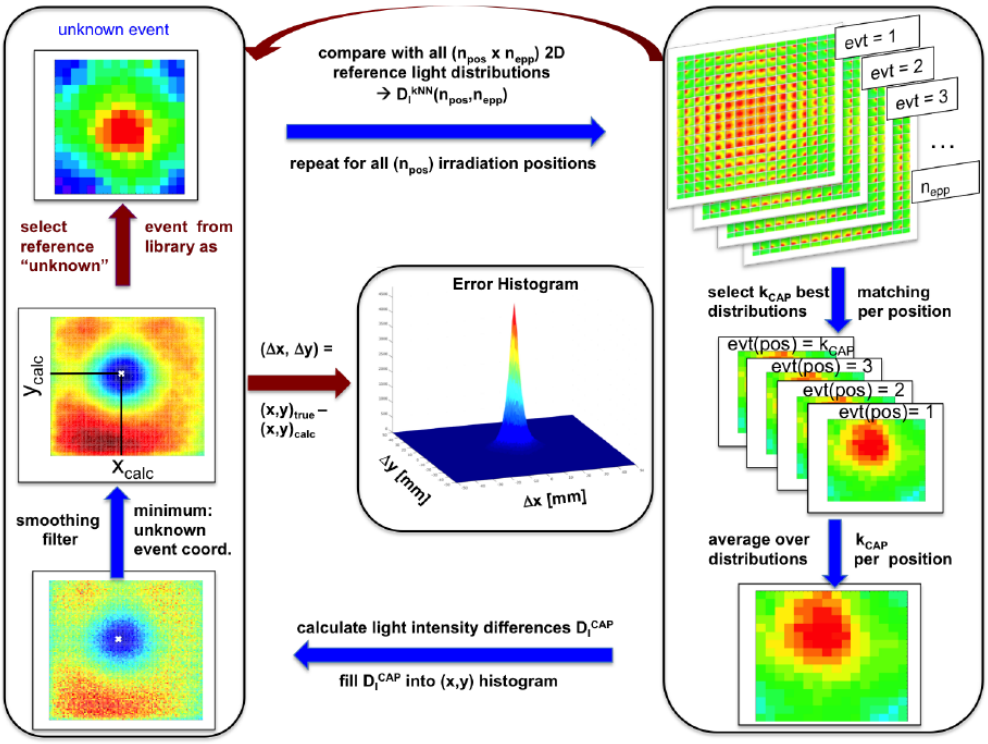

Figure 4.28: Workflow of the CAP smoothed algorithm for the photon interaction position-reconstruction [5], described in detail in Sect. 4.3.1.2.

granularity. Two reference libraries were created from the same raw data, with 400 photopeak events (n_{epp} =400) recorded per irradiation position, one consisting of the 2D light distributions of 256 pixels directly acquired from the experimental data, and another one with 64 pixels created during the offline analysis by summing up, through software, the light amplitudes of each four neighbouring pixels from the full 256 pixels light distribution, as illustrated in the following sketch of Fig. 4.29. This way the behaviour of an 8 × 8 multi-anode PMT is mimicked.

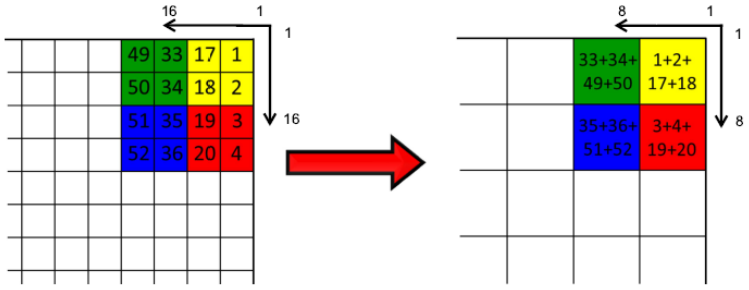

Figure 4.29: Sketch of the procedure used to create the 64-pixel 2D light amplitude distributions from the originally acquired 16 x 16 multianode PMT data [1].

It was determined that the optimum values for the k parameter were 12 for the

CAP smoothed algorithm and 1000 for the k-NN smoothed algorithm, respectively. Moreover, the best spatial resolution, while using the previously mentioned k values, was obtained for $n_{epp} = 400$, the maximum number of events per position recorded, and for a scan pitch size of 0.5 mm. These studies also found that there is a dependence of the spatial resolution on the impinging γ-ray energy, meaning that for higher photon energies a better spatial resolution was observed. The optimum determined spatial resolution as a function of the γ-ray energy, for the two studied PMT granularities of 64 and 256 channels and for both reconstruction algorithms, after "blank pixel" correction, is plotted in Fig. 4.30.

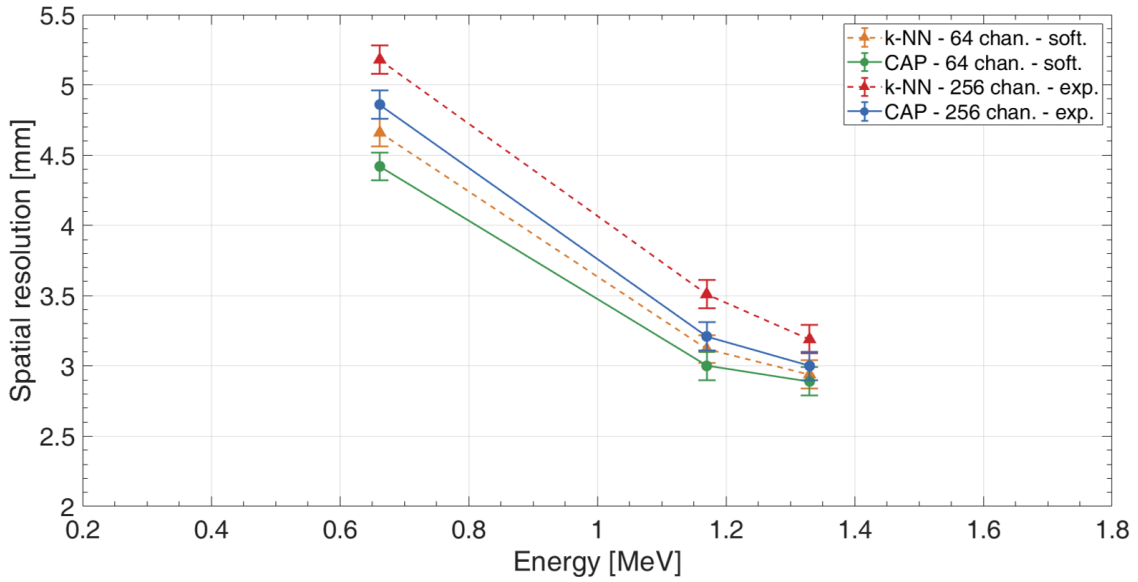

Figure 4.30: Spatial resolution of a monolithic $LaBr_3:Ce^{3+}$ scintillator, obtained in previous studies, as a function of E_γ. The spatial resolution, determined with the CAP smoothed and k-NN smoothed reconstruction algorithms for the two PMT granularities of 64 and 256 channels is displayed as a function of the incident γ-ray energy. The underlying reference libraries consist of 400 photopeak events per irradiation position and were acquired with a 1 mm collimator and 0.5 mm scan step size [1, 2].

As expected, the CAP smoothed algorithm outperformed the k-NN smoothed algorithm for both PMT granularities. Moreover, it is clearly visible that the spatial resolution depends not only on the energy of the incoming γ ray, decreasing with an increasing γ-ray energy, but also on the PMT granularity, improving with its decrease. This improvement may occur due to the fact that, when considering same size PMTs, the lower the granularity the larger the pixel size will be, leading to an improved photon statistics of the scintillation light in each pixel. The optimum values obtained for the spatial resolution using the CAP smoothed algorithm and

after "blank pixel" correction, using the offline CGDR algorithm, are presented in Table 4.5.

N° channels	**Spatial Resolution (mm)**		
	662 keV	**1.17 MeV**	**1.33 MeV**
256	4.7(1)	3.2(1)	3.0(1)
64	4.2 (1)	3.0(1)	2.9(1)

Table 4.5: Spatial resolution of a $LaBr_3$:Ce^{3+} crystal scintillator coupled to a 256-fold segmented PMT determined for three different photon energies, and different PMT granularities (64 channels by software summation of each 4 neighbouring pixels), using the CAP smoothed algorithm [1, 2].

As already stated in Sect. 1.3 the main objective of this thesis is to experimentally study the performance of the new $LaBr_3$:Ce^{+3} crystal scintillator read out by a truly fold 64-segmented PMT in order to determine whether the previously obtained results for 64 pixels through software summation can be experimentally reproduced. Therefore, in the remaining sections of this chapter, the acquired results for the spatial resolution of the new system will be presented.

4.4.3 Results and discussion

The systematic study of the detector's spatial resolution determined using the "leave-one-out method" of the k-NN smoothed and CAP smoothed algorithms will be presented and discussed in the following sections. The spatial resolution was studied as a function of the two main variables that needed to be optimized, i.e. the number of nearest neighbours k and the number of reference events per irradiation position n_{epp}. The spatial resolution was determined via the "leave-one-out method" for different k values. The number of nearest neighbours was varied within a certain range, depending on the applied algorithm. For the k-NN smoothed algorithm, since in this case the k closest matching reference light distributions are chosen from the complete reference set consisting of around $\sim 10^6$ light distributions ($n_{pos} \times n_{epp}$), the set of values chosen for k ranges from 3 to 4000 were:

$$\begin{aligned} k_{\text{k-NN}} = \{&3, 5, 10, 20, 30, 40, 50, 70, 100, 200, 300, \\ &400, 500, 700, 1000, 1200, 1500, 2000, 3000, 4000\} \end{aligned} \tag{4.9}$$

where

$$k_{\max}(\text{k-NN}) \ll n_{\text{pos}} \times n_{\text{epp}} \tag{4.10}$$

On the other hand the CAP smoothed algorithm seeks the k best values among the available events per irradiation position n_{epp}, therefore the set of values studied for this algorithm differ from the ones chosen for the k-NN scenario according to:

$$k_{\text{CAP}} = \{5, 10, 12, 14, 15, 25, 30, 40, 50\} \tag{4.11}$$

where

$$k_{\max}(\text{CAP}) \ll n_{\text{epp}} \tag{4.12}$$

In order to study the n_{epp} dependence, individual reference libraries subsets were created for different n_{epp} values by selecting the first n_{epp} events from the total number of collected events, e.g., the $\text{n}_{\text{epp}} = 150$ sub-library contains the first 150 photopeak events recorded at each irradiation position. The values chosen range from 75 to 600:

$$n_{\text{epp}} = \{75, 100, 150, 200, 300, 400, 500, 600\} \tag{4.13}$$

Although the previously acquired libraries only contain 400 reference photopeak events per irradiation position, it was observed that the spatial resolution tends to (slightly) improve with an increase of the available statistics. In order to assess if the spatial resolution continues to improve when using more than 400 photopeak events per irradiation position, it was decided to acquire 600 events per position in the current study.

Moreover, a study of the impact of the energy of the incident photons on the detector's spatial resolution was performed. Since the LMU Compton camera system is being developed to detect and localize the origin of prompt γ rays emitted in an energy range of predominately 3-6 MeV and originating from the interaction between an ion or proton beam and organic tissue, the spatial resolution must be studied as a function of the incident photon energy. Therefore two collimated sources were used, ^{137}Cs and ^{60}Co, enabling the acquisition of reference events at 662 keV, 1.17 MeV and 1.33 MeV. Although the targeted photon energy range is considerably higher than the one reachable by these sources, this study enables to at least catch

a glimpse at the $LaBr_3$:Ce^{3+} detector's spatial resolution as a function of the incident γ-ray energy.

4.4.3.1 Spatial resolution as a function of the *k* value

The spatial resolution was first studied as a function of the number k of nearest neighbours for both reconstruction algorithms to determine its optimum value. It was decided to only consider the first 400 events recorded per position ($n_{epp} = 400$) of each reference library in order to establish a direct comparison with the previous studies. Due to the different range of k values used in the two algorithms, their results will be shown separately.

Fig. 4.31 displays the spatial resolution as a function of the k values chosen for applying the k-NN smoothed algorithm k_{kNN} for each reference library for photon energies of 662 keV, 1.17 MeV and 1.33 MeV. It can already be inferred from this first systematic study that there is a tendency for the spatial resolution to improve with an increase of the photon energy, since there is a clear separation between the spatial resolution measured at 662 keV (solid orange line) and the rest of the data corresponding to the ^{60}Co energies (dashed green line and dashed-dotted red line).

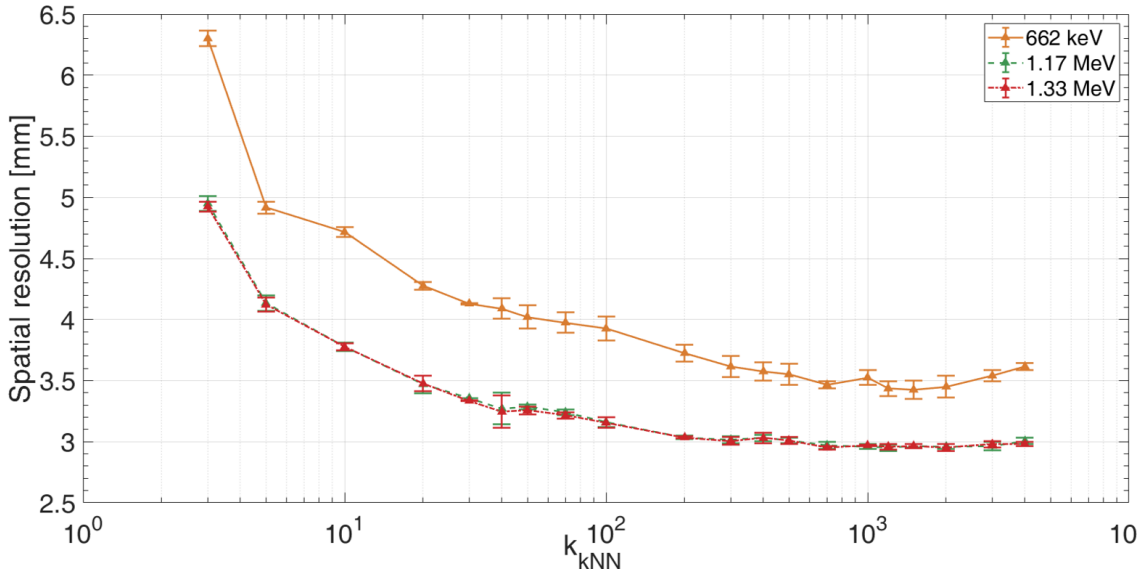

Figure 4.31: Spatial resolution as a function of the k value chosen for the k-NN smoothed algorithm, for $n_{epp} = 400$. The photon energies are distinguished by the line style and colour.

For the three cases presented in Fig. 4.31 the trend of the detector's spatial resolution is similar over the range of studied k_{kNN} values. The detector's spatial

resolution improves with the increase of k_{kNN}, reaching its best value around $k_{kNN} \sim 700$. Increasing this value further leads to an oversampling of the reconstructed photon interaction position and therefore a deterioration of the detector's spatial resolution.

Fig. 4.32 shows the spatial resolution of the reference libraries acquired for photon energies of 662 keV, 1.17 MeV and 1.33 MeV as a function of the k values chosen for applying the CAP smoothed algorithm k_{CAP}. Similarly to the k-NN case, there is apparently a dependence of the detector's spatial resolution on the impinging photon energy, with a more pronounced gap between the ^{137}Cs (solid orange line) and ^{60}Co (dashed green line and dashed-dotted red line) energies than observed before. For all cases the spatial resolution dependence is similar over the range of studied k_{CAP} values. With the increase of k_{CAP} the spatial resolution starts to improve, reaching an optimum for a value of $k_{CAP} \sim 12$. Beyond this value the spatial resolution slowly deteriorates with increasing k_{CAP}, possibly due to oversampling of the reference events by the algorithm.

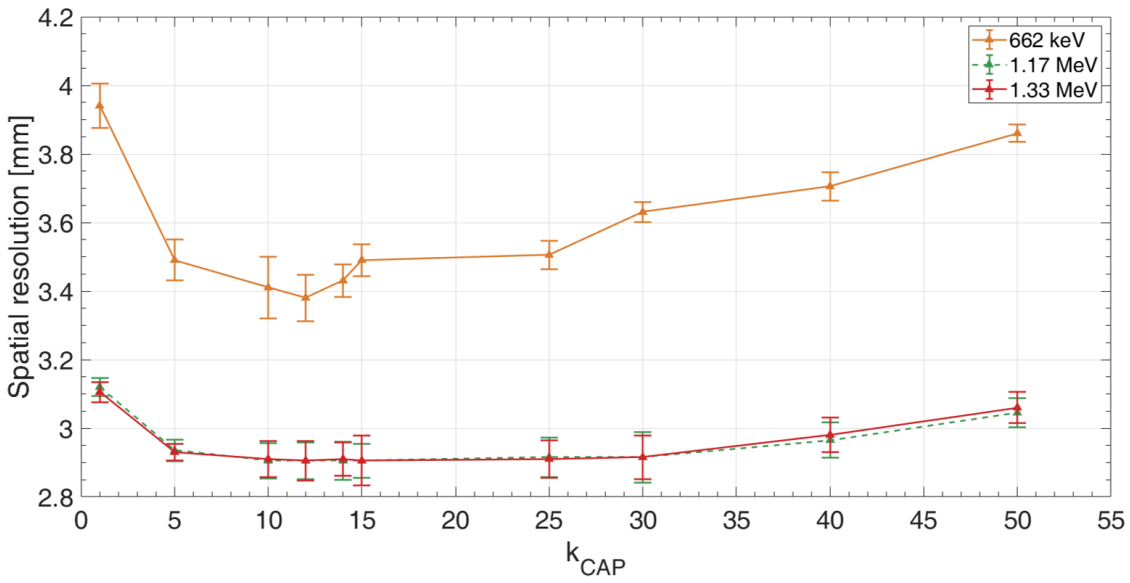

Figure 4.32: Spatial resolution as a function of the k value chosen for the CAP smoothed algorithm, for $n_{epp} = 400$. The photon energies are distinguished by the line style and colour.

Table 4.6 provides the optimum results of the spatial resolution obtained as a function of the incident photon energy achieved for the two reconstruction algorithms, using in each case the determined minimum k values. The results indicate that the applied algorithms display a clear trend when it comes to the number of nearest neighbours used in the reconstruction, exhibiting a minimum k value for

which an optimum spatial resolution is obtained. A dependence of the detector's spatial resolution on the impinging γ-ray energy has been observed and will be further discussed in Sect. 4.4.3.3.

Reconstruction Algorithm	***k***	**Spatial Resolution (mm)**		
		662 keV	**1.17 MeV**	**1.33 MeV**
k-NN smoothed	700	3.5(1)	3.0(1)	3.0(1)
CAP smoothed	12	3.4(1)	2.9(1)	2.9(1)

Table 4.6: Spatial resolution of a $LaBr_3:Ce^{3+}$ crystal scintillator coupled to a 64-channel PMT (H8500), determined for two reconstruction algorithms, k-NN and CAP smoothed, and for three different photon energies, considering $n_{epp} = 400$.

These findings are in agreement with the ones previously obtained [1, 2] for a PMT granularity of 64 channels achieved by software summation from a 256-fold segmented PMT. When comparing the detector's spatial resolution obtained with the k-NN and CAP smoothed algorithms, the conclusion is reached that the latter outperforms the former. Again these results confirm the ones already reached for the first acquired absorber component and it was therefore decided to discard the k-NN smoothed algorithm results in the following systematic studies, focusing on its improved version CAP.

Uncertainties determination

The error bars applied in the previous and following plots of this section have been determined based on the statistical uncertainties of the spatial resolution derived from sub-samples of the whole acquired reference library. The full library containing 600 reference events per position was subdivided in order to create six libraries, each containing 100 events per position. The subsets were not assembled randomly, rather they were selected in ascending order, meaning that the first sub-library contains the first 100 events acquired per position, the second sub-library contains the next 100 events acquired per position and so on. The "leave-one-out" method was applied to each sub-library using the two reconstruction algorithms and the spatial resolution was determined for each of the k values indicated in Eq. (4.9) and Eq. (4.11). The standard deviation of the six spatial resolution values was calculated and assigned as the experimental uncertainty.

This method was performed for all libraries, ^{137}Cs (662 keV) and ^{60}Co (1.17 MeV and 1.33 MeV) and for both reconstruction algorithms. Fig. 4.33 shows an example of the implementation of this method using the CAP algorithm to the

^{137}Cs source reference library.

The uncertainties of the spatial resolution for different values of n_{epp}, namely for values larger than 100, were extrapolated from the one obtained with n_{epp}=100 using Eq. (4.14) according to

$$\sigma(k,n_{epp}) = \sigma(k,100) \times \sqrt{\frac{100}{n_{epp}}} \tag{4.14}$$

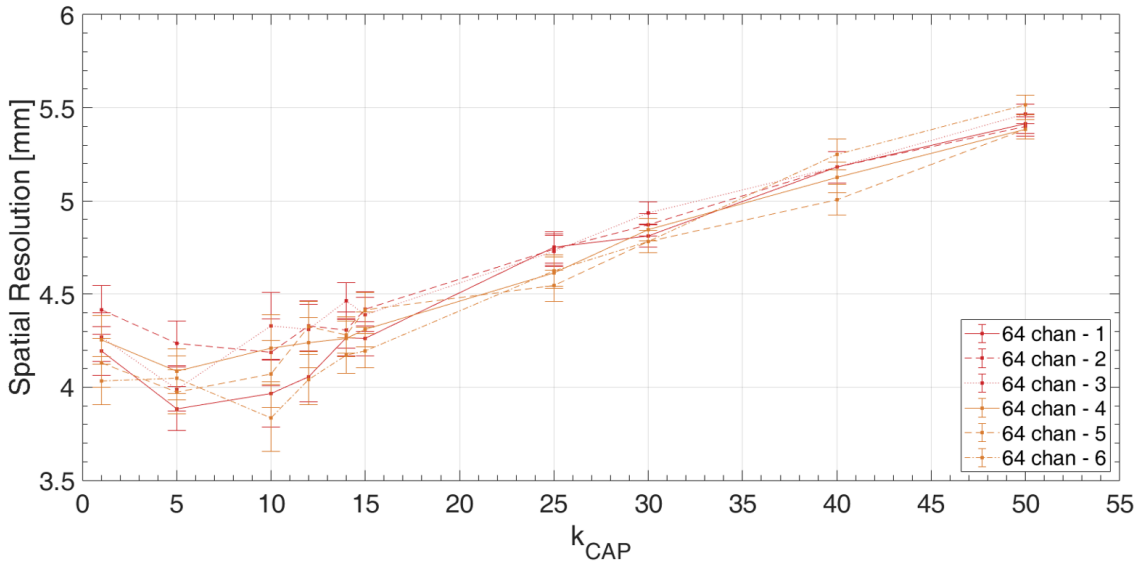

Figure 4.33: Determination of the experimental uncertainties of the detector's spatial resolution. The main reference library, with n_{epp}= 600, acquired for a photon energy of 662 keV, was splitted into six sub-libraries, each containing n_{epp}= 100. In the plot the spatial resolution is shown as a function of the k_{CAP} for each sub-library, distinguished by the index 1-6 in the plot legend.

4.4.3.2 Spatial resolution as a function of n_{epp}

After assessing the optimum k value for the reconstruction algorithms, the dependence of the detector's spatial resolution on the number of events per irradiation position n_{epp} of the reference library was studied. This systematic study was carried out by applying the CAP smoothed algorithm to individual reference libraries created for different n_{epp} values, ranging from 75 to 600, using the optimum k value previously determined as k_{CAP} = 12. It should be noted that depending on the value of n_{epp}, the optimum k_{CAP} value can vary. However, since these values do not differ significantly between the different libraries, and for the obtained spatial resolution to be comparable, it was chosen to present the results using the previously

determined k_{CAP} value.

This study was performed in order to determine if a minimum value of acquired events per position n_{epp} can be used without compromising the optimum value of the resulting spatial resolution. By using an optimized value of n_{epp}, the computational effort required to compare an unknown event with the entries of the reference library can be significantly reduced, as well as the overall measurement time needed to generate the reference libraries. This dependence was also studied by [2] for the reference libraries artificially created for a PMT granularity of 64 channels, after applying the CGDR algorithm and a maximum value of n_{epp}=400.

Fig. 4.34 displays the spatial resolution as a function of the value of n_{epp} for the reference libraries acquired experimentally (solid lines) and by software (dashed lines), for different photon energies (distinguished by the marker style).

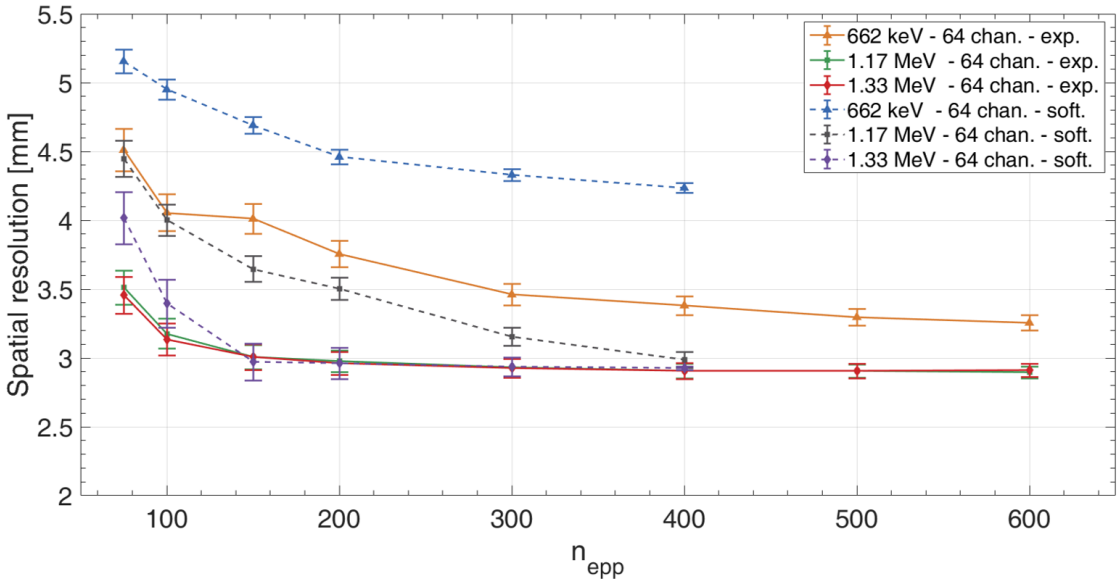

Figure 4.34: Systematic study of the spatial resolution as a function of the number of events per irradiation position n_{epp} obtained for different values of the incident photon energy E_γ, distinguished by the markers. The reference libraries acquired experimentally and by software, for a PMT granularity of 64 channels, are distinguished by the line style. The optimum k_{CAP} value of 12 was chosen for each data set.

In general, the spatial resolution tends to improve with an increasing number of recorded events per irradiation position, which is expected, since a larger number of reference events leads to larger statistics. Therefore, the risk of over-sampling is minimized, since the selection of the k best matching light amplitude distribution is optimized, as can be seen in the previous section. However, for values of n_{epp} larger

than 300 and for the lowest energy from ^{137}Cs, in both presented cases this trend flattens with a further increasing number of n_{epp}. For the ^{60}Co energies this effect is even more prominent and, within the experimental uncertainties, no improvement of the spatial resolution was obtained for n_{epp} larger than ~ 200.

The energy-dependent difference between the number of events recorded per position at which this saturation occurs may be due to the fact that for lower photon energies there is a higher probability of scattering in the detector, leading to a loss of a larger number of photopeak events.

The best spatial resolution of the $LaBr_3$:Ce^{3+} scintillator currently under study was found to be 2.9(1) mm, measured at 1.17 MeV and 1.33 MeV, using reference libraries with $n_{epp} \geq 400$, since the spatial resolution for all measured incident γ-ray energies saturates and turns out to be comparable within their uncertainties. This finding is in agreement with the one reached previously for the reference library created artificially by software summation, as indicated by the results obtained for different photon energies represented by the dashed lines in Fig. 4.34. These results have important implications on the measurement time needed to generate future reference libraries, since it was proven that an optimum spatial resolution can be achieved by acquiring only two thirds of the reference events per irradiation position currently registered ($n_{epp} = 600$).

As first noticed in the previous section, the spatial resolution drops to lower values when going from 662 keV to the ^{60}Co energies (1.17 MeV and 1.33 MeV), leading once more to the conclusion that the photon interaction position reconstruction improves for higher energies. This dependence will be further discussed at the end of the chapter.

It is clear from the analysis of the graphs presented in Fig. 4.34 that the results achieved for a true 64-fold PMT segmentation are superior to the ones achieved by software. This improvement is more evident for the photon energy of 662 keV, where an improvement of more than 0.5 mm is noticeable for $n_{epp} = 400$. However, for higher photon energies, the values obtained for both cases and for a number of 400 recorded events per position, are comparable within their error bars.

4.4.3.3 Spatial resolution as a function of the γ-ray energy

This last section is dedicated to the study of the correlation between the impinging γ-ray energy and the achieved spatial resolution. The comparison between the results obtained using the CAP algorithm for the reference library acquired

experimentally and the ones obtained for the reference library created by software summation for a PMT granularity of 64 channels and a value of $n_{epp} = 400$ can be seen in Fig. 4.35. It is clearly visible that, as previously observed in Fig. 4.32 and Fig. 4.34, the spatial resolution tends to improve with the increase of the impinging γ-ray energy. This improvement can be attributed to the fact that the increase of the collected scintillation light improves the statistics of the intensity recorded in the reference library. This effect is more evident between 662 keV and 1.17 MeV, since the results achieved for 1.17 MeV and 1.33 MeV are rather similar, within the experimental uncertainties, for the data obtained from the true 64-fold segmentation. This may be due to the fact that the ^{60}Co energies lie rather close to each other, and therefore the difference between them is not enough for a improvement in the spatial resolution to be noticeable.

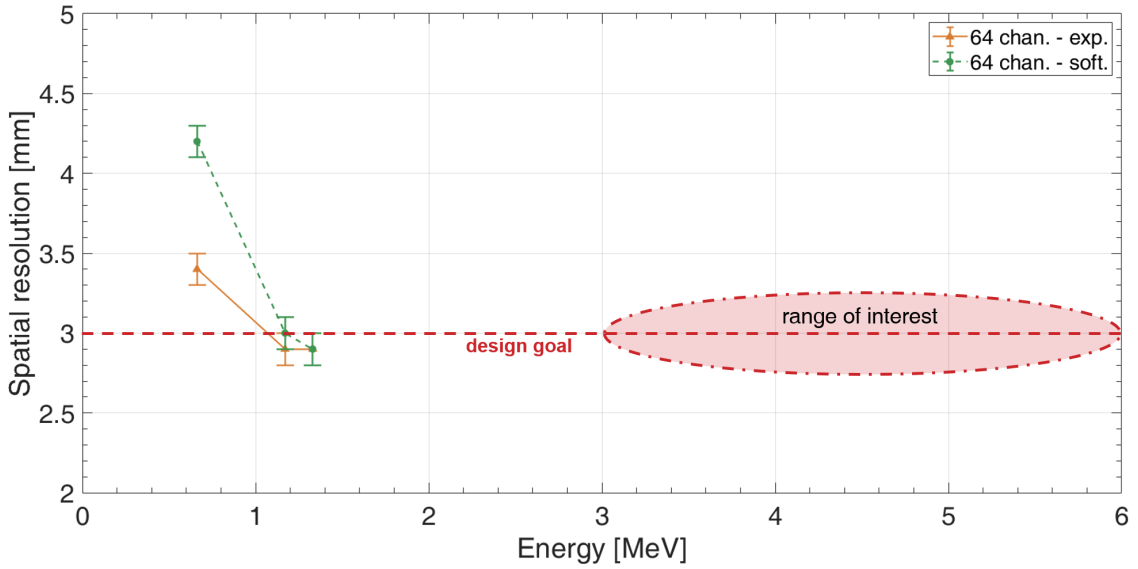

Figure 4.35: Spatial resolution as a function of E_γ, comparing the data set acquired for a PMT granularity of 64 channels obtained experimentally (orange solid line) and created by software from an initially 256-fold segmented PMT (green dashed line). The data were acquired with a 1 mm collimator, a 0.5 mm scan pitch size and an optimized k_{CAP} value of 12 for $n_{epp} = 400$. The vertical red dashed line denotes the design goal of 3 mm for the LMU Compton camera absorber, while the elliptically shaded area indicates the range of energies of interest for prompt-γ imaging in hadron-therapy.

The horizontal red dashed line, included in Fig. 4.35, marks the design goal of 3 mm for the spatial resolution of the absorber component of the LMU Compton camera for an energy range of 3 to 6 MeV, according to the design simulations performed by Christian Lang in a previous PhD thesis [8]. As stated by this simulation study, a 3 mm spatial resolution of the absorber would enable to reach an overall

spatial resolution of about 2 mm of the Compton camera in a small-animal irradiation scenario. This design goal was previously achieved by Michael Mayerhofer in his Master Thesis [2], for a photon energy of 1.33 MeV, when implementing the CGDR algorithm into the data analysis process of the artificially created reference library of a monolithic $LaBr_3:Ce^{3+}$ scintillator crystal for a PMT granularity of 64 channels. In the course of the present Master Thesis this goal was experimentally achieved not only for a photon energy of 1.33 MeV, but also for a lower energy of 1.17 MeV, for a new $LaBr_3:CeBr^{3+}$ crystal scintillator read out by a 64-segmented PMT. These findings are directly in line with the ones previously achieved, leading to the conclusion that when the monolithic scintillator crystal is read out by a 64-segmented PMT, instead of a 256-segmented PMT, a better or at least similar spatial resolution is achieved.

It is furthermore believed that a spatial resolution of the absorber component below the design goal of 3 mm even for multi-MeV photons, whose range is represented in Fig. 4.35 by the red shaded area, is within reach, considering the well-localized photon-interaction process of pair creation that increasingly contributes at photon energies well above 1 MeV.

5

Conclusions and outlook

The alarming number of new cancer cases and deaths that emerge each year have led to an increasing need for new and more effective cancer treatment modalities. For some non-metastatic cancers, the currently most promising cancer therapy is hadron therapy. This treatment modality enables the delivery of a high radiation dose to a specific tumour volume while minimizing the effects on the surrounding healthy tissue. However, due to possible beam range uncertainties introduced by the treatment planning and delivery, in-vivo range verification techniques need to be applied in order to avoid irradiation of healthy tissue during the beam delivery, while ensuring that the maximum dose deposition is released in the targeted volume. Over the last few years, different approaches for in-vivo range verification have been proposed. One of these, a Compton camera prototype which exploits the Compton scattering kinematics of the incident prompt photons induced by the nuclear interaction of the impinging particle beam with the targeted tissue and subsequently registered in a suitable detector arrangement, has been under development at the chair of Medical Physics at LMU. This device is composed of a scatter detector (consisting of six layers of DSSSD) and an absorber detector (a monolithic $LaBr_3$:Ce^{3+} scintillation crystal), allowing to reconstruct the origin of the prompt γ rays by exploiting Compton-scattering kinematics. Due to the layered structure of the scatterer, besides detecting the incident photon, the LMU Compton camera prototype is also able to track the Compton-scattered electron.

The main goal of this Master Thesis was to study the performance of a new absorber detector of the LMU Compton camera prototype, a $LaBr_3$:Ce^{3+} monolithic scintillator read out by an 8×8 multianode position-sensitive PMT featuring 64 segments that are processed individually using spectroscopy electronics. This performance can be assessed through the measurement of several physical observables. In particular, in the framework of this thesis the detector's spatial and energy resolution were assessed.

An energy resolution dependence on the irradiation position was observed when scanning the crystal's front surface with a 1 mm collimated photon source. A slightly reduced energy resolution was obtained in the crystal's center, contrary to what would be expected for a monolithic crystal. An average value of the relative energy resolution $\frac{\triangle E}{E} = 4.3(1)\%$ at 662 keV was determined. The same position dependence was observed when testing a different $LaBr_3$:Ce^{3+} crystal, as well as coupling the first crystal to a different type of readout PMT, thus leaving the origin of this counterintuitive, yet small, position dependence unexplained. It was also observed, through a systematic study of the energy resolution as a function of the applied high voltage applied to the PMT, that the best energy resolution achievable for the detector system under study is realized by operating the detector at voltages ranging from -900 to -950 V, where a value of $\frac{\triangle E}{E} = 4.3(1)\%$ at 662 keV was determined, slightly less than the value of 3.8% measured for a first comparable detector crystal read out by a 256-fold segmented PMT. The discrepancy between the two measured values is likely due to the performance of the PMT in use here (H8500), since coupling the same crystal to the more recently developed PMT type H12700 an energy resolution of 3.4% at 662 keV was obtained. This result suggests that in the future the H8500 PMT should be replaced by the H12700 PMT.

The determination of the photon interaction position on the $LaBr_3$:Ce^{3+} scintillator crystal's surface is performed using the k-Nearest-Neighbour (k-NN) smoothed algorithm and its improved version, the Categorical Average Patterns (CAP) smoothed algorithm, both developed at TU Delft for PET applications. Both algorithms compare the 2D light amplitude distribution of an impinging γ ray with a reference library of 2D light amplitude distributions previously acquired at a large number of known positions, in order to reconstruct the photon interaction position. This reference library is obtained by scanning the scintillator's surface with a tightly (1 mm) collimated photon source with a step size of 0.5 mm in both x and y directions, resulting in an irradiation at 102 $\times$ 102 positions. In order to study the energy dependence of the detector's spatial resolution, reference libraries for the absorber component under study were determined using two different collimated sources, ^{137}Cs and ^{60}Co. The reference libraries acquisition was performed by attaching the photon sources to a DENSIMET® collimator block, which is kept stationary and lead shielded, while the scintillation detector is connected to a motorized translation stage which moves the detector in front of the collimated source. Due to the presence of zero pixel values in the acquired data, a replacement algorithm, the CGDR algorithm, described in Sect. 4.3.6, was applied to the reference libraries.

The absorber detector's spatial resolution was determined by applying the so-

called "leave-one-out" method to both reconstruction algorithms. However, after first assessing the spatial resolution as a function of the number k of best matching values from the 2D light distributions contained in the reference libraries (acquired for photon energies of 662 keV, 1.17 MeV and 1.3 MeV) it was inferred that the "conventional" k-NN algorithm is outperformed by its improved version CAP and therefore it was decided to discard the former in the following spatial resolution studies. The spatial resolution was also assessed as a function of the number of events n_{epp} recorded per position and as a function of the impinging γ-ray energy. It was inferred that for a value of n_{epp} larger than 300, for all energies the spatial resolution reached saturation. An improvement of the spatial resolution with increasing energy of the impinging γ-ray was observed. An optimum spatial resolution of 2.9(1) mm was achieved using the CAP smoothed algorithm with $k_{cap} = 12$ at photon energies of 1.17 MeV and 1.33 MeV, for $n_{epp} = 400$. The envisaged design goal of 3 mm for the spatial resolution of the absorber component of the LMU Compton camera was therefore surpassed.

The results experimentally achieved in this thesis are in agreement with the ones previously obtained [1, 2] for a PMT granularity of 64 channels created artificially by software summation, using raw data acquired with a $LaBr_3$:Ce^{3+} crystal coupled to a 256-fold segmented PMT (H9500). It can be concluded that by reducing the number of PMT readout channels of the absorber detector, from 256 to 64, the system's performance is improved. As a consequence of reducing the number of readout electronics channels, the whole detector system is also simplified and more economical.

The reference libraries acquired in the context of this thesis enable the determination of the interaction position of an unknown incident photon event on the crystal surface. These data have already been applied in the image reconstruction process for the characterization of a specific Compton camera arrangement in the context of a different project. This is briefly mentioned here to demonstrate the benefit of the LMU Compton camera developments obtained from the work preformed in the framework of this thesis. A ^{60}Co radioactive source was placed in a distance of 45 mm from the scatterer detector center of a Compton camera system. The interaction position of the scattered photon in the absorber detector was determined using the previously acquired reference library of the corresponding scintillation crystal, allowing for the reconstruction of the source position. The spatial resolution determined for the absorber detector was used as an input for GEANT-4 based simulations. The Compton camera system used in this measurement consisted of a scatter component comprised of a segmented GAGG scintillation array and the

previously characterized $LaBr_3:Ce^{3+}$ scintillation crystal absorber, coupled to the H8500 PMT. This system is under development within the framework of the International Open Laboratory (IOL) collaboration between our group and the group of Taiga Yamaya from the National Institute of Radiological Sciences (NIRS) at the National Institute for Quantum and Radiological Science and Technology in Chiba, Japan. This ongoing collaboration will be explained in detail in Silvia's Liprandi PhD thesis [65]. A typical example for a reconstructed source image obtained in this measurement scenario is displayed in Fig. 5.1.

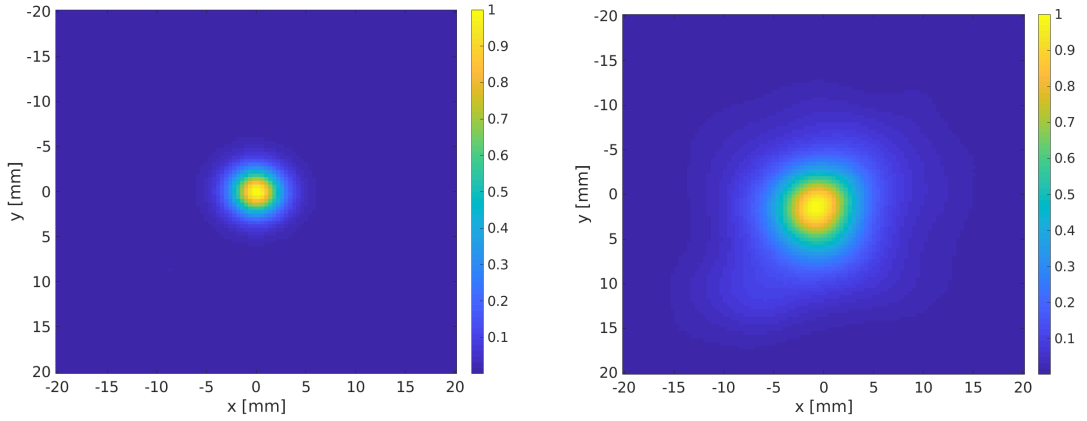

(a) (b)

Figure 5.1: Reconstructed ^{60}Co source position images from simulated (a) and experimental data (b). The source was placed at a distance of 45 mm from the scatterer detector (segmented GAGG scintillation array) center, which is positioned at a 5 cm distance from the previously characterized $LaBr_3:Ce^{3+}$ scintillation crystal absorber, coupled to the H8500 PMT [65].

In order to reduce the cost of the LMU Compton camera prototype, a potential alternative absorber detector material compared to the presently used monolithic $LaBr_3:Ce^{3+}$ scintillation crystal is being investigated, namely a monolithic $CeBr_3$ scintillator of identical dimensions. This crystal shares many of the favourable performance characteristics of $LaBr_3:Ce^{3+}$ at a lower price, moreover, $CeBr_3$ does not possess any internal radioactivity. The time resolution determined for the $CeBr_3$ crystal coupled to the H12700 PMT (281(3) ps (FWHM)) only differs by 5% from the one obtained for the $LaBr_3:Ce^{3+}$ coupled to the H8500 PMT (266(3) ps (FWHM)), thus making them comparable. From the position-dependent energy resolution study performed in this thesis for the $CeBr_3$ crystal, it was inferred that, contrary to what was observed for the $LaBr_3:Ce^{3+}$, the overall energy resolution only slightly varies with the irradiation position, with an observable deterioration in the crystal corners

probably due to scattering effects. However, a 50% reduction of $\frac{\triangle E}{E}$ was observed at 662 keV when comparing the $CeBr_3$ crystal with its $LaBr_3$:Ce^{3+} counterpart. Although these preliminary studies show a promising performance for $CeBr_3$ this crystal needs to be further studied before replacing $LaBr_3$:Ce^{3+} as the Compton camera absorber material in the future.

The main outlook topic beyond the scope and results of this thesis is to further study the spatial resolution performance of the LMU Compton camera absorber detector for higher photon energies relevant for medical imaging applications ($\sim$4 to 6 MeV), and to optimize the method used to reconstruct the photon interaction position without compromising the detector's spatial resolution. Although a sub-3 mm spatial resolution was obtained using the CAP smoothed reconstruction algorithm the required computational effort to reconstruct an unknown event is still too high to come into the regime of our finnaly envisaged for in-vivo range verification during treatment irradiation. Therefore, preliminary studies are being carried out in our group to replace the currently used algorithm by different machine learning techniques, such as AdaBoost and Random Forest. Moreover, in order to study the detector's spatial resolution performance for photon energies ranging from 4 to 6 MeV, a monoenergetic intense and tightly collimated multi-MeV photon beam is needed. Such a beam can only be provided at few large-scale research facilities. The most promising one is the Extreme-Light Infrastructure (ELI), a new research infrastructure based in four sites. The ELI Nuclear Physics (NP) facility in Bucharest, Romania, presently under construction, will focus on laser-based nuclear physics [79]. The ELI-NP facility hosts a γ-beam source, capable of delivering up to 19.5 MeV photons. This system is based on incoherent Compton backscattering of a high-repetition pulsed laser beam of an electron beam, with an energy of 720 MeV, produced by a warm LINAC. This facility will become fully operational in 2019 and as such become an interesting option for future Compton camera detector tests.

In conclusion, the work presented in this Thesis contributed considerably to the optimization of the performance of the absorber detector of the LMU Compton camera prototype by reducing the number of segments of the readout PMT and therefore the system's complexity. The 3 mm envisaged as the detector's spatial resolution was experimentally surpassed for a 1.3 MeV photon energy, leading to the sound confidence that this value can be realized or even improved for the high-energy range of prompt photons relevant in medical physics applications like hadron therapy.

Bibliography

[1] A. Miani, "Determination of the spatial resolution of a monolithic scintillator in a Compton camera system with MeV range photons," Master's thesis, Università Degli Studi di Milano and LMU Munich, 2016.

[2] M. Mayerhofer, "Optimizing the spatial resolution of the monolithic $LaBr_3$ absorbing scintillator of the Garching Compton-camera prototype," Master's thesis, Ludwig-Maximilian-Universität München, 2016.

[3] J. M. Borras, Y. Lievens, M. Barton, J. Corral, J. Ferlay, F. Bray, and C. Grau, "How many new cancer patients in Europe will require radiotherapy by 2025? An ESTRO-HERO analysis," *Radiotherapy and Oncology*, vol. 119, no. 1, pp. 5–11, 2016.

[4] J. Widder, "The origins of radiotherapy: discovery of biological effects of X-rays by Freund in 1897, Kienböck's crucial experiments in 1900, and still it is the dose." *Radiotherapy and oncology : journal of the European Society for Therapeutic Radiology and Oncology*, vol. 112, no. 1, pp. 150–2, 2014.

[5] S. Aldawood, "Commissioning of a Compton camera for medical imaging," Ph.D. dissertation, LMU Munich, 2016.

[6] M. J. Garcia Borge, *Nuclear Physics for Medicine*. Nuclear Physics European Collaboration Committee (NuPECC), 2014, vol. 24.

[7] R. R. Wilson, "Radiological Use of Fast Protons," *Radiology*, vol. 47, no. 5, pp. 487–491, 1946.

[8] C. Lang, "Medical imaging and characterization of its components," Ph.D. dissertation, LMU Munich, 2015.

[9] M. Jermann, "Particle Therapy Patient Statistics (per end of 2015)," vol. 2016, no. November, p. 2, 2016.

[10] E. Fokas, G. Kraft, H. An, and R. Engenhart-Cabillic, "Ion beam radiobiol-

ogy and cancer: Time to update ourselves," *Biochimica et Biophysica Acta - Reviews on Cancer*, vol. 1796, no. 2, pp. 216–229, 2009.

[11] H.-M. Lu, R. Brett, M. Engelsman, R. Slopsema, H. Kooy, and J. Flanz, "Sensitivities in the production of spread-out Bragg peak dose distributions by passive scattering with beam current modulation," *Medical Physics*, vol. 34, no. 10, pp. 3844–3853, 2007.

[12] A. N. Schreuder, S. G. Hedrick, J. R. Renegar, T. J. Netherton, H. Chen, M. D. Blakey, M. E. Artz, B. H. Robison, A. G. Meek, and M. Fagundes, "Review of Proton Radiation Therapy and the Path to Widespread Clinical Adoption," *Medical Physics International Journal*, vol. 4, no. 1, pp. 35–46, 2016.

[13] J. Krimmer, D. Dauvergne, J. M. Létang, and Testa, "Prompt-gamma monitoring in hadrontherapy: A review," *Nuclear Instruments and Methods in Physics Research, Section A: Accelerators, Spectrometers, Detectors and Associated Equipment*, vol. 878, pp. 58–73, 2017.

[14] H. Paganetti, "Range uncertainties in proton therapy and the role of Monte Carlo simulations," *Physics in Medicine and Biology*, vol. 57, no. 11, pp. R99–R117, 2012.

[15] J. C. Polf and K. Parodi, "Imaging particle beams for cancer treatment," *Physics Today Cancer Physics Today*, vol. 68, no. 34, pp. 28–33, 2015.

[16] S. Kellnberger, W. Assmann, S. Lehrack, S. Reinhardt, P. Thirolf, D. Queirós, G. Sergiadis, G. Dollinger, K. Parodi, and V. Ntziachristos, "Ionoacoustic tomography of the proton Bragg peak in combination with ultrasound and optoacoustic imaging," *Scientific Reports*, vol. 6, no. 1, p. 29305, 2016.

[17] T. L. Szabo, *Diagnostic Ultrasound Imaging: Inside Out*, 2nd ed. Academic Press, 2013.

[18] J. Tada, Y. Hayakawa, K. Hosono, and T. Inada, "Time resolved properties of acoustic pulses generated in water and in soft tissue by pulsed proton beam irradiation–a possibility of doses distribution monitoring in proton radiation therapy." *Medical Physics*, vol. 18, no. 6, pp. 1100–1104, 1991.

[19] U. Amaldi, W. Hajdas, S. Iliescu, N. Malakhov, J. Samarati, F. Sauli, and D. Watts, "Advanced Quality Assurance for CNAO," *Nuclear Instruments and Methods in Physics Research Section A: Accelerators, Spectrometers, Detectors and Associated Equipment*, vol. 617, no. 1-3, pp. 248–249, 2010.

[20] S. Muraro, G. Battistoni, F. Collamati, E. De Lucia, R. Faccini, F. Ferroni, S. Fiore, P. Frallicciardi, M. Marafini, I. Mattei, S. Morganti, R. Paramatti, L. Piersanti, D. Pinci, A. Rucinski, A. Russomando, A. Sarti, A. Sciubba, E. Solfaroli-Camillocci, M. Toppi, G. Traini, C. Voena, and V. Patera, "Monitoring of Hadrontherapy Treatments by Means of Charged Particle Detection," *Frontiers in Oncology*, vol. 6, p. 177, 2016.

[21] P. Henriquet, E. Testa, M. Chevallier, D. Dauvergne, G. Dedes, N. Freud, J. Krimmer, J. M. Létang, C. Ray, M.-H. Richard, and F. Sauli, "Interaction vertex imaging (IVI) for carbon ion therapy monitoring: a feasibility study," *Physics in Medicine and Biology*, vol. 57, no. 14, pp. 4655–4669, 2012.

[22] H. D. Maccabee, U. Madhvanath, and M. R. Raju, "Tissue activation studies with alpha-particle beams." *Physics in Medicine and Biology*, vol. 14, no. 2, pp. 213–24, 1969.

[23] X. Zhu and G. E. Fakhri, "Proton Therapy Verification with PET Imaging," *Theranostics*, vol. 3, no. 10, pp. 731–740, 2013.

[24] H. Panganetti and G. E. Fakhri, "Monitoring proton therapy with PET." *The British journal of radiology*, vol. 88, no. 1051, pp. 1–3, 2015.

[25] W. Enghardt, P. Crespo, F. Fiedler, R. Hinz, K. Parodi, J. Pawelke, and F. Pönisch, "Charged hadron tumour therapy monitoring by means of PET," *Nuclear Instruments and Methods in Physics Research Section A: Accelerators, Spectrometers, Detectors and Associated Equipment*, vol. 525, no. 1-2, pp. 284–288, 2004.

[26] Y. Iseki, H. Mizuno, Y. Futami, T. Tomitani, T. Kanai, M. Kanazawa, A. Kitagawa, T. Murakami, T. Nishio, M. Suda, E. Urakabe, A. Yunoki, and H. Sakai, "Positron camera for range verification of heavy-ion radiotherapy," *Nuclear Instruments and Methods in Physics Research Section A: Accelerators, Spectrometers, Detectors and Associated Equipment*, vol. 515, no. 3, pp. 840–849, 2003.

[27] S. Vecchio, F. Attanasi, N. Belcari, M. Camarda, G. A. P. Cirrone, G. Cuttone, F. Di Rosa, N. Lanconelli, S. Moehrs, V. Rosso, G. Russo, and A. Del Guerra, "A PET Prototype for "In-Beam" Monitoring of Proton Therapy," *IEEE Transactions on Nuclear Science*, vol. 56, no. 1, pp. 51–56, 2009.

[28] E. Yoshida, H. Tashima, T. Shinaji, K. Shimizu, H. Wakizaka, A. Mohammadi, F. Nishikido, and T. Yamaya, "Development of a Whole-Body Dual Ring,"

IEEE Transaction on Radiation and Plasma Medical Sciences, vol. 1, no. 4, pp. 293–300, 2017.

[29] G. Shakirin, H. Braess, F. Fiedler, D. Kunath, K. Laube, K. Parodi, M. Priegnitz, and W. Enghardt, "Implementation and workflow for PET monitoring of therapeutic ion irradiation: a comparison of in-beam, in-room, and off-line techniques," *Physics in Medicine and Biology*, vol. 56, no. 5, pp. 1281–1298, 2011.

[30] J. M. Verburg and J. Seco, "Proton range verification through prompt gamma-ray spectroscopy," *Physics in Medicine and Biology*, vol. 59, no. 23, pp. 7089–7106, 2014.

[31] C. Golnik, F. Hueso-González, A. Müller, P. Dendooven, W. Enghardt, F. Fiedler, T. Kormoll, K. Roemer, J. Petzoldt, A. Wagner, and G. Pausch, "Range assessment in particle therapy based on prompt γ-ray timing measurements," *Physics in Medicine and Biology*, vol. 59, no. 18, pp. 5399–5422, 2014.

[32] M. Testa, M. Bajard, M. Chevallier, D. Dauvergne, N. Freud, P. Henriquet, S. Karkar, F. Le Foulher, J. M. Létang, R. Plescak, C. Ray, M.-H. Richard, D. Schardt, and E. Testa, "Real-time monitoring of the Bragg-peak position in ion therapy by means of single photon detection," *Radiation and Environmental Biophysics*, vol. 49, no. 3, pp. 337–343, 2010.

[33] F. Hueso-González, F. Fiedler, C. Golnik, T. Kormoll, G. Pausch, J. Petzoldt, K. E. Römer, and W. Enghardt, "Compton Camera and Prompt Gamma Ray Timing: Two Methods for In Vivo Range Assessment in Proton Therapy," *Frontiers in Oncology*, vol. 6, p. 80, 2016.

[34] D. Everett, J. Fleming, R. Todd, and J. Nightingale, "Gamma-radiation imaging system based on the Compton effect," *Proceedings of the Institution of Electrical Engineers*, vol. 124, no. 11, p. 995, 1977.

[35] M. H. Richard, M. Dahoumane, D. Dauvergne, M. De Rydt, G. Dedes, N. Freud, J. Krimmer, J. M. Letang, X. Lojacono, V. Maxim, G. Montarou, C. Ray, F. Roellinghoff, E. Testa, and A. H. Walenta, "Design study of the absorber detector of a compton camera for on-line control in ion beam therapy," *IEEE Transactions on Nuclear Science*, vol. 59, no. 5, pp. 1850–1855, 2012.

[36] J. Krimmer, J.-L. Ley, C. Abellan, J.-P. Cachemiche, L. Caponetto, X. Chen, M. Dahoumane, D. Dauvergne, N. Freud, B. Joly, D. Lambert, L. Lestand, J. Létang, M. Magne, H. Mathez, V. Maxim, G. Montarou, C. Morel, M. Pinto,

C. Ray, V. Reithinger, E. Testa, and Y. Zoccarato, "Development of a Compton camera for medical applications based on silicon strip and scintillation detectors," *Nuclear Instruments and Methods in Physics Research Section A: Accelerators, Spectrometers, Detectors and Associated Equipment*, vol. 787, pp. 98–101, 2015.

[37] J. Krimmer, D. Dauvergne, J. Létang, and É. Testa, "Prompt-gamma monitoring in hadrontherapy: A review," *Nuclear Instruments and Methods in Physics Research Section A: Accelerators, Spectrometers, Detectors and Associated Equipment*, vol. 878, pp. 58–73, 2018.

[38] A. Kishimoto, J. Kataoka, T. Nishiyama, T. Taya, and S. Kabuki, "Demonstration of three-dimensional imaging based on handheld Compton camera," *Journal of Instrumentation*, vol. 10, no. 11, 2015.

[39] E. Muñoz, J. Barrio, A. Etxebeste, P. G. Ortega, C. Lacasta, J. F. Oliver, C. Solaz, and G. Llosá, "Performance evaluation of MACACO: a multilayer Compton camera," *Physics in Medicine & Biology*, vol. 62, no. 18, pp. 7321–7341, 2017.

[40] C. Lang, D. Habs, K. Parodi, and P. G. Thirolf, "Sub-millimeter nuclear medical imaging with high sensitivity in positron emission tomography using $\beta^+\gamma$ coincidences," *Journal of Instrumentation*, vol. 9, no. 1, 2014.

[41] C. Muller, M. Bunka, J. Reber, C. Fischer, K. Zhernosekov, A. Turler, and R. Schibli, "Promises of Cyclotron-Produced 44Sc as a Diagnostic Match for Trivalent –Emitters: In Vitro and In Vivo Study of a 44Sc-DOTA-Folate Conjugate," *Journal of Nuclear Medicine*, vol. 54, no. 12, pp. 2168–2174, 2013.

[42] Hamamatsu, "H9500 PMT," https://www.hamamatsu.com/resources/pdf/etd/H9500{_}H9500-03{_}TPMH1309E.pdf, 2015.

[43] ——, "H8500 PMT," https://www.hamamatsu.com/resources/pdf/etd/H8500{_}H10966{_}TPMH1327E.pdf, 2011.

[44] E. B. Podgorsak, *Radiation Physics for Medical Physicists*, 2nd ed. Springer-Verlag Berlin Heidelberg, 2010.

[45] Glenn F. Knoll, *Radiation Detection and Measurement*, 4th ed. Wiley, 2010.

[46] Smith, Hastings A and Lucas, Marcia, *Passive Nondestructive Assay of Nuclear Materials*. United States Nuclear Regulatory Commission, 1997, ch. Gamma-Ray Detectors.

[47] "Intrinsic Resolution of Compton Electrons in $CeBr_3$ Scintillator Using Compact CCT," *IEEE Transactions on Nuclear Science*, vol. 65, pp. 616–620, 2018.

[48] S. Buytaert, C. Enz, F. Piuz, K. Marent, E. H. M. Heijne, F. Krummenacher, P. Jarron, and J.-C. Santiard, "Gassiplex - A Low Noise Analog Signal Processor for Readout of Gaseous Detectors," 1994. [Online]. Available: https://inspirehep.net/record/928417/

[49] Saint-Gobain Crystals, "BrilLanCe380 Scintillation Material," http://www.gammadata.se/assets/Uploads/LaBr3-BrilLanCe-380-Data-Sheet.pdf, 2001.

[50] S. Aldawood, I. Castelhano, R. Gernhäuser, H. Van Der Kolff, C. Lang, S. Liprandi, R. Lutter, L. Maier, T. Marinšek, D. R. Schaart, K. Parodi, and P. G. Thirolf, "Comparative Characterization Study of a $LaBr_3$(Ce) Scintillation Crystal in Two Surface Wrapping Scenarios: Absorptive and Reflective," *Frontiers in Oncology*, vol. 5, no. December, pp. 1–9, 2015.

[51] B. Milbrath, R. Runkle, T. Hossbach, W. Kaye, E. Lepel, B. McDonald, and L. Smith, "Characterization of alpha contamination in lanthanum trichloride scintillators using coincidence measurements," *Nuclear Instruments and Methods in Physics Research Section A: Accelerators, Spectrometers, Detectors and Associated Equipment*, vol. 547, no. 2-3, pp. 504–510, 2005.

[52] J. R. De Laeter, J. K. Böhlke, P. De Bièvre, H. Hidaka, H. S. Peiser, K. J. R. Rosman, and P. D. P. Taylor, "Isotope-abundance variations of selected elements," Tech. Rep. 6, 2003.

[53] "CeBr3 Scintillator," sep 2005. [Online]. Available: https://patents.google.com/patent/US7405404B1/en

[54] SCIONIX, "$Cebr_3$ scintillation crystal," http://www.gammadata.se/assets/Uploads/CeBr3-data-sheet.pdf, 2018.

[55] F. G. A. Quarati, P. Dorenbos, J. Van Der Biezen, A. Owens, M. Selle, L. Parthier, and P. Schotanus, "Scintillation and detection characteristics of high-sensitivity $CeBr_3$gamma-ray spectrometers," *Nuclear Instruments and Methods in Physics Research, Section A: Accelerators, Spectrometers, Detectors and Associated Equipment*, vol. 729, pp. 596–604, 2013.

[56] P. Guss, M. Reed, D. Yuan, A. Reed, and S. Mukhopadhyay, "$CeBr_3$ as a room-temperature, high-resolution gamma-ray detector," *Nuclear Instruments and Methods in Physics Research, Section A: Accelerators, Spectrometers, Detectors and Associated Equipment*, vol. 608, no. 2, pp. 297–304, 2009.

[57] Saint-Gobain Crystals, "BC-630 Silicone Grease," https://www.crystals.saint-gobain.com/sites/imdf.crystals.com/files/documents/bc-630.pdf, 2008.

[58] Mesytec, "Mcfd-16," https://www.mesytec.com/products/datasheets/MCFD-16.pdf, 2018.

[59] ——, "Mqdc-32," https://www.mesytec.com/products/datasheets/MQDC-32.pdf, 2018.

[60] M. J. Hoffmann, N.Kurz, "Triva 5, vme trigger module," https://www.gsi.de/fileadmin/EE/Module/TRIVA/triva5_5.pdf, 2009.

[61] Lynx Software Technologies, "LynxOS, howpublished = "http://www.lynx.com/products/real-time-operating-systems/lynxos-rtos/", publisher=Lynx Software Technologies, year=2018."

[62] R. Lutter, O. Schaile, K. Schöffel, K. Steinberger, P. Thirolf, and C. Broude, "MARaBOO - a MBS and ROOT based online/offline utility," in *1999 IEEE Conference on Real-Time Computer Applications in Nuclear Particle and Plasma Physics. 11th IEEE NPSS Real Time Conference. Conference Record (Cat. No.99EX295)*. IEEE, pp. 363–366.

[63] "ROOT a Data analysis Framework — ROOT a Data Analysis Framework." [Online]. Available: https://root.cern/

[64] Hamamatsu, "H12700 PMT," https://www.hamamatsu.com/resources/pdf/etd/H12700{_}TPMH1348E.pdf, 2018.

[65] S. Liprandi, "Development and performance evaluation of detectors in a Compton camera arrangement for ion beam range monitoring in particle therapy," Ph.D. dissertation, LMU Munich, in preparation (2018).

[66] Hamamatsu, "H9500 PMT," https://www.hamamatsu.com/resources/pdf/etd/H9500_H9500-03_TPMH1309E.pdf, 2015.

[67] Saint-Gobain Crystals, "Bc-418," https://www.crystals.saint-gobain.com/sites/imdf.crystals.com/files/documents/sgc-bc418-420-422-data-sheet_69699.pdf, 2016.

[68] H. Photonics, "XP2020Q," http://www.hzcphotonics.com/products/ProductManual.pdf, 2018.

[69] T. Binder, "Evaluation of new components for the absorber detector of the

Garching Compton camera prototype," Master's thesis, Ludwig-Maximilian-Universität München, 2017.

[70] P. L. Reeder and D. C. Stromswold, "Performance of Large NaI(Tl) Gamma-Ray Detectors Over Temperature-50°C to +60°C," Northwest NAtional Laboratory, Tech. Rep., 2004.

[71] Hamamatsu Photonics K.K., "Photomultiplier tubes - basics and applications," Word Technical Writing, Inc., Ed. Hamamatsu Photonics K.K., 2007, ch. 4, pp. 29–82.

[72] E. Fix and J. L. Hodges, "Discriminatory Analysis. Nonparametric Discrimination: Consistency Properties," *International Statistical Review / Revue Internationale de Statistique*, vol. 57, no. 3, p. 238, 1989.

[73] M. Maas, D. van der Laan, D. Schaart, J. Huizenga, J. Brouwer, P. Bruyndonckx, S. Leonard, C. Lemaitre, and C. van Eijk, "Experimental characterization of monolithic-crystal small animal PET detectors read out by APD arrays," *IEEE Transactions on Nuclear Science*, vol. 53, no. 3, pp. 1071–1077, 2006.

[74] D. van der Laan, M. Maas, H. de Jong, D. Schaart, P. Bruyndonckx, C. Lemaître, and C. van Eijk, "Simulated performance of a small-animal PET scanner based on monolithic scintillation detectors," *Nuclear Instruments and Methods in Physics Research Section A: Accelerators, Spectrometers, Detectors and Associated Equipment*, vol. 571, no. 1-2, pp. 227–230, 2007.

[75] D. R. Schaart, H. T. van Dam, S. Seifert, R. Vinke, P. Dendooven, H. Löhner, and F. J. Beekman, "A novel, SiPM-array-based, monolithic scintillator detector for PET," *Physics in Medicine and Biology*, vol. 54, no. 11, pp. 3501–3512, 2009.

[76] H. T. Van Dam, S. Seifert, R. Vinke, P. Dendooven, H. Löhner, F. J. Beekman, and D. R. Schaart, "Improved nearest neighbor methods for gamma photon interaction position determination in monolithic scintillator PET detectors," *IEEE Transactions on Nuclear Science*, vol. 58, no. 5, pp. 2139–2147, 2011.

[77] CAEN, "DT5800 Digital Detector Emulator," http://www.caen.it/csite/CaenProd.jsp?idmod=837{&}parent=59{#}, 2016.

[78] S. Liprandi, M. Mayerhofer, S. Aldawood, T. Binder, G. Dedes, A. Miani, D. R. Schaart, I. I. V. Lozano, K. Parodi, and P. G. Thirolf, "Sub-3mm spatial resolution from a large monolithic $LaBr_3$ (Ce) scintillator," *Current Directions in Biomedical Engineering*, vol. 3, no. 2, pp. 655–659, 2017.

[79] *Extreme Light Infrastructure - Nuclear Physics (ELI-NP)*, accessed in August, 2018. [Online]. Available: http://www.eli-np.ro/

Appendices

A

PMTs' specifications

The more relevant specifications of the three different PMTs mentioned in this thesis work are present in Table A.1 and in Fig. A.1, Fig. A.2 and Fig. A.3.

Type	N° of anode pixels	Window material	Photocathode material	Rise time (ns)
H9500	256 (16 x 16 matrix)	Borosolicate glass	Bialkali	0.8
H8500C	64 (8 x 8 matrix)			
H12700A-10				0.52

Table A.1: Specifications of the three flat panel type multianode PMT assemblies used during this thesis work. The table shows the number of anode pixels, the window and photocathode material and the signal rise time [66, 43, 64].

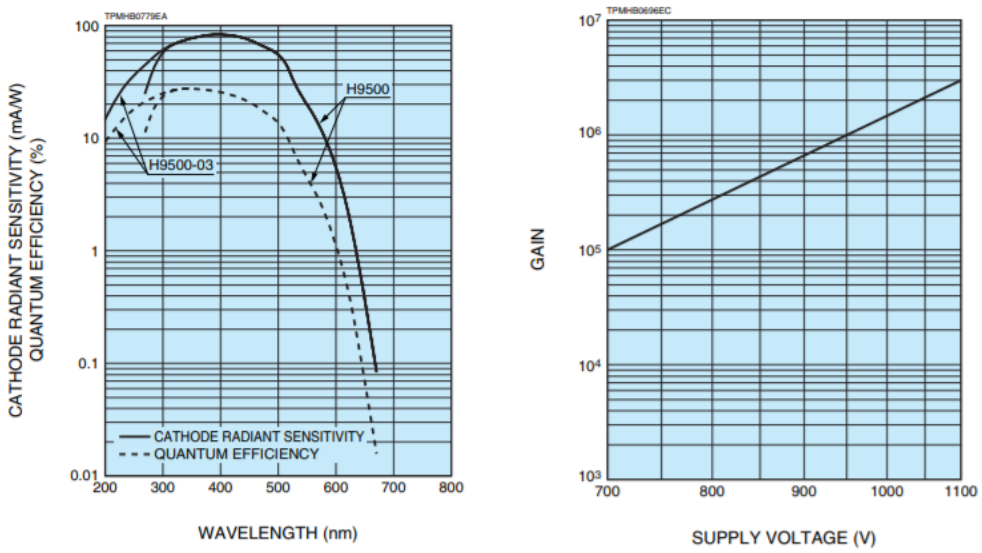

(a) (b)

Figure A.1: Typical spectral response (a) and typical gain (b) of the H9500 PMT [66].

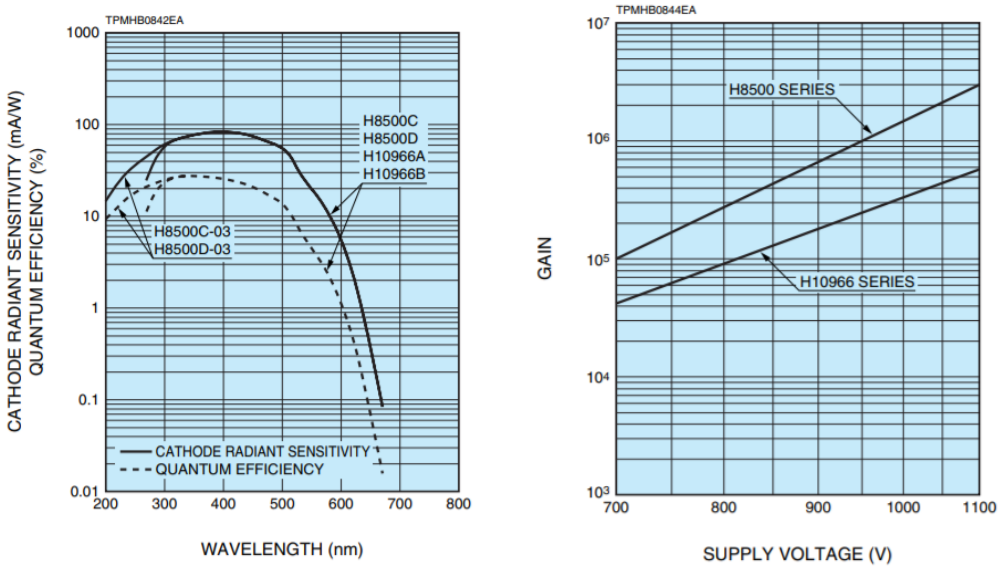

(a) (b)

Figure A.2: Typical spectral response (a) and typical gain (b) of the H8500 PMT [43].

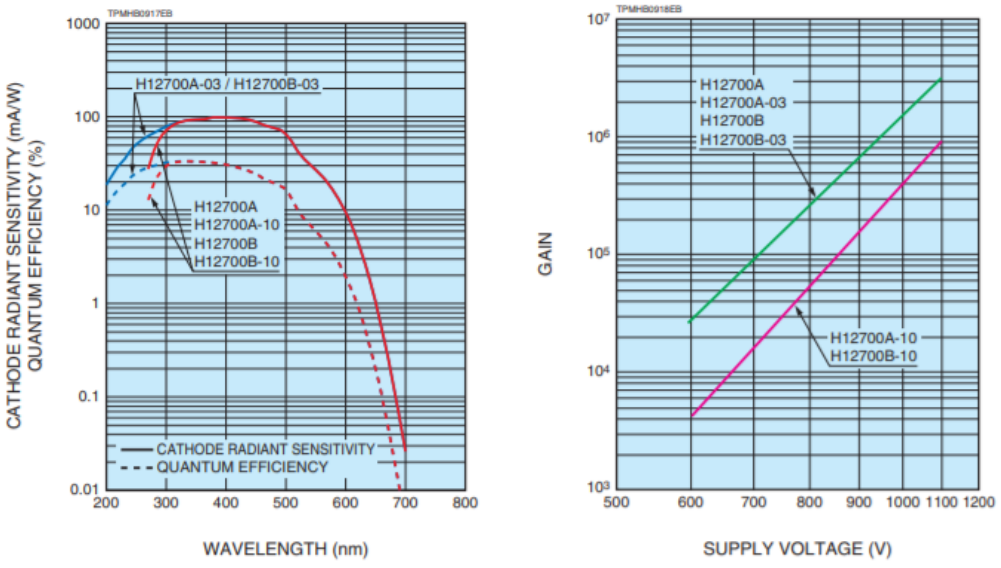

(a) (b)

Figure A.3: Typical spectral response (a) and typical gain (b) of the H12700 PMT [64].

B

PMT non-uniformity matrix

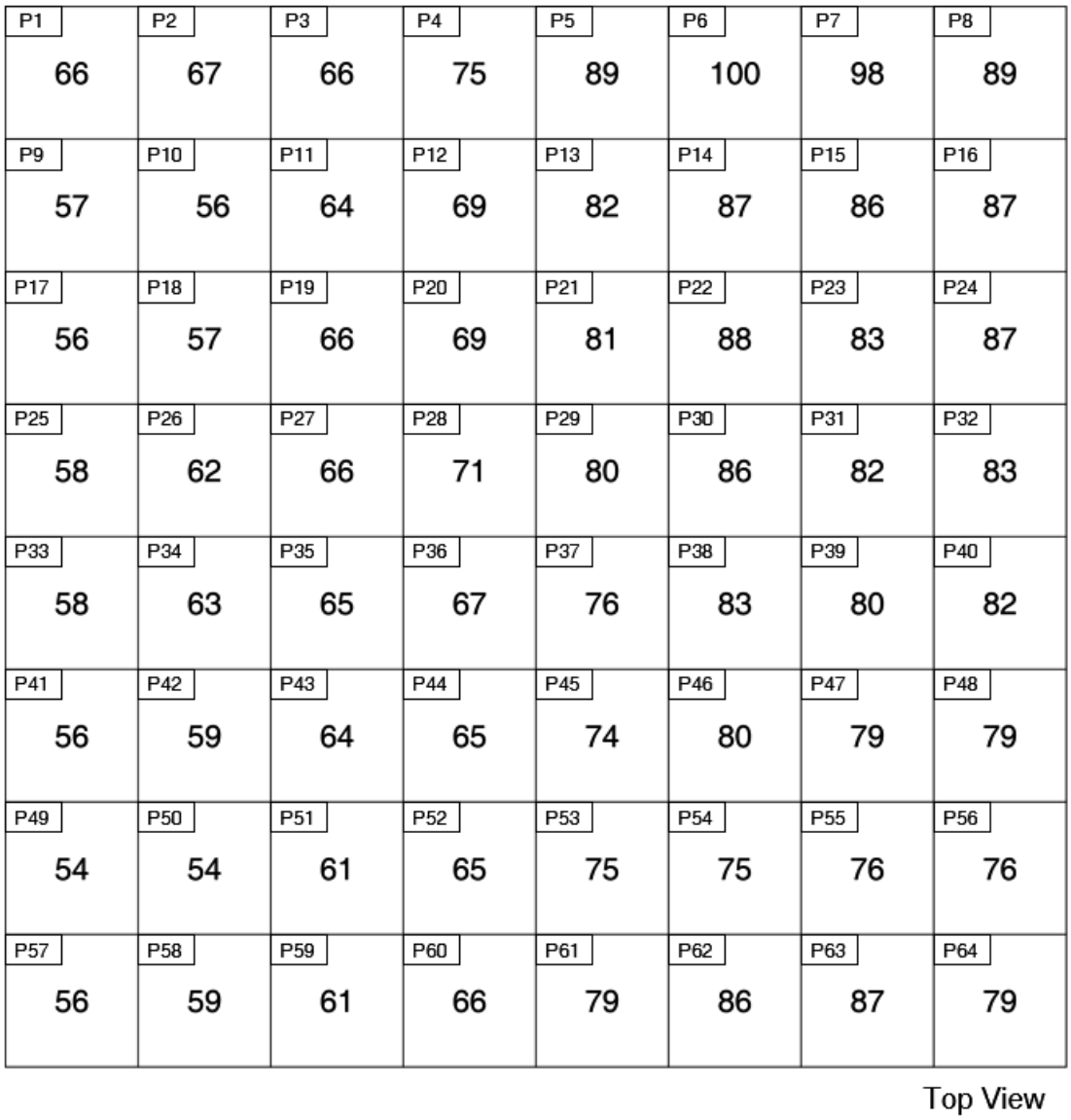

Figure B.1: H8500 PMT non-uniformity matrix [43].

C

Absorber Component coupling procedure

The current absorber component of the LMU Compton camera was coupled by our group in our laboratory, according to the following procedure which is illustrated in the figure present in the next page:

a) The crystal (2) side covered by the quartz window was carefully covered with a thin homogeneous layer of optical coupling grease (1) (BC-630 Silicone Grease manufactured by Saint-Gobain Crystals [57]) for light guidance.

b) The PMT (3) was carefully mounted on top of the crystal side covered with optical grease.

c) In order to ensure that the crystal and the PMT are perfectly aligned and connected Gaflon P.T.F.E. tape (4) was used.

d) To ensure light tightness Aluminium tape (5) was employed all around the junction between the crystal and the PMT.

e) Finally the detector was carefully covered with two layers of black PVC tape (6).

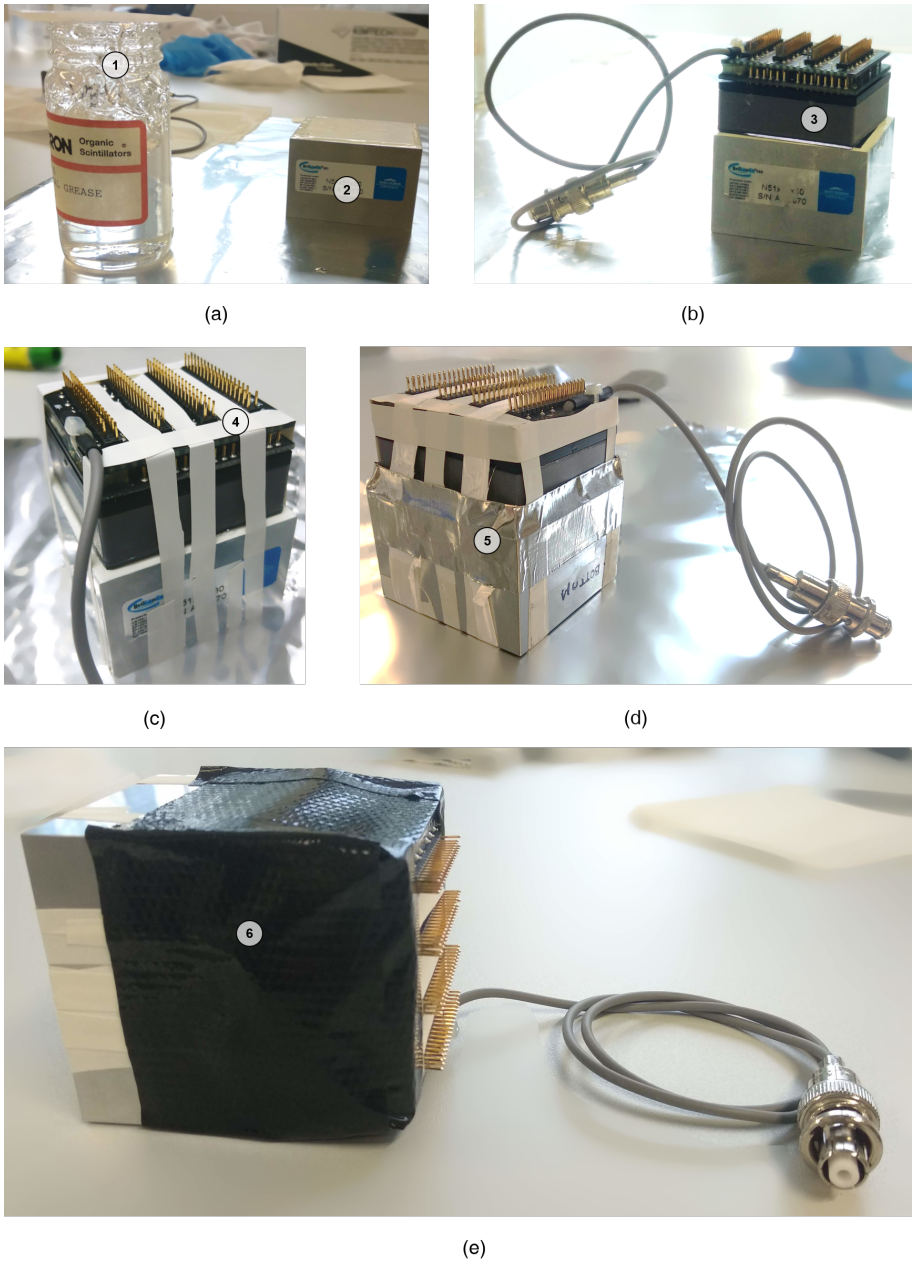

Figure C.1: Absorber Component coupling procedure. For a detailed description see main text.

D

Conference contributions

The work preformed in the present thesis was (or will soon be) presented at 2 conferences:

1. T. Binder, R. Viegas Rego, S. Liprandi, T. Ganka, F. Schneider, F. Wiest, R. Foji, K. Parodi and P.G. Thirolf, "Characterization of a Compton Camera Absorber Detector," presented at the *49. Jahrestagung der Deutschen Gesellschaft für Medizinische Physik, Meistersingerhalle in Nürnberg*, Germany, September 2018.
2. S. Liprandi, S. Takyu, T. Binder, G. Dedes, K. Kamada, M. Kawula, R. Lutter, F. Nishikido, I. I. Valencia, R. Viegas, 4, T. Yamaya, K. Parodi and P. G. Thirolf, "Monolithic LaBr3(Ce) absorber and segmented GAGG scatter detectors in a Compton camera arrangement for medical imaging," *2018 IEEE Nuclear Science Symposium and Medical Imaging Conference NSS/MIC*, International Convention Centre Sydney, Australia, to be presented in November 2018.